8-15-2009

A Segmented aperture space telescope modeling tool and its application to remote sensing as understood through image quality and image utility

Michael E. Zelinski

A Segmented Aperture Space Telescope Modeling Tool and Its Application to Remote Sensing as Understood Through Image Quality and Image Utility

by

Michael E. Zelinski

Bachelors of Science, Rochester Institute of Technology 2006

A thesis submitted in partial fulfillment of the
requirements for the degree of Master of Science
in the Chester F. Carlson Center for Imaging Science
Rochester Institute of Technology

August 15, 2009

Signature of the Author _____

Accepted by _____
Coordinator, M.S. Degree Program Date

CHESTER F. CARLSON CENTER FOR IMAGING SCIENCE
ROCHESTER INSTITUTE OF TECHNOLOGY
ROCHESTER, NEW YORK

CERTIFICATE OF APPROVAL

M.S. DEGREE THESIS

The M.S. Degree Thesis of Michael E. Zelinski
has been examined and approved by the
thesis committee as satisfactory for the
thesis required for the
M.S. degree in Imaging Science

_____
Dr. John Schott, Thesis Advisor

_____
Dr. Robert D. Fiete

_____
Dr. David Messinger

_____
Date

THESIS RELEASE PERMISSION

ROCHESTER INSTITUTE OF TECHNOLOGY

CHESTER F. CARLSON CENTER FOR IMAGING SCIENCE

Title of Thesis:

A Segmented Aperture Space Telescope Modeling Tool and Its Application to Remote Sensing as Understood Through Image Quality and Image Utility

I, Michael E. Zelinski, hereby grant permission to Wallace Memorial Library of R.I.T. to reproduce my thesis in whole or in part. Any reproduction will not be for commercial use or profit.

Signature _____

Date

Acknowledgements

I have to start this by thanking Dr. John Schott for bringing me into this program. When I was looking for a research project he saw something in me and knew I would enjoy segmented and sparse aperture modeling. Working under his wing was a pleasure.

Dr. David Messinger always had his door open and when I would visit he would put down his work no matter how busy he was. His advise and guidance were always constructive.

Dr. Robert Fiete was very kind to come on as an outside reader for this work. His input was always useful and greatly appreciated.

Dr. Brian Daniel was a huge help in all areas and a good friend. During the first year of this work he served as my unofficial advisor and got me started on building my own systems model.

May Casterline has been a wonderful friend over the past seven years at RIT. In grad school May took the place of my undergraduate partner in crime (Jeff Meade) at the white board and she and her husband opened her home/refrigerator to me.

My office mates Jacqueline Speir and Ariel Schlamm have been wonderful, fun people to be around. In addition to this they are great people to bounce ideas off of, take interest in my work, and they always seem to remember the syntax for obscure IDL commands.

Out of any professor at RIT Dr. Roger Easton has taught me the most; this is not because I have taken 5 classes from Roger, but because of the quality of his teaching.

Dr. Carl Salvaggio for giving me great advice, a listening ear, and some excellent time in the classroom.

Cindy Schultz and Sue Chan for taking on the difficult task of keeping me in line.

Dr. Bernard Brooks for teaching me how to be passionate about freshman calculus (it spilled over into other areas of study and got me into grad school).

Last but certainly not least my family - Alan, Joan, and Lindsay Zelinski

This document is dedicated to my friends from Potsdam, NY.

A Segmented Aperture Space Telescope Modeling Tool and Its Application to Remote Sensing as Understood Through Image Quality and Image Utility

by

Michael E. Zelinski

Submitted to the
Chester F. Carlson Center for Imaging Science
in partial fulfillment of the requirements
for the Master of Science Degree
at the Rochester Institute of Technology

Abstract

The remote sensing community is constantly pushing technology forward to achieve better system performance, this is often done by improving signal-to-noise ratio and spatial and spectral resolution. However, improving one design parameter (such as spatial resolution) could detract from another (such as signal-to-noise). A flexible imaging system simulation tool capable of modeling the effects of changes in system parameters would be a great asset to design engineers. In words, this tool would manipulate a "perfect" image and produce an output image identical to one physically created by the imaging system. Having such a tool available would make it possible to fully understand a design's potential. In addition, this tool can be used to understand the importance of changes in system parameters.

Modern space based remote sensing systems are taking on new forms using sparse and segmented apertures with lightweight mirrors. The driving force for this is that systems are constrained by the size and weight tolerances of the launch vehicles. The new designs come with new problems, many of which are related to the geometry and aberrations of the aperture. The tool developed in this effort will be able to examine the effects of different amounts and types of aperture aberrations.

The task is to build an imaging system simulation tool, based on linear systems and standard radiometry, capable of accurately displaying the performance of a plausible design. Using this tool, several designs will be tested using image quality analysis and image utility.

Image quality/utility will be determined using three techniques. The first is an image quality prediction technique called the Generalized Image Quality Equation (GIQE) which relates system characteristics to the *National Imagery Interpretability Rating Scale* (NIIRS). However, due to the unusual aperture geometry of the sparse aperture systems Fiete et al. (2002) showed that the GIQE is unable to accurately predict image quality. The other two approaches are therefore somewhat unorthodox. These approaches do not actually define an image quality but allow systems to be ranked by their performance in a test of motion detection and a test of spatial target detection. A multispectral motion detection algorithm developed and implemented by Adams (2008) combined with motion truth show a given imaging system's ability to track motion. A similar experimental design is evaluated using the spatial target detection algorithm.

The tests reveal how changes in parameters such as GSD; SNR; spectral band selection; piston, tip, and tilt aberrations; and light weight optic aberrations affect a system's NIIR's estimate, ability to detect motion, or ability to detect objects.

Contents

List of Figures

Chapter 1

Introduction

Terrestrial remote sensing allows analysts to view areas of Earth that may be inaccessible. There are many forms of terrestrial remote sensing and as one might imagine certain remote sensing systems are better suited for a given application than others. It is important to note that remote sensing is a diverse field and these systems are complex enough that it is nearly impossible for a systems design engineer to have a complete understanding of a system's capabilities before it is fielded. However, modern scene simulation techniques combined with accurate sensor and optics information can be used with a linear systems approach to give an engineer an accurate estimate of a system's capabilities. This research demonstrates how a system can be modeled and how an engineer can use the model to evaluate a system's performance and capabilities.

In this field, there is a constant force driving technology to produce higher spatial and spectral resolution imagery with better signal to noise ratios (SNR). In addition to this, the community has become interested in systems that would be capable of acquiring imagery at any time over a given expanse of land. To have this ability the space system must be located in a geostationary orbit at an altitude of 35,786 km above the equator. But to have the desired spatial resolution and SNR the systems must have a very large primary aperture.

There are some fundamental difficulties with putting a satellite in a geostationary orbit. The two problems most commonly dealt with are the size and weight of the payload. A spacecraft carried aboard a launch vehicle against the force of gravity for 35,786 km must

be as light as possible. It was mentioned that the primary aperture on the desired system will have to be large. This means a traditional monolithic aperture space telescope cannot be used. Monolithic apertures tend to be very heavy for their size (high areal density), and to achieve the desired performance (of less than 1.5m GSD with good SNR) the monolithic aperture could easily have a larger diameter than the launch vehicle expected to carry it. Newer types of apertures include segmented and sparse (or dilute) apertures. These apertures can be made light, durable, and foldable. This allows a large telescope to be folded, placed within a launch vehicle, survive the launch without attaining additional aberrations, and then unfold once deployed. With these new types of apertures comes a new a set of problems; perhaps the largest problem is aligning the sub-apertures so they produce an image of equal sharpness to the one created by a monolithic aperture of the same size.

This document will present the physics behind modeling a space-borne imaging system and demonstrate how different telescope parameters can be quickly interchanged and compared. The goal is to then use this tool to create imagery that can be applied to motion detection and spatial target recognition tests. By observing the results of these tests (for example, % of motion detected) it is possible to understand the capability of a proposed design. This technique also allows designers to analyze the potential benefits of improving individual features of a design. For example, they could analyze the cost and benefits of having a higher signal to noise ratio or lower mirror aberrations. Perhaps these changes will produce an equal performance increase while the cost of one improvement is radically different than the cost of the other. Cost is always an issue and understanding the most efficient and cost effective method of improving a system is vital to every large project.

Chapter 2

Work Statement

- Develop a flexible Fourier optics based model of a remote sensing platform at a geostationary orbit (35,786 km) above the equator. There should be full flexibility of detector type (this includes various noise parameters, quantum efficiency, and pixel pitch); scene content; aperture geometry; and optical parameters including focal length, reference wavelength, flimsy style aberrations, and piston, tip, and tilt aberrations.

- The model should also have an alternate mode that allows users to specify GSD and SNR.

- Demonstrate a novel way of modeling lightweight optic aberrations using a fractal Brownian motion algorithm.

- Use GIQE to quantify image quality.

- Process video imagery using the modeling tool and then use a multispectral motion detection algorithm developed by Adams (2008) for a test of motion detection ability. This can be viewed as a test of information content in the data because it is affected by all aspects of system design.

- Process imagery using the modeling tool and then use a Matched Filter with a spatial target on the output image to test spatial image utility.

- Use the tests mentioned above on many different imaging scenarios by individually incrementing GSD, SNR, and aberration levels.
- Use the results to gain an understanding of the importance of the tested parameters.

Chapter 3

Background and Theory

This chapter will provide a basic theoretical background for the proposed research. To begin, it is best to have a basic understanding of how an imaging system can be modeled. A common way of doing this is through an image "chain" approach. Each link of the chain will describe how information is transferred - in various forms of energy - from an input object to an output image. Different types of imaging systems have different links in the chain; a standard example for an optical system is listed below:

1. electromagnetic radiation from an energy source,
2. EM radiation interacts (reflects, absorbs, or scatters) with object material,
3. re-emitted energy then propagates from object to imaging system,
4. energy is then collected (by an aperture in an optical system) and propagated (by lens and mirrors) through the imaging system,
5. energy is converted into some kind of quantifiable form (typically electrons),
6. image processing and storage (optional),
7. image display.

Most of this research will address numbers 4, 5, and 6.

Light is emitted from a point source and diverges in all directions. This light is often characterized by its wavelength (λ) and its power per unit area and solid angle - radiance $[W/(m^2 sr)]$. Typically we are not interested in objects consisting of one point source, but objects made of a distribution of point sources, all emitting light that spherically diverges from its point of emission. The imaging system redirects the diverging light to converge forming an image on a focal plane. In optical imaging systems, the measured quantity is the time average of the squared magnitude of the complex valued amplitude of the electromagnetic radiation. This is also referred to as irradiance and has units of W/m^2. Much of what will be discussed in the following sections covers the process from when we collect diverging light (as radiance) in our aperture to the moment it falls on the focal plane (as irradiance). From there we look at what happens when the light interacts with the sensor and how the retrieved image can be enhanced. Lastly we discuss some of the challenges of working with sparse and segmented apertures.

Much of what will be discussed in the following sections assumes the system is linear and shift invariant (see Section 3.1); we will build mathematical representations of imaging systems based on this assumption. Despite this, it is important to recognize that imaging systems are NOT linear and shift invariant and it is therefore impossible to completely represent them in this fashion. What we CAN do is put forth the idea that imaging systems are a mapping from one space to another. The simplest mathematical description of an imaging system is done using an operator $\mathcal{O}$ on an input function $f(x, y, z, t, \lambda)$ to yield an output $g(x', y')$.

$$\mathcal{O}\{f[x, y, z, t, \lambda]\} = g[x', y'] \tag{3.1}$$

where $f(x, y, z, t, \lambda)$ is an object (a distribution of point sources) that vary in 3-dimensional space (x, y, z), time (t), and emitted wavelength (λ). And $g(x', y')$ is the resulting image (perceived by the viewer) after $f(x, y, z, t, \lambda)$ has been operated on by the nonlinear operator $\mathcal{O}$. During this process where $\mathcal{O}$ maps from the real world to our eyes the spatial, temporal, and spectral properties are "averaged" and in most cases lost. It is the job of systems designers to create systems that re-map this real world space in a fashion that allows the important information to make it to the viewer.

3.1 Linear Systems Theory for Imaging Systems

It is well known that most imaging systems are not mathematically linear and shift-invariant; however, it can be assumed that the degree of error related to nonlinearity and shift-variance is negligible. This makes it possible to characterize imaging systems from a linear systems perspective. To characterize the imaging system's spatial manipulation of the real world we use a *point spread function* (PSF); this is often referred to as the *impulse response*. If the system can be assumed noiseless, linear, and shift-invariant the system output can be predicted through this convolution expression:

$$g[x,y] = f[x,y] * h[x,y] = \int_{-\infty}^{-\infty}\int_{-\infty}^{-\infty} f[\alpha,\beta]h[x-\alpha,y-\beta]d\alpha d\beta. \tag{3.2}$$

where $f[x,y]$ represents the object plane radiance, $h[x,y]$ is the system impulse response (PSF), $g[x,y]$ is the output image, and "$*$" is the mathematical symbol for convolution. Convolutions can be computationally expensive. Luckily, there is another method, through usage of a Fourier transform, that achieves the same result far more efficiently. The continuous Fourier transform is expressed mathematically as:

$$F[\xi,\eta] = \mathcal{F}\{f[x,y]\} = \int_{-\infty}^{+\infty}\int_{-\infty}^{+\infty} f[x,y]e^{-2\pi i(\xi x+\eta y)}dxdy. \tag{3.3}$$

where $F[\xi,\eta]$ is the Fourier transform pair in the frequency domain, f[x,y] is the function in the spatial domain, $\mathcal{F}\{\ \}$ is the shorthand notation for the Fourier transform on the right hand side of the equation, i is an imaginary number ($\sqrt{-1}$), and ξ and η are coordinates in the frequency domain. The most powerful property of the Fourier transform for imaging systems is the Filter Theorem. The theorem is derived from Eq. 3.2 through a simple Fourier transform [Easton (2004)] and is expressed below as:

$$G[\xi,\eta] = F[\xi,\eta] \cdot H[\xi,\eta]. \tag{3.4}$$

In the frequency domain Eq. 3.2 is greatly simplified by the fact that a convolution in the spatial domain is equivalent to a multiplication in the frequency domain. The filter the-

orem's prevalence in imaging has lead to the naming of the system $h[x, y]$ and its Fourier transform pair $H[\xi, \eta]$ as the *point spread function (PSF)* (as stated earlier) and the *transfer function* respectively. Much of this research will focus on producing accurate PSFs and transfer functions for various parts of the modeled imaging system.

As mentioned before the Fourier transform of the PSF is referred to as the transfer function; however in optical systems the transfer function is referred to as the *optical transfer function* (OTF) and the normalized magnitude is the *modulation transfer function* (MTF). The MTF of the optical system will be discussed further in Section 3.3.

The frequency response generated from Eq. 3.4 can be inverse Fourier transformed to give us the output image $g[x, y]$. This is shown in the equation below for continuous functions:

$$g[x, y] = \mathcal{F}^{-1}\{G[\xi, \eta]\} = \int_{-\infty}^{+\infty} \int_{-\infty}^{+\infty} G[\xi, \eta] e^{+2\pi i(\xi x + \eta y)} d\xi d\eta. \tag{3.5}$$

where $\mathcal{F}^{-1}\{\ \}$ is shorthand for the inverse Fourier transform operator. In conclusion, a continuous system free of noise where the PSF is known can be modeled by Fourier transforming the input scene radiance and the PSF, array multiplying the two together, and then inverse Fourier transforming to get the output image. Of course, the system modeling approach just described is unrealistic because it is noiseless. To build *a more* correct model statistically independent additive random noise can be introduced to Equations 3.2 and 3.4:

$$g[x, y] = f[x, y] * h[x, y] + n[x, y]. \tag{3.6}$$

where $n[x, y]$ is the total statistically independent random noise in the system. This function is simply reexpressed in the frequency domain as:

$$G[\xi, \eta] = F[\xi, \eta] \cdot H[\xi, \eta] + N[\xi, \eta]. \tag{3.7}$$

where $N[\xi, \eta]$ is the frequency spectrum of the system noise. Approaching this problem through linear systems produces a concise mathematically tractable model for an imaging system. This type of model also fits nicely within the frame work of the image chain. This thesis will examine several potential imaging scenarios with various forms of output. The lin-

ear system approach ensures that all changes within the model have a linear correspondence with the model output.

3.2 Scene Radiance and Detected Signal

Because this model attempts to accurately represent a real world system using incoherent radiation, it should have data that accurately represents the the world's incoherent nature. Schott (2007) describes the primary radiation transfer mechanisms in this equation:

$$\begin{aligned} L_{r,total}[\lambda] \quad = \quad & \Bigg(E_{s,exo}[\lambda] cos[\sigma'] \tau_1[\lambda] \frac{\rho[\lambda]}{\pi} + \varepsilon[\lambda] L_{emis}[\lambda, T] + F \frac{r[\lambda]}{\pi} \Bigg(E_{ds}[\lambda] + \\ & E_{de}[\lambda] \Bigg) + (1 - F) \big[L_{bs}[\lambda] + L_{be} \big] r[\lambda] \Bigg) \tau_2 + L_{us}[\lambda] \\ & + L_{ue}[\lambda] \end{aligned} \tag{3.8}$$

where:

- $E_{s,exo}[\lambda]$ is the exoatmospheric radiance
- σ' is the solar zenith angle
- τ_1 is the atmospheric transmission along the sun-target path
- ρ is the bidirectional reflectance
- ε is the target emissivity
- $L_{emis}[\lambda, T]$ is the self emitted radiance for a blackbody at temperture *T*
- F is the fraction of the hemisphere above the target that is sky
- $E_{ds}[\lambda]$ is the reflected downwelled irradiance
- $r[\lambda]$ is the target reflectance
- τ_2 is the atmospheric transmission along the sun-target path

- $E_{de}[\lambda]$ is the emissive downwelled irradiance
- $L_{bs}[\lambda]\ and\ L_{be}[\lambda]$ are the reflective and emissive background radiance
- $L_{us}[\lambda]\ and\ L_{ue}[\lambda]$ are the reflected and emissive upwelled radiance

Because this project will not be using the thermal portion of the EM spectrum we can slim this equation down by omitting the thermal components.

$$L_{r,total}[\lambda] = \left[E_{s,exo} cos\sigma' \tau_1[\lambda]\frac{\rho[\lambda]}{\pi} + F E_{ds}[\lambda]\frac{r[\lambda]}{\pi} + (1-F)L_{bs}[\lambda]\right] r[\lambda]\tau_2[\lambda] + L_{us}[\lambda] \quad (3.9)$$

where $L_{r,total}$ is the reflective (V/NIR) radiance at the aperture. The question now becomes, how do we relate the measured signal to the radiance at the entrance aperture? We start by using the $G\#$ equation [Schott (2007)] to relate the radiance at the entrance aperture to the irradiance on the detector:

$$G\#[\lambda] = \frac{L_{r,total}[\lambda]}{E_{inc}[\lambda]} = \frac{1 + 4(f\#)^2}{F_{fill}\tau_{opt}\pi}\left[\frac{1}{sr}\right] \quad (3.10)$$

where $f\#$ is the ratio of the focal length over the aperture diameter, F_{fill} is the fill factor or the percentage of aperture that would fill an unobscured aperture of equal diameter, and τ_{opt} is the transmission of the optics. The above equation can be rearranged so that it is solved for $E_{incident}$:

$$E_{inc}[\lambda] = \frac{F_{fill}\tau_{opt}\pi}{1 + 4(f\#)^2} L_{r,total}[\lambda]\left[\frac{W}{m^2}\right]. \quad (3.11)$$

The flux onto a pixel can then be determined by multiplying this quantity by the area of the pixel.

$$\Phi[\lambda] = E_{inc}[\lambda] A_{pixel} = \frac{A_{pixel} F_{fill}\tau_{opt}\pi}{1 + 4(f\#)^2} L_{r,total}[\lambda][W] \quad (3.12)$$

The flux can then be multiplied by the integration time to get the total energy in Joules onto the pixel:

$$\Phi_{Total}[\lambda] = E_{inc}[\lambda] A_{pixel} T_{int} = \frac{A_{pixel} T_{int} F_{fill}\tau_{opt}\pi}{1 + 4(f\#)^2} L_{r,total}[\lambda][Joules] \quad (3.13)$$

This number can then be divided by the energy of one photon at the central wavelength λ to yield the number of photons hitting the pixel:

$$\#photons = \frac{\Phi_{Total}}{\frac{hc}{\lambda}} \tag{3.14}$$

where h is Planck's Constant (6.626 x $10^{-34}[J \cdot s]$) and c is the speed of light (2.9979 x$10^{-8}\left[\frac{m}{s}\right]$). The signal in electrons is computed as the # photons times the quantum efficiency (QE) $\left[\frac{\#electrons}{\#photons}\right]$, integrated over all wavelengths:

$$\begin{aligned} S_{electrons} &= \frac{A_{pixel} T_{int} F_{fill} \pi}{hc(1+4(f\#)^2)} \int_0^{+\infty} L_{r,total}[\lambda] \tau_{opt}[\lambda] QE[\lambda] \lambda d\lambda \\ &\left[sec \;\; sr \;\; m^2 \;\; \frac{1}{J \cdot sec} \;\; \frac{sec}{m} \frac{W}{m^2 \;\; sr \;\; \mu m} \;\; \mu m \;\; \mu m\right]. \end{aligned} \tag{3.15}$$

The signal in electrons is then converted to volts in a transistor. This is done mathematically using a conversion gain, $G_{conv}\left[\frac{Volts}{electron}\right]$. There is also an electronic gain, G_{elec} from the focal plane array to the A/D converter. These gains are shown below:

$$S_{volts} = G_{conv} G_{elec} S_{electrons}[Volts]. \tag{3.16}$$

If Eq. 3.15 is substituted into 3.16 and is rewriten we find:

$$S_{volts} = G_{conv} G_{elec} \frac{F_{fill} T_{int} \pi A_{detector}}{hc(1+4(f\#)^2)} \int_0^{+\infty} L_{aper}[\lambda] \tau_{opt}[\lambda] QE[\lambda] \lambda d\lambda [Volts]. \tag{3.17}$$

This radiometric treatment is for one pixel in the absence of noise. It ignores the fact that we are working with a 2D array of pixels and that system components like the aperture and optics will degrade or blur the PSF and subsequently the image. The details about how to accurately model the PSF will be discussed in the coming sections; however, now is an appropriate time to look into how to apply the PSF to imagery. Equation 3.15 can be rewritten

so that it includes spatial variation instead of one pixel:

$$S_{volts}[x,y] = G_{conv}G_{elec}\frac{F_{fill}T_{int}\pi A_{detector}}{hc(1+4(f\#)^2)}\int_0^{+\infty} L_{aper}[x,y;\lambda]\tau_{opt}[\lambda]QE[\lambda]d\lambda. \quad (3.18)$$

The PSF is applied to this function through a convolution (Eq. 3.2) with the system reaching radiance:

$$\begin{aligned} S_{volts}[x,y] &= G_{conv}G_{elec}\frac{F_{fill}T_{int}\pi A_{detector}}{hc(1+4(f\#)^2)} \\ &\int_0^{+\infty}\big(L_{aper}[x,y;\lambda] * PSF[x,y;\lambda]\big)\tau_{opt}[\lambda]QE[\lambda]d\lambda. \end{aligned} \quad (3.19)$$

Just for completeness and future reference it is necessary to apply the PSF to Eq. 3.15:

$$\begin{aligned} S_{electrons}[x,y] &= \frac{F_{fill}T_{int}\pi A_{detector}}{hc(1+4(f\#)^2)} \\ &\int_0^{+\infty}\big(L_{aper}[x,y;\lambda] * PSF[x,y;\lambda]\big)\tau_{opt}[\lambda]QE[\lambda]d\lambda. \end{aligned} \quad (3.20)$$

The analogue to this expression in the frequency domain (in the absence of noise) is expressed as:

$$\begin{aligned} S_{volts}[\xi,\eta] &= G_{conv}G_{elec}\frac{F_{fill}T_{int}\pi A_{detector}}{hc(1+4(f\#)^2)} \\ &\int_0^{+\infty}\mathcal{F}\big(L_{aper,FT}[\xi,\eta;\lambda]MTF[\xi,\eta;\lambda]\big)\tau_{opt}[\lambda]QE[\lambda]d\lambda \end{aligned} \quad (3.21)$$

. where $L_{aper,FT}[\xi,\eta;\lambda]$ is the Fourier transform of the sensor reaching radiance [Easton (2005)].

3.3 Incoherent Light and Imaging Systems

A few assumptions need to be made before a model of an incoherent imaging system is built. The first assumption is that that the imaging system can be assumed to be linear and shift-

invariant so that the linear systems approach explained in 3.1 can be used to characterize the system. The second assumption, is that the light is "quasimonochromatic", which means that the band pass, $\Delta\lambda$, is much less than the reference wavelength, λ_0. In more plain terms, this means that the light can be described as a single wavelength but still has a bandwidth broad enough that there will be no interference [Easton (2005)]. This is a valid assumption for much of this work; we will be dealing with light that has 10nm band passes from 400 - 900nm; the motion detection experiment will have 100nm band passes from 400 - 700nm and then a 200nm band pass from 700-900nm.

The impulse response of a single-lens incoherent imaging system at the focal plane can be described as the squared magnitude of the coherent impulse response:

$$\mathfrak{h}[x,y;z_1,f,z_2] = \left|\frac{1}{-\lambda^2{}_0 z_1 z_2} e^{+2\pi i\frac{(z_1+r+z_2)}{\lambda_0}} e^{+i\pi\frac{x^2+y^2}{\lambda z_2}} P\left[\frac{x}{\lambda_0 z_2},\frac{y}{\lambda_0 z_2}\right]\right|^2 \tag{3.22}$$

$$= \left(\frac{1}{\lambda^2{}_0 z_1 z_2}\right)^2 \left|P\left[\frac{x}{\lambda_0 z_2},\frac{y}{\lambda_0 z_2}\right]\right|^2. \tag{3.23}$$

where z_1 is the object distance, z_2 is the image distance, f is the focal length and P is the Fourier transform of the pupil function. Examples of various pupil functions are shown in Section 3.8. If we assume that the object is located at a very large distance from the aperture then $z_2 = f$ (which is always the case for remote sensing) and the above equation can be rewritten as:

$$\mathfrak{h}[x,y;z_1,f,z_2=f] = \left(\frac{1}{\lambda^2{}_0 z_1 f}\right)^2 \left|P\left[\frac{x}{\lambda_0 f},\frac{y}{\lambda_0 f}\right]\right|^2. \tag{3.24}$$

We can get the incoherent optical transfer function ($\mathcal{OTF}$), $\mathfrak{H}$, by separating the magnitude of $\mathfrak{h}$ and then using the Filter Theorem, Transform of a Transform Property, and Transform of a Conjugate Property to find that Eq. 3.24 is equivalently expressed in the frequency

domain as:

$$\mathfrak{H}[\xi,\eta;z_1,f,z_2] = \mathcal{OTF}[\xi,\eta;z_1,f,z_2] = \mathcal{F}\left\{\left(\frac{1}{\lambda^2{}_0 z_1 f}\right)^2 \left|P\left[\frac{x}{\lambda_0 f},\frac{y}{\lambda_0 f}\right]\right|^2\right\} \tag{3.25}$$

$$= \left(\frac{1}{\lambda^2{}_0 z_1 f}\right)^2 \mathcal{F}\left\{P\left[\frac{x}{\lambda_0 f},\frac{y}{\lambda_0 f}\right]P^*\left[\frac{x}{\lambda_0 f},\frac{y}{\lambda_0 f}\right]\right\} \tag{3.26}$$

$$= \left(\frac{f}{z_1}\right)^2 p[-\lambda_0 f\xi,-\lambda_0 f\eta] * p^*[\lambda_0 f\xi,\lambda_0 f\eta] \tag{3.27}$$

$$= \left(\frac{f}{z_1}\right)^2 p[-\lambda_0 f\xi,-\lambda_0 f\eta] \bigstar p[-\lambda_0 f\xi,-\lambda_0 f\eta]. \tag{3.28}$$

This shows that the Fourier transform of the impulse response is the 2-D autocorrelation (represented by the star) of the scaled pupil function. The incoherent modulation transfer function ($\mathcal{MTF}$) is the magnitude of the $\mathcal{OTF}$ normalized to 1. Because the maximum value of autocorrelations is always at the central ordinate ([ξ = 0, η=0]) the $\mathcal{OTF}$ is normalized by this value, as shown below:

$$MTF[\xi,\eta] \equiv \frac{\mathcal{OTF}[\xi,\eta]}{\mathcal{OTF}[\xi,\eta]_{\xi=0,\eta=0}} = \frac{p[-\lambda_0 f\xi,-\lambda_0 f\eta] \bigstar p[-\lambda_0 f\xi,-\lambda_0 f\eta]}{p[-\lambda_0 f\xi,-\lambda_0 f\eta] \bigstar p[-\lambda_0 f\xi,-\lambda_0 f\eta]|_{\xi=0,\eta=0}}. \tag{3.29}$$

One thing worth noting here is that the incoherent MTF for an optical system will have a cutoff frequency. This means that any frequencies higher than this cutoff frequency will NOT pass from the scene radiance through the aperture to the focal plane. The cutoff frequency for a cicular aperture is defined as:

$$\nu_c = \frac{D}{\lambda_0 f} = \frac{1}{\lambda_0 f\#}. \tag{3.30}$$

This is incorporated in the MTF by the scaling factor. If we take for example a system with a circular aperture we can define the pupil function as:

$$p[x,y] = CYL\left(\frac{r}{D}\right). \tag{3.31}$$

where r is the radial coordinate from the center of the cylinder function with diameter D.

The MTF of this function would be defined as:

$$MTF(\rho) = \frac{CYL\left(\frac{\lambda_0 f \rho}{D}\right) \bigstar CYL\left(\frac{\lambda_0 f \rho}{D}\right)}{CYL\left(\frac{\lambda_0 f \rho}{D}\right) \bigstar CYL\left(\frac{\lambda_0 f \rho}{D}\right)\Big|_{\rho=0}}. \tag{3.32}$$

where ρ is the radial frequency domain compliment to r.

For more exotic aperture designs that are not circularly symmetric, such as sparse and segmented apertures, there won't be a single cutoff frequency. Instead there will be a range of frequencies that (if oriented at specific angles) will be passed through the system. This will be discussed in more detail in Section 3.12

3.4 Detector Sampling

Once the radiance at the aperture has propagated threw the imaging system and has been low-pass filtered by the optics, the scene irradiance forms an image on the focal plane. From this point there is a transfer of energy from electromagnetic radiation to a quantifiable electronic form. This transduction of energy is performed by the CCD. The CCD sits on the focal plane and samples the image that is projected onto it. Because the light sensitive area of a single CCD pixel is not a perfect point the spatial variation of the image that falls on the pixel is averaged. Hence the CCD pixel acts as a low pass filter. This section will begin with a brief discussion of ideal sampling for a basis of understanding realistic sampling.

The ideal detector (s[x, Δx]) has an infinite length and is composed of unit-area Dirac delta functions (detector elements e.g. single pixels) spaced at intervals of Δx. This is often known as a COMB function:

$$s_{ideal}[x;\Delta x] = \sum_{n=-\infty}^{\infty} \delta[x - n \cdot \Delta x] \equiv \frac{1}{x} COMB\left[\frac{x}{\Delta x}\right]. \tag{3.33}$$

The sampled signal is then defined as:

$$\mathcal{S}\{f[x]\} = f[x] \cdot s[x;\Delta x] \equiv f_s[x;\Delta x]. \tag{3.34}$$

Sampling theory tells us that as long as the input function f[x] does not contain spatial frequencies greater than $\xi_{Nyquist}$ then the original function can be reconstructed without aliasing. The Nyquist sampling frequency is defined as:

$$\xi_{Nyquist} = \frac{1}{\Delta x}. \tag{3.35}$$

Ideal sampling is completely unrealistic, it is not possible to have a sampling function with infinite support, nor is it possible to have a detector element with an infinitesimally small support. A more realistic example of a detector would include a sampling function that had a finite support and detector elements with a support equal to the sampling function's support or some fraction of the sampling function's support. As was eluded to in the introduction of this section, this will have a detrimental effect on the system MTF because the detected signal at each detector element is the average of the continuos signal over that element. The sampling expressed in Eq. 3.34 takes on a more realistic form in the equation below:

$$\mathcal{S}\{f[x = n_0 \cdot \Delta x;\Delta x]\} = \left(f[x] * \frac{1}{p} RECT\left[\frac{x}{p}\right]\right) \cdot \delta[x - n_0 \cdot \Delta x]. \tag{3.36}$$

where Δx is the spacing between detector element centers (pixel pitch) and p is the width of each detector element. Typically for a CCD the pixel pitch, Δx, and the pixel pitch, p, are about equal. In the next expression $p \equiv \Delta$ x. Also, to make this more realistic the single Dirac delta will be replaced by a COMB function which represents a 1-D detector similar to a push broom array.

$$\mathcal{S}\{f[x;\Delta x]\} = \left(f[x] * \frac{1}{p} RECT\left[\frac{x}{p}\right]\right) \cdot \frac{1}{\Delta p} COMB\left[\frac{x}{\Delta x}\right]. \tag{3.37}$$

The mathematical expression shown above is the realistic sampling of a continuous function f. This is done by convolving the continuous function with a rect function of width p,

followed by the ideal sampling (COMB function) at the centers of each detector. It should be noted that this expression does not account for variations in detector response. Figure 3.1 shows this detector: As stated before the detector elements average (or blur) the con-

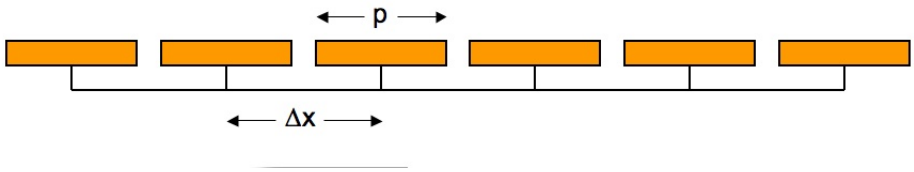

Figure 3.1: Pixel width and pixel pitch are almost equal for CCDs.

tinuous signal f. The MTF of the detector is the Fourier Transform of the RECT function representing the detector:

$$MTF[\xi] = \mathcal{F}\left\{ RECT\left[\frac{x}{p}\right]\right\} = p\ SINC[p\xi]. \tag{3.38}$$

Figure 3.2 shows a portion of a SINC function.

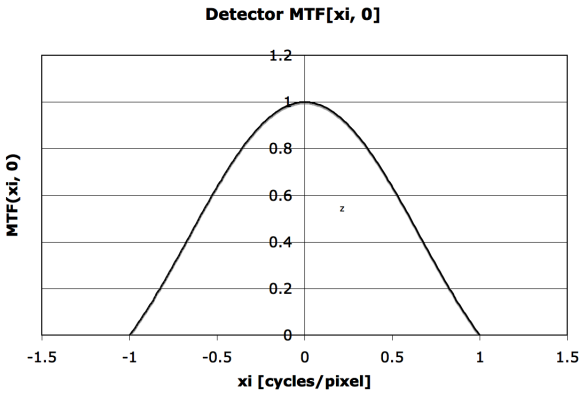

Figure 3.2: A portion of a SINC function that is the detector MTF.

On a 2D array of pixels, one pixel can be represented as a 2D separable function:

$$pixel(x,y) = RECT\left(\frac{x}{p},\frac{y}{p}\right) = RECT\left(\frac{x}{p}\right)RECT\left(\frac{y}{p}\right). \tag{3.39}$$

which can be Fourier transformed to produce the 2D MTF of the detector, shown in Eq. 3.40:

$$MTF_{Detector}(\xi,\eta) = \mathcal{F}\left\{ RECT\left(\frac{x}{p}\right) RECT\left(\frac{y}{p}\right) \right\} = p^2 SINC(p\xi) SINC(p\eta). \quad (3.40)$$

The detector MTF will be entered into the system MTF by multiplying it with the other subsystem MTFs. This will be shown more explicitly in Section 4.2. Section 4.2 also has a plot (Figure 4.2) that shows how much degradation can be attributed to the detector MTF in relation to the other subsystem MTFs. From this plot the reader will notice that the effect of the detector is relatively low for a system operating at Nyquist frequencies.

3.5 Linking the Detector and Optics

Section 3.3 explained the basic Fourier optics behind an incoherent imaging system; perhaps the most important equation in Section 3.3 (for this section) is the equation for optical cutoff frequency, ν_c:

$$\nu_c = \frac{D}{\lambda f} = \frac{1}{\lambda F\#}. \quad (3.41)$$

Section 3.4 presented the basics behind realistic sampling behind the CCD. Another very important equation that is found in this section is the equation for the Nyquist sampling limit, $\nu_{Nyquist}$:

$$\nu_{Nyquist} = \frac{1}{2p}. \quad (3.42)$$

These two equations present the highest spatial frequency produceable and the high spatial frequency detectable respectively. An optimal system (a Nyquist limited system) will link these two systems so that the highest spatial frequency produced by the optics is equal to the highest spatial frequency detectable by the CCD. This can be done mathematically by simply setting $\nu_c = \nu_{Nyquist}$ and solving for which ever parameter is undefined.

$$\begin{aligned} \frac{D}{\lambda f} &= \nu_c = \nu_{Nyquist} = \frac{1}{2p} \\ f &= \frac{2Dp}{\lambda}. \end{aligned} \quad (3.43)$$

This equation is very useful for system designers. The above equation was solved for the focal length (f) for a reason. When building a space telescope the most difficult parameter to adjust is the size of the primary mirror (D). The pixel pitch can also be somewhat difficult to change. The easiest parameter to adjust is the focal length because it entails changing the curvature of the mirrors, which is relatively simple. Fiete (1999) discusses Nyquist systems as having $\lambda f\#/p$ values of 2. $\lambda f\#/p$ is the ratio of sampling frequency to optical cutoff frequency.

$$\frac{\lambda f\#}{p} = 2\frac{\nu_{Nyquist}}{\nu_c} \tag{3.44}$$

3.6 System Noise

System noise is a composite of many lesser noise sources. This section will look at the most prominent sources of noise under plausible operation scenarios for Earth observation. Noise ranges can vary depending on illumination conditions or the current state of the space telescope. For example, we should not expect the signal-to-noise ratio (SNR) during daytime surveillance to be equal to the SNR during night time surveillance. Or if the spacecraft is unable to keep the detector at a constant temperature we would expect more noise at warmer temperatures and less noise at lower temperatures. This behavior will be explained in full in the coming sections.

To model the system noise the individual noise sources must be defined and somehow combined to give us the total amount of noise. This can be done by making two assumptions. The first assumption being that each noise parameter abides by random Gaussian statistics (except for the photon noise) and can be quantified by its standard deviation ($\sigma_{noisesource}$). The second assumption is that the individual noise components are statistically independent. This allows each noise component to be added in quadrature to produce the total system noise [Strojnik and Anderson (2002)].

$$\sigma_{total} = \left(\sum_{i=1}^{N}\sigma_i^2\right)^{1/2} = \left(\sigma_{photon}^2 + \sigma_{read}^2 + \sigma_{dark}^2 + \sigma_{chain} + \sigma_{quatization}^2\right)^{1/2} \tag{3.45}$$

where five statistically independent sources of noise have been identified as photon noise (σ_{photon}), dark current noise (σ_{dark}), read noise (σ_{read}), electronic chain noise (σ_{chain}), and quantization noise ($\sigma_{quantization}$). The following subsections will describe each noise source in detail.

3.6.1 Photon Noise

Due to random fluctuations in photon arrival rate there is an uncertainty value associated with the number of photons reaching the detector. Because photon arrival is a discrete process over a fixed integration time where only an average value of the actual number of photons can be calculated from the detected signal, it is said that photon arrival adheres to Poisson statistics. A property of Poisson statistics is that the standard deviation of an occurrence is the square root of the number of occurrences. Therefore, the standard deviation associated with photon arrival rate is the square root of the signal in electrons (Eq. 3.15):

$$\sigma = \left(S_{electrons}\right)^{1/2}. \tag{3.46}$$

Photon noise is usually the dominating noise source when there is a large amount of light entering the aperture. Whether or not it is the dominating noise source of course depends on the magnitude of the other radiation independent noise sources; we will see later in Section 4.4 that different detectors have different amounts of noise.

3.6.2 Dark Noise

This noise source is a detector specific characteristic and is given or can be calculated from values given in a detector performance specifications sheet. This noise can be observed when there is no flux incident on the detector and is caused by imperfections in the crystalline structure of the detector. Thermally generated electrons become captured in the CCDs depletion region and are read out with the other photo-generated electrons. The amount of dark noise

on a given CCD is dependent upon integration time and CCD temperature:

$$\sigma_{dark} = \frac{J_{dark} 2^{\frac{T-T_{ref}}{T_{double}}} (n_{TDI} + 1) A_{det} T_{int}}{q} \tag{3.47}$$

where J_{dark} is the classic temperature-dependent dark current density (typically in nA/cm^2) measured at reference temperature T_{ref}, T is the temperature of the detector, T_{double} is the dark current doubling temperature, A_{det} is the area of the detector, T_{int} is the integration time, q is the charge of one electron, and n_{TDI} is the number of time delay integration (TDI) stages (unity for staring sensor). The parameters of the above equation are sometimes not given in performance specifications sheets, there are luckily other ways of computing σ_{dark}:

$$\sigma_{dark} = \sqrt{T_{int} \left(\frac{Dark\ Signal\ Integration[\mu V/s]}{Output\ Sensitivity[\mu V/e^-]} \right) 2^{\frac{T-T_{ref}}{T_{double}}}}. \tag{3.48}$$

The *Dark Signal Integration* is the amount of dark signal over a given amount of time. By dividing by the output sensitivity the number of dark signal electrons per second are calculated. Similar to the classic-temperature-dependent dark current density from Eq. 3.47 the dark signal integration is dependent on temperature and has a doubling temperature. Due to the Poisson nature of the electron arrival, the square root is taken to find the standard deviation of the dark current.

Another parameter that is sometimes given in the performance specifications sheet is the Dark Signal $[e^-/s]$. The standard deviation of the dark current is calculated using this value in a similar fashion:

$$\sigma_{dark} = \sqrt{T_{int} \cdot Dark\ Signal[e^-/s] \cdot 2^{\frac{T-T_{ref}}{T_{double}}}}. \tag{3.49}$$

Often times CCDs have special light shielded pixels on the side of the chip that can be used to make measurements of dark signal, which can subsequently be used to calculate σ_{dark}.

3.6.3 Read Noise

Another prevalent type of noise is read noise; read noise is similar to dark noise in that it is independent of the flux onto the detector. The difference is in its origin as it is created by the CCD readout electronics. A value for read noise can usually be found in the CCD performance specifications sheet and is given in units of rms electrons. This term tends to be constant through the imaging system and can be treated as a biasing term in the total noise.

3.6.4 Signal Chain Noise

The signal chain noise - similar to the read noise - can also be treated as a biasing term in the total noise. This noise source is a combination of all the analog signal processing components from the readout to the A/D converter. This noise source can be measured in volts; Strojnik and Anderson (2002) explains that it can be converted to electrons applying the inverse of the products of the electronic and conversion gain terms.

$$\sigma_{chain,electrons} = \frac{\sigma_{chain,Volts}}{G_{elec}G_{conv}} \tag{3.50}$$

3.6.5 Quantization Noise

Finally, at the A/D converter there is a noise source associated with the digitization of the analog signal. Because the input into the A/D converter is continuous and then quantized into discrete bins there is a residual error or uncertainty in the new digital signal. The quantization of signal can potentially result in a loss of information depending on the bit number of the A/D converter and the prior noise sources. Strojnik and Anderson (2002) explains that if one assumes that the quantization is uniformly distributed and because the standard deviation of a uniform distribution is $1/\sqrt{12}$ then the rms electrons can be expressed as:

$$\sigma_{quan} = \frac{S_{ADC}}{2^n G_{conv} G_{elec} \sqrt{12}} = \frac{QSE}{\sqrt{12}}. \tag{3.51}$$

where S_{ADC} is the A/D converter input voltage range, *n* is the number of binary digits associated with the A/D converter (bit number), and “QSE is the quantum step equivalence or

effective bin size of the quantization scheme in rms electrons per count" [Introne (2004)].

3.6.6 Total Noise

The total system noise was written out in equation 3.45; however, this was only for a single pixel. As one might imagine, these noise components will vary spatially over a 2-D array of pixels due to either their random nature or the physical nature by which they are generated. Introne (2004) suggests:

$$\begin{aligned} n_{total}[x,y] \cong\ & \mathcal{P}\{s^{\ell}_{electrons}[x,y] * \mathfrak{h}^{\ell}[x,y]\} + \sigma_{dark} n_2[x,y] + \\ & \sigma_{read} n_3[x,y] + \sigma_{quan} n_4[x,y] + \sigma_{chain} n_5[x,y]. \end{aligned} \tag{3.52}$$

where the photon noise is modeled as the signal in electrons from spectral band ℓ convolved with the system PSF for spectral band ℓ ($\mathfrak{h}^{\ell}(x,y)$) and then operated on by the Poisson operator $\mathcal{P}$. n_i is a statistically independent Gaussian function with zero mean and unit variance. Multiplying n_i by the standard deviation of a noise source then creates a 2-D function with a zero mean and standard deviation equal to that of the noise source it represents. The total noise in the frequency domain is calculated by Fourier transforming each term:

$$\begin{aligned} N_{total}[\xi,\eta] \cong\ & \mathcal{F}\{\mathcal{P}\{S^{\ell}_{electrons}[\xi,\eta] * \mathfrak{h}^{\ell}[\xi,\eta]\}\} + \sigma_{dark} N_2[\xi,\eta] + \\ & \sigma_{read} N_3[\xi,\eta] + \sigma_{quan} N_4[\xi,\eta] + \sigma_{chain} N_5[\xi,\eta]. \end{aligned} \tag{3.53}$$

The two expressions are equivalent, however in the modeling situation described here the first expression in Eq. 3.52 will be used.

3.6.7 Signal-to-Noise Ratio

The signal-to-noise ratio (SNR) of an image is going to be a very important parameter in this research. The SNR is a value that defines how strong the signal is compared to the system noise. Imagine imaging a flat gray scene, a system that has a low SNR would create an image that has a high standard deviation about the mean. Conversely, a system that has a high SNR would produce an image that has low standard deviation about the mean. If you swapped

out this gray scene for a more interesting image you would notice that the high SNR system is going to have a nice sharp quality while the low SNR system (provided the SNR is low enough) is going to have a "grainy" less sharp quality.

There are numerous ways of defining the SNR (see Leachtenauer et al. (1997)). The method used in this research is to take the scene-wide mean of the signal in electrons $S_{electrons}$ (from Eq. 3.20) and then divide by the scene-wide standard deviation of the total noise, $std\{n_{total}(x,y)\}$ (from Eq. 3.52) [Introne (2004)]. This can be done because we are working with synthetic data that has no noise. Observe Eq. 3.54.

$$SNR = \frac{mean\{S_{electrons}(x,y)\}}{std\{n_{total}(x,y)\}} \tag{3.54}$$

3.7 Image Restoration

In Sections 3.1 and 3.4, it was shown that the pupil function and the detector act as low pass filters on the radiance entering the aperture and flux incident onto the detector. In the previous section, Section 3.6 the degraded image was further degraded by noise inherent in the system. This section will describe a technique to high-boost filter the image and restore some of the attenuated signal information. Let us revert back to the simple notation used in Section 3.1 to write out the mathematical description of an imaging system with additive noise:

$$g[x] = f[x] * h[x] + n[x] \tag{3.55}$$

$$G[\xi] = F[\xi] \cdot H[\xi] + N[\xi]. \tag{3.56}$$

The idea presented in this section is that a linear filter, *w*, can be derived that will use *a priori* knowledge of the system MTF (or PSF) to produce an estimate of f[x] ($\hat{f}$[x,y]) from the output g[x]. Easton (2005) describes the action of this filter as:

$$g[x] * w[x] = f[x] * h[x] * w[x] + n[x] * w[x] = \hat{f}[x] \tag{3.57}$$

$$G[\xi] \cdot W[\xi] = F[\xi] \cdot H[\xi] \cdot W[\xi] + N[\xi] \cdot W[\xi] = \hat{F}[\xi]. \tag{3.58}$$

Thinking unrealistically and in the frequency domain the above equations could be used to

reconstruct the original input function if the spectra of $F[\xi]$ and $N[\xi]$ were *disjoint*; meaning that where $|N[\xi]|$ = 0 then $|F[\xi]| \neq 0$ and where $|F[\xi]|$ = 0 then $|N[\xi]| \neq 0$. This would allow Eq. 3.57 to satisfy these two conditions:

$$N[\xi] \cdot W[\xi] = 0[\xi] \tag{3.59}$$

$$F[\xi] \cdot W[\xi] = F[\xi]. \tag{3.60}$$

A Wiener Filter, in this case, equal to 1 would satisfy these conditions. In a more realistic scenario the spectra of the noise and signal, $N[\xi]$ and $F[\xi]$, will never be equal to 0; therefore, a Wiener Filter that accounts for both the disjoint and overlapping of the signal and noise spectra is necessary. This causes us to think of what characteristics a Wiener Filter might have. First of all spatial frequencies that contain large amounts of noise power and low amounts of signal power should not be transmitted by the filter:

$$where\ |N[\xi]|^2 >> |F[\xi]|^2 \Rightarrow W[\xi] \cong 0. \tag{3.61}$$

This can be rearranged as an expression that is small in this region:

$$1 >> \frac{|F[\xi]|^2}{|N[\xi]|^2} \cong 0\ if\ |N[\xi]|^2 >> |F[\xi]|^2. \tag{3.62}$$

And at spatial frequencies where the noise power is much less than the signal power, the Wiener Filter should be approximately unity so that most of the useful frequencies are transmitted.

$$|N[\xi]|^2 << |F[\xi]|^2 \Rightarrow W[\xi] \cong 1 \tag{3.63}$$

Norbert Wiener proved a relation that provided a smooth transition between the two conditions defined by Eq. 3.62 and Eq. 3.63. The conclusion of his proof showed that the "appropriate relation to minimize the squared error is the reciprocal of the sum of the recip-

rocals of the two limiting cases." This expression can be written in multiple ways:

$$W[\xi] = \left[\left(\frac{|F[\xi]|^2}{|F[\xi]|^2}\right)^{-1} + \left(\frac{|F[\xi]|^2}{|N[\xi]|^2}\right)^{-1}\right]^{-1} \tag{3.64}$$

$$= \left[(1)^{-1} + \left(\frac{|F[\xi]|^2}{|N[\xi]|^2}\right)^{-1}\right] \tag{3.65}$$

$$= \frac{1}{1+\frac{|N[\xi]|^2}{|F[\xi]|^2}} \equiv \frac{1}{1+\Gamma[\xi]} \tag{3.66}$$

$$= \frac{|F[\xi]|^2}{|F[\xi]|^2 + |N[\xi]|^2}. \tag{3.67}$$

where $\Gamma[\xi] \equiv \frac{|N[\xi]|^2}{|F[\xi]|^2}$ is the *noise-to-signal power ratio*.

Later, Carl Helstrom constructed the Wiener-Helstrom Filter using complete knowledge of the system transfer function, an estimate of the noise spectrum, and an assumed or modeled version of the power spectrum. To do this derivation Helstrom defined limiting cases similar to those defined in Eq. 3.62 and Eq. 3.63, though this time it included the effects of the system transfer function. He then solved to find the appropriate relation that minimized the squared error between the two limiting cases.

When working with the Wiener Filter, the ratio of the power spectra was needed to determine the scaling factors between limiting cases. Again, this is needed but now the contribution from the system transfer function ($H[\xi]$) is also needed. The first condition states, when $|F[\xi] \cdot H[\xi]|^2 << |N[\xi]|^2$ then:

$$\begin{aligned} N[\xi] \cdot W[\xi] \quad &= 0 \cong \frac{1}{H[\xi]}\left(\frac{|F[\xi] \cdot H[\xi]|^2}{|N[\xi]|^2}\right) if\ |F[\xi] \cdot H[\xi]|^2 << |N[\xi]|^2 \\ &= H^*[\xi] \cdot \left(\frac{|F[\xi]|^2}{|N[\xi]|^2}\right) = H^*[\xi] \cdot (\Gamma[\xi])^{-1}. \end{aligned} \tag{3.68}$$

The second condition states, where $|F[\xi] \cdot H[\xi]|^2 >> |N[\xi]|^2$, the Wiener filter becomes a

simple inverse filter:

$$\hat{F}[\xi] = G[\xi] \cdot W[\xi] = F[\xi] \cdot H[\xi] \cdot W[\xi] = F[\xi] \; if \; |F[\xi] \cdot H[\xi]|^2 >> |N[\xi]|^2$$
$$\Rightarrow W[\xi] \cong \frac{1}{H[\xi]} \cdot \left(\frac{|F[\xi] \cdot H[\xi]|^2}{|F[\xi] \cdot H[\xi]|^2} \right) = \frac{1}{H[\xi]} \tag{3.69}$$

These two boundaries are then brought together the same way that was used for the Wiener Filter.

$$W[\xi] = (|F[\xi]|^2) \left[\left(\frac{H[\xi]^{-1}}{|F[\xi]|^2} \right)^{-1} + \left(\frac{H^*[\xi]}{|N[\xi]|^2} \right)^{-1} \right]^{-1} \tag{3.70}$$
$$= \frac{H^*[\xi]}{|H[\xi]|^2 + \Gamma[\xi]|} \tag{3.71}$$

Because the exact forms of the power spectra of the signal and noise are not known it can be assumed that they have a constant ratio. An approximation to the Wiener-Helstrom Filter called the Constrained Least-Squares Filter can be constructed using the assumption that the parameter Γ, the noise-to-signal power ratio, is constant. Determination of Γ is done experimentally, this process is discussed in Section 4.7. The Constrained Least Squares Filter is shown in Eq. 3.72.

$$W[\xi] = \frac{H^*[\xi]}{|H[\xi]|^2 + \Gamma} \tag{3.72}$$

Another important point is that in a realistic situation there is never full knowledge (if any knowledge) of the pupil phase or its subsequent effect on the transfer function, H, used in this equation. The system model will have the ability to build restoration filters that are partially derived from pupil functions that have a user specified degree of aberration knowledge. Section 4.5 discusses how the user can define pupil function knowledge, and Section 4.7 discusses the importance of aberration knowledge in this work. It should also be noted that there are techniques available for determining aperture aberrations [Daniel (2009)].

3.8 Apertures

In the previous sections much of the basic theory that will enable successful imaging system modeling has been described. The remaining sections shall explain how the model can be made more realistic. Section 3.3 displayed the importance of the pupil function to the system's MTF. This section will focus on the different types of pupils that will be used in this project.

Each pupil is initially modeled as a simple real-valued "zero-one" function. This represents a perfect pupil with no aberations. In the real world a pupil will have aberrations, this will be discussed in detail later in Section 3.9. Figure 3.3 shows side profiles of the three different types of telescopes that will be modeled. Figure 3.3 a) is a conventional Cassegrain telescope with a large monolithic primary mirror and a smaller secondary mirror along the optical axis.

Figure 3.3 b) shows a sparse (or dilute) aperture telescope. This is a modern design that can have two or more smaller sub-apertures; each sub-aperture is a miniature Cassegrain telescope. Light from each telescope is then combined at the focal plane to achieve a spatial resolution that is higher than that of a single sub-aperture. The sparse aperture design has some advantages over the traditional Cassegrain for Earth observation and astronomy. The main advantage of these systems for space-borne applications is size and weight because they can be designed so that they are "foldable" allowing them to be larger and still capable of being placed aboard a launch vehicle. After deployment they can unfold to have an effectively very large aperture that would otherwise not be possible with current launch technology. In addition to this the sub-apertures are less expensive and easier to manufacture. There are of course disadvantages to this system. The main problem is phasing the apertures; once the telescope has unfolded the sub-apertures will not be aligned properly. Actuators will be required to control the exact alignment of each sub-aperture. The sparse aperture systems suffer from additional problems related to the reduced fill factor which results in a lower SNR. Lastly, the MTF for these types of systems will often severely attenuate many spatial frequencies. This is easily seen in the MTF of the triarm (Figure 3.8) and the annulus (Figure 3.9).

Figure 3.3 c) shows a segmented aperture system. This system can be thought of as a

compromise between the Cassegrain and the sparse systems. Here we have a large segmented primary aperture with a fill factor comparable to the Cassegrain. The segmented aperture, similar to the sparse aperture, is foldable and therefore easily placed on a launch vehicle, but the system might have to have lightweight optics in order to satisfy the launch vehicle's weight contraints. This system will also suffer from the same phasing problems that the sparse aperture design did.

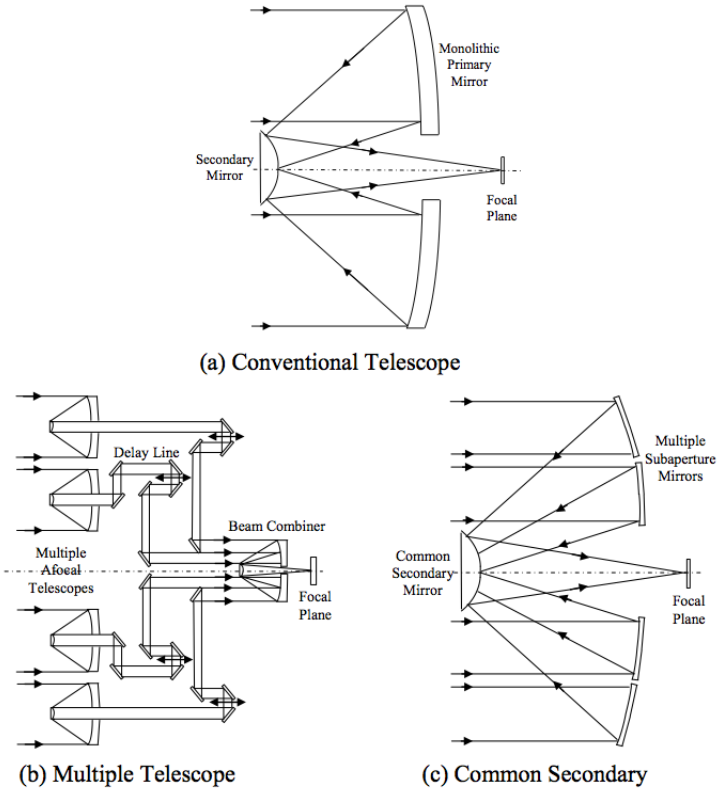

Figure 3.3: Side profile for three telescope designs [Introne (2004)].

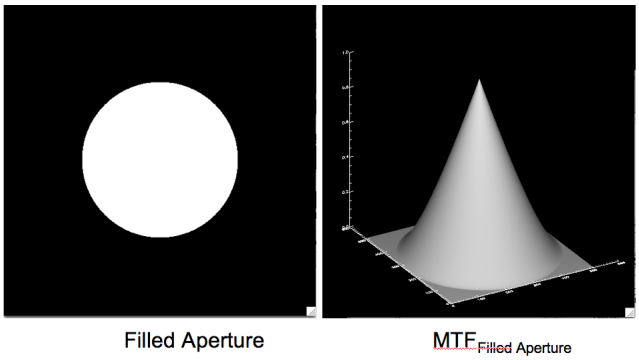

Figure 3.4: Filled Aperture. We start out with a full aperture and move to the more exotic segmented and sparse designs.

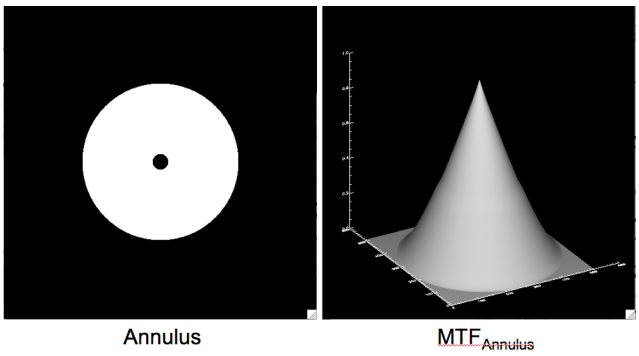

Figure 3.5: Cassegrain Aperture

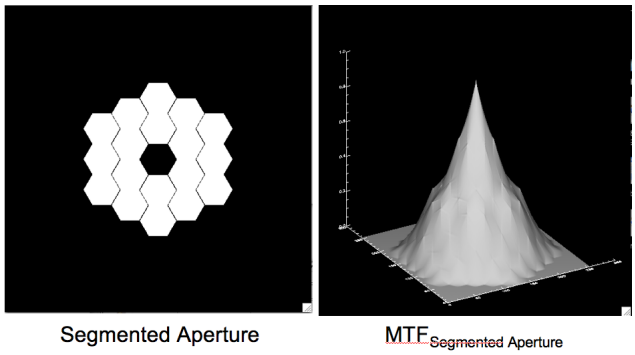

Figure 3.6: Segmended Aperture

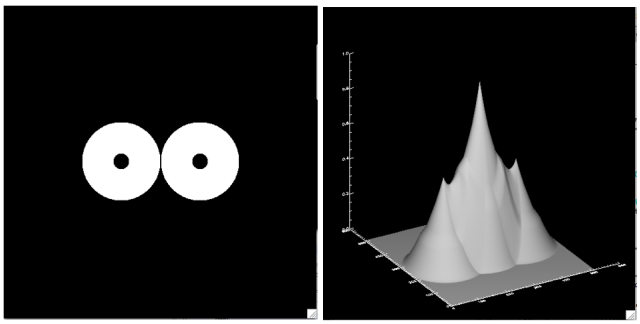

Figure 3.7: Bi Aperture

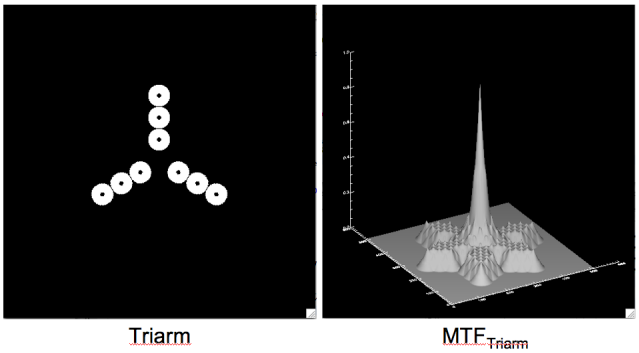

Figure 3.8: Triarm Aperture

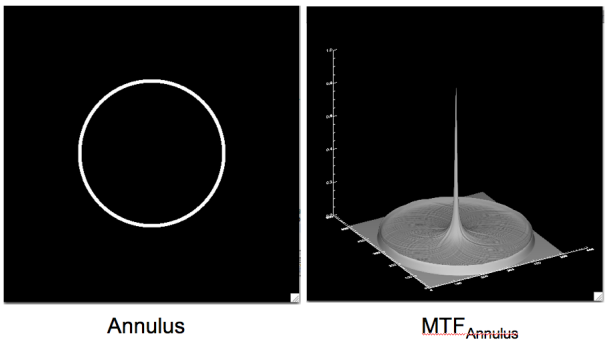

Figure 3.9: Annulus

3.9 Aperture Aberrations

In Section 3.8, several different types of apertures were shown with their MTFs. In that section, the pupil functions were modeled so that the spherical nature of the light would be unperturbed after reflection. The idea of a mirror with no aberrations that could preserve the spherical nature of light is rather unrealistic as aberrations are found in all lenses and mirrors. In this document we are presented with a slightly more exotic imaging scenario that includes segmented and sparse aperture systems. These systems are composed of smaller subapertures that work in concert to achieve the performance of a larger monolithic aperture. The smaller subapertures could in theory be aberration free and yet still not provide optimal performance because they are not aligned properly. For example, a subaperture could be tipped, tilted, or have a piston error. These would be considered aberrations on a multi-aperture system and would effectively degrade the MTF and output. To make the system completely realistic we would need to introduce aberrations in the subapertures that are exhibited in real mirrors. Simple mirrors contain aberrations such as spherical, aspherical, coma, astigmatism, etc. Many of these types of aberrations can be modeled using Sidel or Zernike Polynomials. Other more complex lightweight mirrors that are very attractive for space-borne applications contain aberrations that are not well explained using polynomials. To model these types of aberrations we may need to look elsewhere or obtain an optical path difference map of the mirror segment.

As was stated earlier the MTF is calculated by performing an autocorrelation on the scaled pupil function. If the scaled pupil function includes information about the mirror's aberrations, how does this impact the MTF and image quality? This section will cover geometric aberrations and how they degrade the MTF.

Goodman (1996) explains that optical path difference (OPD) error can be incorporated into the Fourier optical model through the complex pupil function as a phase term. This is done by breaking the pupil function into its magnitude and phase and then adding the wavefront error to the existing phase. In the case where there is no pre-existing phase the expression looks like:

$$p_{aber}[x, y] = p[x, y] \cdot e^{\frac{2\pi i}{\lambda_0} w[x.y]} \tag{3.73}$$

where $w[x, y]$ is a 2-D function that describes the OPD in units of wavelength, λ_0. This equation can be adapted to suit segmented and sparse aperture systems by introducing shift parameters (x_i, y_i) for the centers of the i^{th} subaperture.

$$p_{aber}[x, y] = p[x, y] \cdot e^{\frac{2\pi i}{\lambda_0} w_i[x-x_i, y-y_i]} \tag{3.74}$$

Just so the reader can get a more complete understanding of the importance of aberrations, the different types of aberrations, and what effect they might have on image quality, an example is presented in Figure 3.10. Here we have a Bi-aperture sparse aperture system with the left mirror severely tilted. As one might expect the model output has a double image.

To create a realistic MTF for a system including a pupil function with aberrations and phase error, one simply needs to replace all zero-one pupil masks with the complex pupil function expressed in Eq. 3.73. The following subsections will present the traditional Zernike Polynomials, a interferogram from a light weight mirror, and a novel technique used to generate aberrations similar to those of the light weight mirror.

3.9.1 Zernike Aberrations

To model simple aberrations the two most commonly used approaches are through Seidel and Zernike polynomials. This discussion will focus on Zernike polynomials because they can produce aberrations similar to those observed in optical tests [Wyant and Creath (1992)]. Wyant explains that Zernike polynomials are not necessarily the best polynomials for fitting data or generating typical aberrations, he goes on to provide his readers with multiple examples of why this is so. They are however quite easily implemented and are used frequently in the remote sensing and space telescope communities. Eq. 3.75 shows 36 Zernike Polynomials.

The aberrations are usually good enough to simulate phase errors in large rigid optics, however they are not useful for the abnormal aberrations found in light weight nano laminate mirrors.

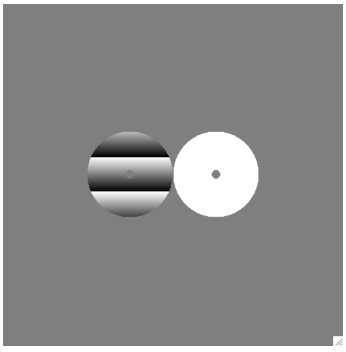

(a) Bi Aperture with large amount of tilt error on left aperture.

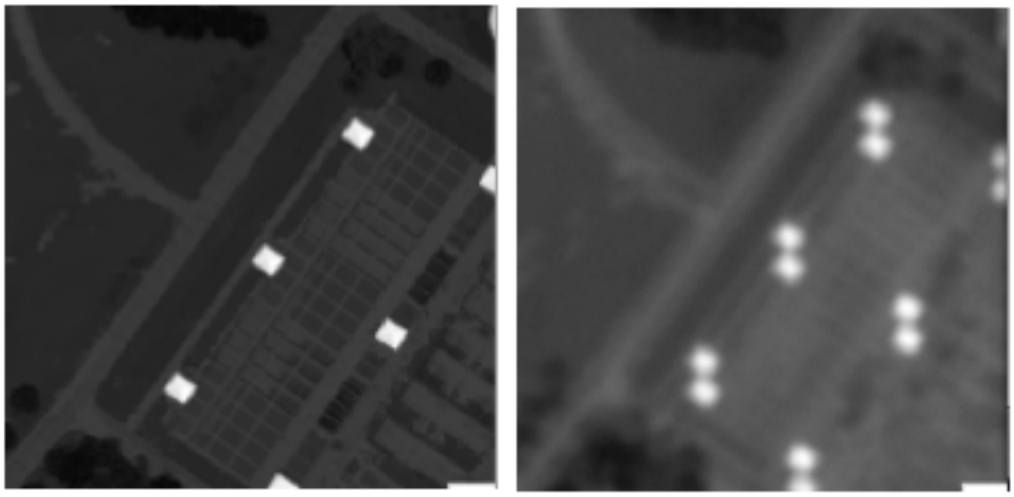

(b) Pan-chromatic image before and after the being processed by the model. Notice that there is now a double image effect caused by the tilted aperture.

Figure 3.10: Proof of concept Bi-aperture test.

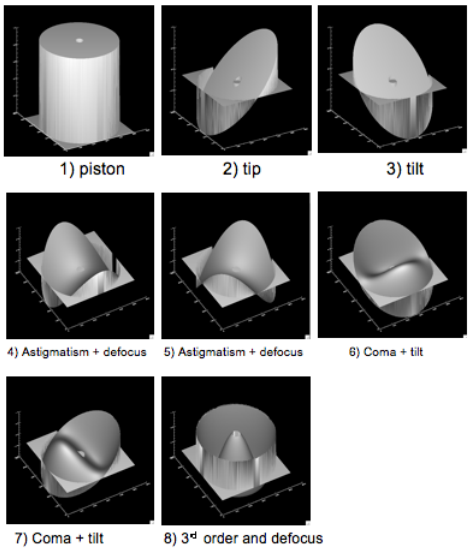

Figure 3.11: The first 8 Zernike Polynomials

$$
\begin{aligned}
WFE(\rho,\theta) \quad = \quad & 1 \\
& +\rho * cos(\theta) \\
& +\rho * sin(\theta) \\
& +(2 * \rho^2 - 1) \\
& +(\rho^2) * cos(2 * \theta) \\
& +(\rho^2) * sin(2 * \theta) \\
& +(3 * (\rho^2) - 2) * \rho * cos(\theta) \\
& +(3 * (\rho^2) - 2) * \rho * sin(\theta) \\
& +(6 * (\rho^4) - 6 * (\rho^2) + 1) \\
& +(\rho^3) * cos(3 * \theta) \\
& +(\rho^3) * sin(3 * \theta) \\
& +(4 * (\rho^2) - 3) * (\rho^2) * cos(2 * \theta) \\
& +(4 * (\rho^2) - 3) * (\rho^2) * sin(2 * \theta) \\
& +(10 * (\rho^4) - 12 * (\rho^2) + 3) * \rho * cos(\theta) \\
& +(10 * (\rho^4) - 12 * (\rho^2) + 3) * \rho * sin(\theta) \\
& +(20 * (\rho^6) - 30 * (\rho^4) + 12 * (\rho^2) - 1) \\
& +(\rho^4) * cos(4 * \theta) \\
& +(\rho^4) * sin(4 * \theta) \\
& +(5 * (\rho^2) - 4) * (\rho^3) * cos(3 * \theta) \\
& +(5 * (\rho^2) - 4) * (\rho^3) * sin(3 * \theta) \\
& +(15 * (\rho^4) - 20 * (\rho^2) + 6) * (\rho^2) * cos(2 * \theta) \\
& +(15 * (\rho^4) - 20 * (\rho^2) + 6) * (\rho^2) * sin(2 * \theta) \\
& +(35 * (\rho^6) - 60 * (\rho^4) + 30 * (\rho^2) - 4) * \rho * cos(\theta) \\
& +(35 * (\rho^6) - 60 * (\rho^4) + 30 * (\rho^2) - 4) * \rho * sin(\theta) \\
& +(70 * (\rho^8) - 140 * (\rho^6) + 90 * (\rho^4) - 20 * (\rho^2) + 1) \\
& +(\rho^5) * cos(5 * \theta) \\
& +(\rho^5) * sin(5 * \theta) \\
& +(6 * (\rho^2) - 5) * (\rho^4) * cos(4 * \theta) \\
& +(6 * (\rho^2) - 5) * (\rho^4) * sin(4 * \theta) \\
& +(21 * (\rho^4) - 30 * (\rho^2) + 10) * (\rho^3) * cos(3 * \theta) \\
& +(21 * (\rho^4) - 30 * (\rho^2) + 10) * (\rho^3) * sin(3 * \theta)
\end{aligned}
$$

3.9.2 Interferogram Measurement

The surface plot in Figure 3.12 shows an interferogram of a 24 inch hexagonal light weight mirror meant for a space-borne telescope. The interferogram was obtained through Lewis (2008) at ITT Space Systems. These light weight optics use nonrigid nano-laminant technology that can have unusual aberrations caused by the manufacturing process. The problem is that these aberrations are poorly described by polynomial techniques such as Zernikes. A different technique proposed in the next section could be used to describe the aberrations found in light weight optics.

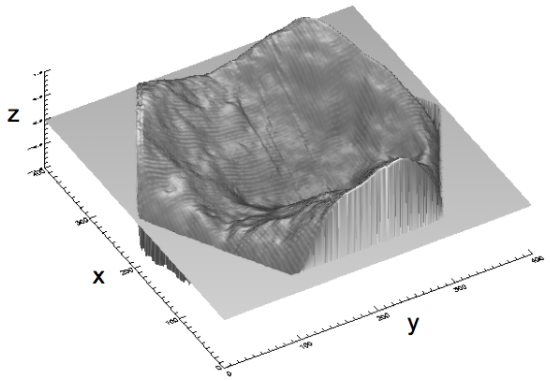

Figure 3.12: A surface plot of the interferogram.

3.9.3 Fractional Brownian Motion Based Aberrations

The author noticed that the interferogram shown in Figure 3.12 has some visual (not necessarily mathematical) resemblance to fractional Brownian motion (fBm). There are several implementations of fBm that are commonly used to make clouds or mountainous terrain in computer graphics [Barnsley et al. (1988)]. The ability to produce OPD maps quickly with similar characteristics to the interferogram measurement could be useful and fBm can provide this easily. A quick and easy way of doing this is by using a Fast Fourier Transform filtering algorithm to produce a surface that can be used as an OPD map. The algorithm begins by constructing a 2D complex "white noise" function, W(ρ). W(ρ) is filtered with a

transfer function T(ρ), where T(ρ) is defined as:

$$T(\rho) = \frac{1}{\rho^{\frac{\beta}{2}}}. \tag{3.76}$$

where β is related to the fractal dimension by:

$$D = E + \frac{3-\beta}{2}. \tag{3.77}$$

where E = 2 for images [Zwiggelaar and Bull (4-6 July 1995)]. In this effort D and E will be ignored and only β will be used to describe the shape. After T(ρ) is used to filter W(ρ) the output is inverse Fourier transformed to produce a 2D array that has a power spectrum proportional to the spatial frequency raised to the power -$\beta/2$. This shows that for a true fractal image the fractal dimension could be determined, and in this case the fractal dimension of the **mirror** could be determined. This would be a wonderful accomplishment, however the mirrors are **not** true fractals and their fractal dimension cannot be determined using these techniques. The fBm algorithm does produce surfaces that are visually similar to the light weight mirror interferogram. For example, observe Figure 3.13, the upper left aperture was made from Zernikes, the upper right was taken from the interferogram, and the bottom two were generated using the fractional Brownian motion approach. Control over the surface roughness is determined by the β value. A larger β value produces a smoother surface because the higher spatial frequencies are attenuated more by the transfer function, in Eq. 3.76. See Figure 3.14 for examples of different surface roughness. This work is presented here as a demonstration and was not used in any of the experiments presented in Chapter 6.

3.10 Jitter

A space telescope's body has mechanical moving parts that create vibrations through the structure. These vibrations disrupt the pointing stability of the telescope and cause the image to blur. The traditional approach to modeling the MTF of the jitter is done by assuming the line of sight vibrations have a high frequency in comparison to the integration time T_{int}; thus allowing the assumption that platform jitter can be described by an isotropic random variable

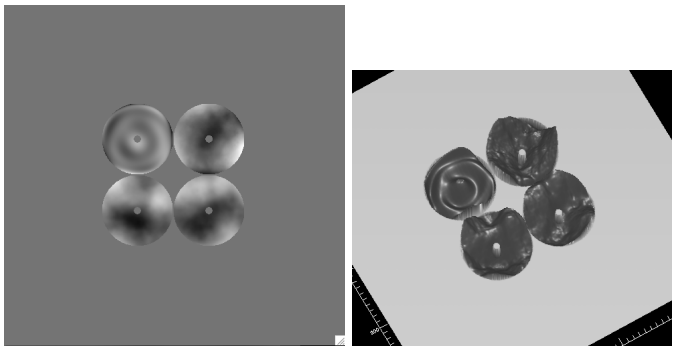

(a) Top view (b) Side view

Figure 3.13: interferogram

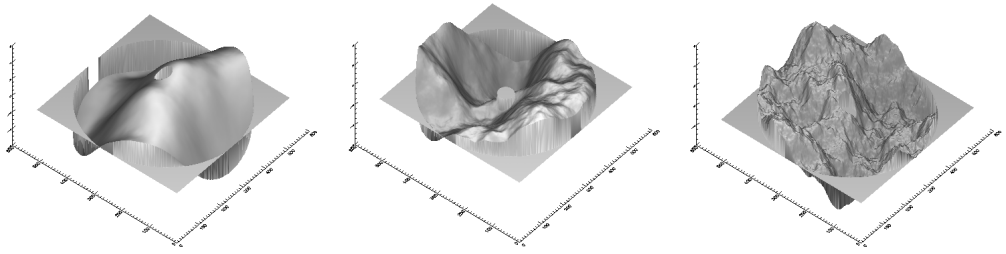

(a) $\beta/2 = 3.333$ (b) $\beta/2 = 2.703$ (c) $\beta/2 = 2.243$

Figure 3.14: This example shows how the roughness of the surface can be altered by changing the β-value.

that abides by Gaussian statistics over T_{int}. It is therefore possible to model the MTF as a Gaussian function:

$$MTF_{jitter} = e^{-2\pi^2\sigma_{jitter}^2(\xi^2+\eta^2)}. \tag{3.78}$$

where σ_{jitter} has units of mrad and is the standard deviation of the observed random line of sight jitter. A σ_{jitter} value that produces a jitter less than $1/10^{th}$ of a pixel is considered to be unperceivable. Finally, it should be noted that jitter is not dependent upon wavelength and is therefore not scaled with the aperture MTF in the polychromatic model.

3.11 The Polychromatic Model

Changing the model to enable polychromatic imaging is another step towards a realistic imaging scenario. In Section 3.5 it was shown how the optics were matched to the detector at the wavelength, λ_0, so that the Nyquist sampling criterion discussed in Section 3.4 would be satisfied. When the model is extended to wavelengths outside of the intended bandpass the frequency information in the incident irradiance changes. Higher spatial frequencies are found at lower spectral wavelengths and lower spatial frequencies are found at higher spectral wavelengths. This relationship can be seen in the wavelength dependence of the incoherent MTF seen in Eq. 3.29; the support of the scaled pupil function can extend to higher spatial frequencies because of a lower spectral wavelength and to lower spatial frequencies at the higher spectral wavelength. One might also argue that this makes intuitive sense because the pupil will appear larger to a blue photon and smaller to a red photon and when they are auto-correlated the MTF will be wider for the blue photon and narrower for the red.

As one might imagine this spectral dependence creates a problem because the system no longer satisfies the Nyquist sampling criterion. If the system is designed for green light ($\lambda = 550nm$) the blue light ($\lambda = 450nm$) may contain frequencies higher than the Nyquist frequency, these frequencies will be aliased by the detector. On the other hand, that maximum spatial frequency produced by the red light ($\lambda = 650nm$) will be lower than the Nyquist frequency and therefore the red light will be under-sampled. A discussion of how this is handled is found in the Approach chapter in Section 4.6.1. This was a topic of major interest in the research performed by Block (2005).

The other part of the model that changes with wavelength is the aberrations. The same intuitive understanding that was used on the scaled pupil function can be used here. Aberrations look much smaller for larger wavelengths than smaller wavelengths. For example, a photon of wavelength 500nm observes a piston error of 1/2 waves; this same piston error for a wavelength of 1000nm is only 1/4 waves. The pupil function for each band can be redefined using the equation below:

$$p(x,y) = |p(x,y)|e^{\frac{2\pi i}{\lambda_0} WFE(x,y)\left(\frac{\lambda_0}{\lambda_l}\right)}. \tag{3.79}$$

An interesting paradox can be observed from the spectral dependence of the MTF and wavefront error (WFE). As the wavelength of light decreases the high spatial frequencies get passed to the focal plane, which can manifest higher image quality provided the detector is capable of sampling the higher spatial frequencies. At the same time this decrease in wavelength will cause the wavefront error to increase which will have a negative effect on image quality. Therefore there is a design tradeoff between wavelength, aperture size, and aberrations that effect image quality. These design parameters will be part of the trade space for the experiments performed in this thesis. There is a further discussion of this and how it affects the results in Section 5.2.

3.12 Sparse Aperture Issues

3.12.1 Effective Diameter

Due to the geometry of the sparse aperture type telescopes the support of the encircled MTF is less than that of the MTF of the filled aperture. To begin this explanation observe Figure 3.15 that shows a triarm aperture overlaying a filled aperture.

When the filled aperture is autocorrelated to produce its MTF the output is a circular triangle function with a radius (or cutoff frequency, ρ_c) of $\frac{D}{\lambda f}$. The MTF of the triarm however is not circularly symmetric, so it does not have an obvious ρ_c. Also, as stated before the encircled support of the triarm's maximum MTF, ρ_{max}, is less than the encircled support of the filled aperture MTF. Figures 3.5 and 3.8 in Section 3.8 shows surface plots of the

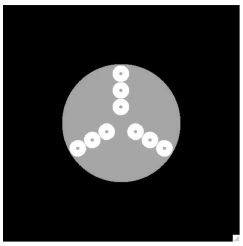

Figure 3.15: Triarm overlaying a filled aperture.

Cassegrain MTF and the triarm MTF.

A thresholded view of the functions is also shown in Figure 3.16.

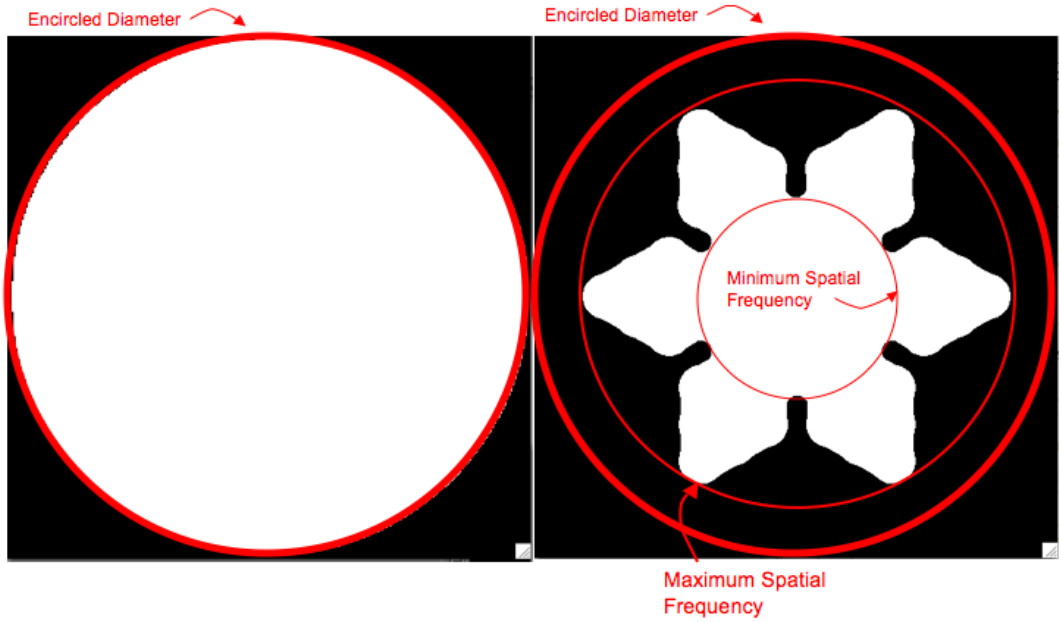

Figure 3.16: Thresholded Cassegrain MTF and triarm MTF.

Circles with radii equal to the radial distance of the minimum and maximum spatial frequencies, ρ_{min} and ρ_{max}, have been drawn. As discussed before, the cutoff frequency, ρ_{max}, is directly related to the diameter of the aperture, what then is the diameter of the aperture when the cutoff frequency is ambiguous like the case presented here with the triarm? Fiete et al. (2002) has shown a variety of ways to calculate the "effective diameter", D_{eff}, for

apertures that don't produce circularly symmetric MTFs. The effective diameter can then be defined as the diameter of a filled aperture that gives the same performance as the sparse aperture. The effective diameter will therefore always be smaller than the encircling diameter of the sparse-aperture.

At first this may seem as if it is a trivial way of analyzing the performance of a system, but when one remembers the discussion presented in Section 3.5 one easily understands the vital importance of the so called "effective diameter" and its relation to the sampling done by the detector. For a sparse aperture system the detector should **not necessarily** be linked to the optics using the method explained in Section 3.5. Instead using the effective diameter may present a more optimal design. Modeling a system designed around an effective diameter, rather than an encompassing diameter, will produce images with a potentially high amount of aliasing. The physical aperture diameter is therefore used in this effort.

3.12.2 Fill Factor vs. Integration Time

When viewing Eq. 3.19 one might believe that the fill factor varies inversely with the integration time to preserve a given image fidelity. Fiete et al. (2002) has shown that this is not necessarily the case as he found that integration times must increase by a factor of at least $1/F^2$. It was determined that different aperture types will require a different change in integration time for a given amount of reduction in fill factor. For example, a psycho-physical test showed that for a $1/F^P$ model the Annulus fit with a P = 3.09 $\pm$ 0.1, where the tri-arm fit with a P = 2.22 $\pm$ 0.1. This research effort will not compare different fill factors for sparse apertures, nor will there be any psycho-physical evaluation involved. This section merely shows the need for a study that compares system parameters, as these models produce unexpected results.

Chapter 4

Approach

This chapter will discuss how the mathematical tools described in the background and theory section were used in the implementation of the model. The first section (4.1) provides a broad overview of the model. The subsequent sections describe the inner workings of the model; many sections will refer back to Chapter 3 while others may take a new approach toward some of the problems. Much of the model is similar to the models build/used by Introne (2004) and Block (2005). Some of the additions to their work include the segmented aperture geometry, a novel way of modeling telescope jitter, flimsy-lightweight mirror aberration modeling using foward Brownian Motion, and flimsy-lightweight mirror aberration modeling using an interferogram of a flimsy mirror.

The later sections in this chapter will describe image quality metrics and different tests that will be used to rank imaging systems based on their performance. By the end of this chapter the reader will have a good understanding of how the model functions and the tests that will be used to rank imaging systems.

4.1 Model Overview

At this point it is appropriate to have a general understanding of the model. This section will be referred to multiple times over the coming chapter. Figure 4.1 is a flow chart showing the model in its basic form. It begins by resizing the synthetic radiance cube to match the

GSD of a system with a given altitude, pixel pitch, and focal length. At each spectral band the image plane is Fourier transformed and multiplied by its respective band of the system OTF, this action is defined by Eq. 3.4. The output is then inverse Fourier transformed, multiplied by the transmission of the optics and quantum efficiency of the detector, and summed over the desired bandpass; in this example, the bandpasses are 400-490nm, 500-590nm, and 600-690nm. The video experiments will use both red, green, blue, and near-infrared bands (RGBN). The output which is still in units of radiance $\left[\frac{W}{m^2 sr}\right]$ is operated on by the detector model which converts the radiance to the detector output which is in units of electrons. Then various forms of noise that are described in Section 3.6 are added to the signal. The signal is then passed through an amplifier which converts it from electrons to volts. This signal is then restored using the Wiener-Helstrom Filter described in Section 3.7 and then finally quantized to a user specified bit number.

4.2 Systems Integration

At this point all pieces of the system are in place to fully integrate a "simple" single broad band imaging system from a geosynchronous orbit. To create a system MTF or system PSF the effects of the aperture, detector, and jitter must be combined. This can be done in the spatial domain by convolving the *psf*s:

$$psf_{system}(x, y, \lambda) = psf_{aper}(x, y, \lambda) * psf_{detector}(x, y) * psf_{jitter}(x, y) \tag{4.1}$$

or this can be done in the frequency domain by multiplying OTFs and MTFs:

$$OTF_{system}(\xi, \eta, \lambda) = OTF_{aper}(\xi, \eta, \lambda) \cdot MTF_{detector}(\xi, \eta) \cdot MTF_{jitter}(\xi, \eta). \tag{4.2}$$

It is important to note that the psf_{aper} and the OTF_{aper} are spectrally dependent. Each spectral wavelength's psf/OTF is operated on by the same detector and jitter functions because they are not spectrally dependent. Figure 4.2 shows a Cassegrain aperture with no aberations, a Gaussian jitter function with a σ_{Jitter} = .1pixels, the detector MTF, and the system MTF. The plot is along the ξ-axis of the reference band where the optical cutoff

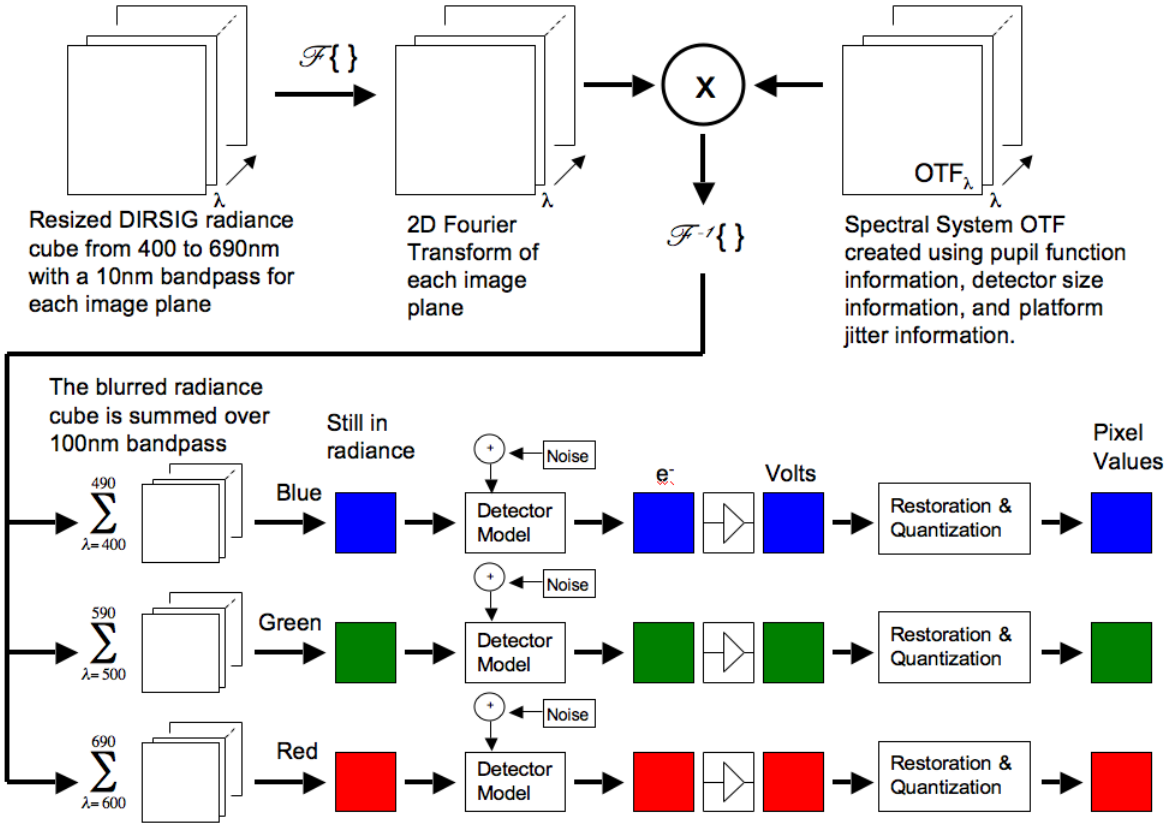

Figure 4.1: An overview of the model.

frequency equals the detector sampling frequency at .5 [cycles/pixel].

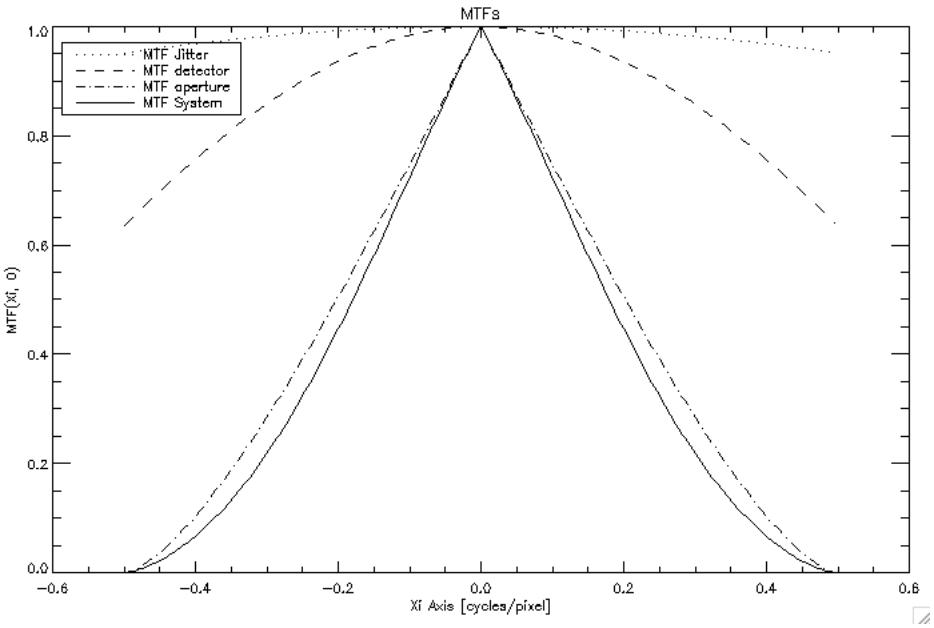

Figure 4.2: Components of the system MTF

All that is needed is data to apply to the OTF_{system} or PSF_{system}. The Digital Imaging Remote Sensing Group at the Rochester Institute of Technology has produced a synthetic image generation tool called DIRSIG (Digital Imaging and Remote Sensing Image Generation) [Schott (2007)], which can produce radiometrically accurate at aperture radiance values (L_{aper} from Section 3.2). Given that this instrument is located in a geosynchronous orbit (altitude of 35,786 Km) and has a focal length, f, it is possible to calculate the ground sample distance (GSD) by projecting the pixel size through the imaging system onto the ground using similar triangles as shown in Figure 4.3. In addition to the GSD, DIRSIG also needs the altitude and the viewing angle of the telescope. The DIRSIG data, which is in radiance units, can be applied to Eq. 3.15 which gives the signal in electrons. The additive noise calculated in Eq. 3.52 can be added to the signal in electrons. This value can then be multiplied by the electronic and conversion gains and then applied to the PSF_{System} or OTF_{System} as shown

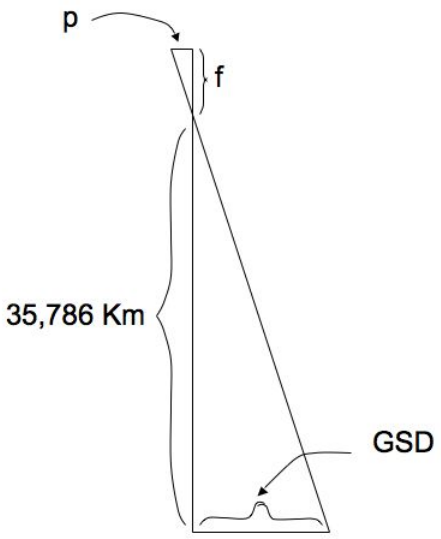

Figure 4.3: Similar triangles projection of the pixel onto the ground to calculate the GSD.

below:

$$I(x, y, \lambda) = psf_{System}(x, y, \lambda) * G_{conv} \cdot G_{elec} \cdot (S_{e^-}(x, y, \lambda) + n_{electrons}(x, y, \lambda)). \quad (4.3)$$

or in the frequency domain as:

$$I_{\mathcal{F}}(\xi, \eta, \lambda) = OTF_{System}(\xi, \eta, \lambda) \cdot G_{conv} \cdot G_{elec} \cdot (S_{\mathcal{F},e^-}(\xi, \eta, \lambda) + N_{electrons}(\xi, \eta, \lambda)). \quad (4.4)$$

Doing a convolution operation is computationally expensive, therefore the author recommends the far more efficient frequency domain implementation. Finally, a Wiener filter can be applied in the frequency domain to restore some of the image quality that was attenuated.

$$\begin{aligned} FinalImage(x, y, \lambda) &= \mathcal{F}^{-1}\{I_{(F)}(\xi, \eta, \lambda) \cdot W(\xi, \eta, \lambda)\} \\ &= \mathcal{F}^{-1}\{OTF_{System}(\xi, \eta, \lambda) \cdot G_{conv} \cdot G_{elec} \cdot (S_{e^-,\mathcal{F}}(\xi, \eta, \lambda) + \\ &N_{electrons}(\xi, \eta, \lambda)) \cdot W(\xi, \eta, \lambda)\} \end{aligned} \quad (4.5)$$

The flow chart in Figure 4.4 shows the entire model and all the parameters that can be adjusted. Take note of the complexity here and how understanding the importance of each parameter would require a large amount of experimentation. Understanding all of these parameters is beyond the scope of this thesis and we have to limit ourselves to GSD; piston, tip, and tilt aberrations; lightweight optic aberrations; spectral band choice; and SNR.

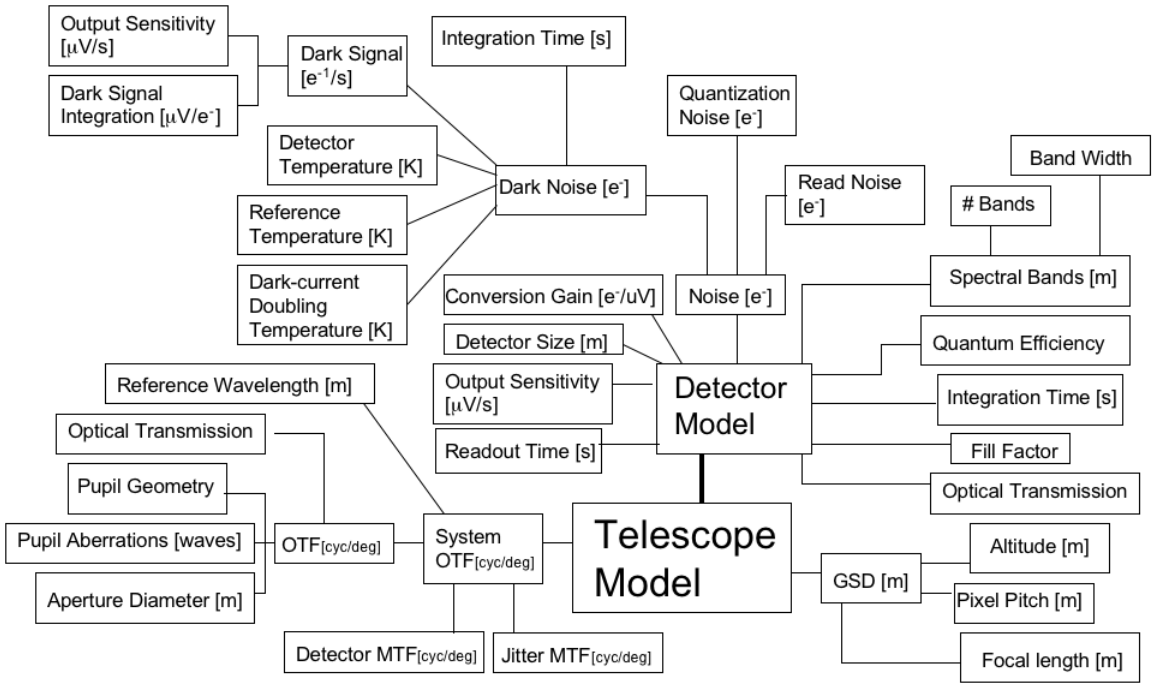

Figure 4.4: Flow chart of the all the parameters accounted for in the space telescope model. This gives some idea of the inner workings of the space telescope model; however, for a more indepth look at which terms are additive and multiplicative refer to Chapter 3.

4.3 Scene and Signal Modeling

DIRSIG allows easy generation of radiometrically accurate synthetic scenes from CAD models. An atmosphere can be generated using the U.S. Air Force atmospheric modeling software MODTRAN [Schott (2007)]. The atmospheric transmission is applied within DIRSIG

to produce an at aperture spectral radiance cube. Different data sets in this experiment have different bandpasses. The "tile1" data set (see Figure 4.5) used to make RGB images is centered over Irondequoit, NY. This data set has 30 bands each with a bandpass of 10nm ranging from 400-690nm. The tile 4 data set is used to make RGB (see Figure 4.6) and NIR images for spatial target detection experiment. It has 51 bands each with a bandpass of 10nm ranging from 400-900nm. The video data from tile 4 has only three bands each of a 100nm band pass ranging from 400-700nm and a fourth NIR band with a 200nm bandpass ranging from 700-900nm (see Figure 4.26). The radiance files are then interpolated to the proper pixel pitch (see Section 4.2) before any processing is done. One attractive feature of the tile1 imagery is that there are three images with a GSD of 1m, 2m, and 3m, it is therefore possible to produce imagery with a wide range of sensor altitudes, pixel pitches, aperture diameters, and focal lengths.

Figure 4.5: Unprocessed RGB image of Tile 1.

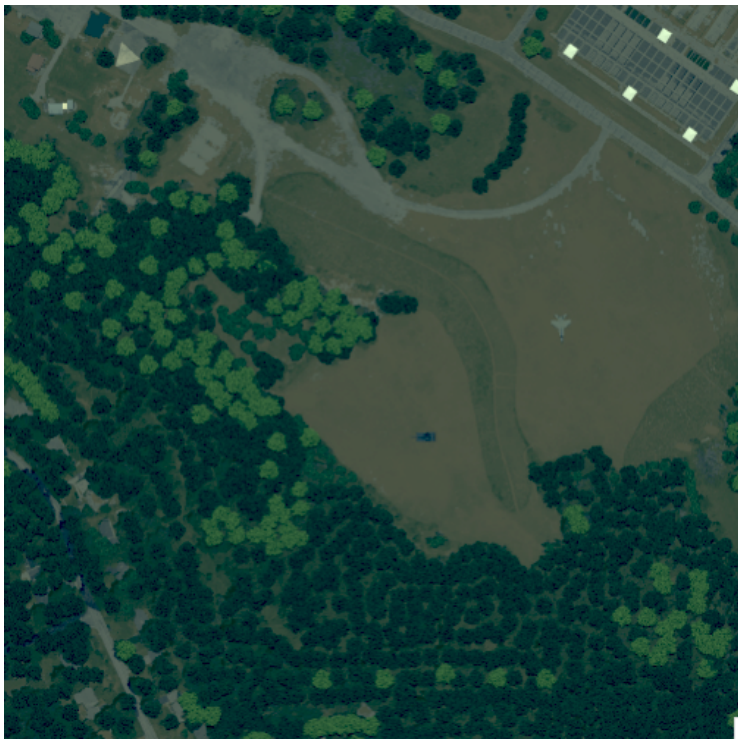

Figure 4.6: Unprocessed RGB image of Tile 4.

4.4 Detector Modeling

The space telescope imaging simulation tool was made so that it would be flexible when modeling different detectors. This means that detector attributes such as pixel pitch, temperature, dark current doubling temperature, output sensitivity, read noise, and quantum efficiency, are inputs to the model. Figure 4.7 shows parameters for various Kodak detectors that have been modeled. These parameters came from Kodak Specification sheets and are cited in the bibliography [KAF (2006), KAF (2007a), KAF (2007b), KAF (2007c), KAF (2004), KAF (2005)]. By modeling these detectors we are ensuring that the system attributes are being

Detector	Size [pixels]	Pixel Pitch [µm]	Dark Current Doubling Temperature [ΔK]	Dark Signal Integration [mV/s]	Dark Signal [e^-/s]	σ_{read} [e^-]	Output Sensitivity [µV/e^-]	$T_{readout}$ [ms]	Quantum Efficiency [R, G, B]
KAF-39000	7216 x 5412	6.8	6.3	4	-	16	26	1077	[.23,.28,.20]
KAF-16803	4096 x 4096	9	6.3	-	3	9	22	4450	[.47,.62,.47]
KAF-10500	3970 x 2646	6.8	6.3	5	-	15	25	268.4	[.32,.40,.21]
KAF-09000	3056 x 3056	12	7	-	5	7	24	2533	[.50,.64,.50]
KAF-4320E	2084 x 2084	24	6.4	-	250	20	10	470.3	[.40,.65,.63]
KAF-4301E	2084 x 2084	24	6	-	150	20	11.5	5320	[.40,.70,.60]
KAI-10100	3648 x 2760	4.7	7.5	-	See specs.	See specs.	32	93	[.32,.42,.40]
KAI-01050	1024 x 1024	5.5	7		7	12	34		[.31,.42,.43]

Figure 4.7: Parameters of the modeled detectors.

modeled realistically. The flow chart shown in Figure 4.4 gives some semblance of how these detector parameters are used. For a more in-depth view of each one of the blocks in Figure 4.4 turn to Chapter 3 of this thesis.

4.5 Aperture Modeling

This section will demonstrate how the segmented aperture pupil function was built. The process for making an individual segment can be broken into two sections: one for the piston, tip, and tilt (PTT) aberrations and another for the lightweight flimsy style aberrations. The PTT WFE map is created by first making a plane with random amount of tip, tilt, and piston bias. This is done by making a plane that has a slope of 1 in the x and y directions and a bias of 0. This would be a plane defined as:

$$z = x + y \tag{4.6}$$

If a Gaussian random number generator - that has a population mean of 0 and a population standard deviation of 1 - is used, three random coefficients can be obtained to modify the slope and bias of the plane. At this point our plane has a RMS error of 1.

$$z = R_1 x + R_2 y + R_3 \tag{4.7}$$

The RMS error can be controlled by multiplying the random coefficients by a standard deviation (σ_{PTT}). The RMS error is now σ_{PTT}:

$$z = \sigma_{PTT}(R_1 x + R_2 y + R_3) \tag{4.8}$$

Finally, the plane can be multiplied by the segment mask shown in Eq. 4.9 (observe Figure 4.8 to see the planes and segments).

$$PTT\ Segment\ WFE = SegmentMask\big(\sigma_{PTT}(R_1 x + R_2 y + R_3)\big) \tag{4.9}$$

Making the WFE map for the flimsy aberrations is somewhat similar. In this case an interferogram of a lightweight segmented mirror is used to create the initial aberration form (see Figure 4.9). The values of the initial surface are manipulated by dividing the surface by its RMS WFE error value and then subtracting the surface's mean value. This provides us with a flimsy segmented mirror that has a standard deviation of 1 and a mean of 0, we refer to it as $Segment$ in Eq. 4.10. This surface can then be multiplied by a random number (R_4)

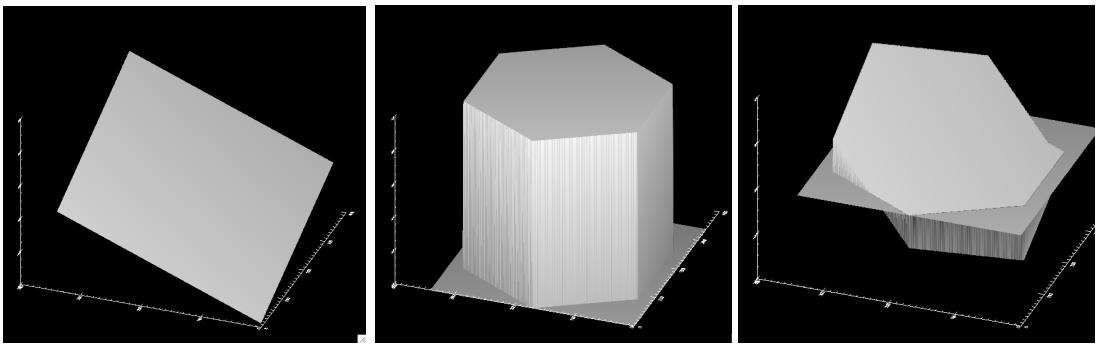

(a) 3-dimensional plane (b) Mask of a single segment. (c) A single segment with RMS PTT WFE (σ_{PTT}).

Figure 4.8: The plane in Figure 4.8(a) is multiplied by the mask of a hexagonal segment shown in Figure 4.8(b) to produce a segment with PTT WFE shown in Figure 4.8(c).

to assign a random amount of flimsy WFE with a zero mean and standard deviation of 1. RMS flimsy WFE is introduced by multiplying the array by σ_{flimsy}. The surface can then be rotated some random interval of 60° by the operator $Rotate$ where R_5 is the random number assigning the rotation:

$$Flimsy\ Segment\ WFE = Rotate(R_5)\{\sigma_{flimsy}\ R_4\ Segment\} \tag{4.10}$$

Finally, the flimsy segment is then added to the PTT segment:

$$Segment\ WFE = Flimsy\ Segment\ WFE + PTT\ Segment\ WFE \tag{4.11}$$

This process can be repeated to produce 18 hexagonal segments that can be placed in an array to construct a pupil function (see Figure 4.10). Using this technique the RMS WFE error caused by piston, tip, tilt, and flimsy aberrations can be controlled using σ_{PTT} and σ_{flimsy}.

The reader may have noticed in Section 3.7 that if a Wiener-Helstrom filter is used then there must be some knowledge of a system transfer function. A major component of the

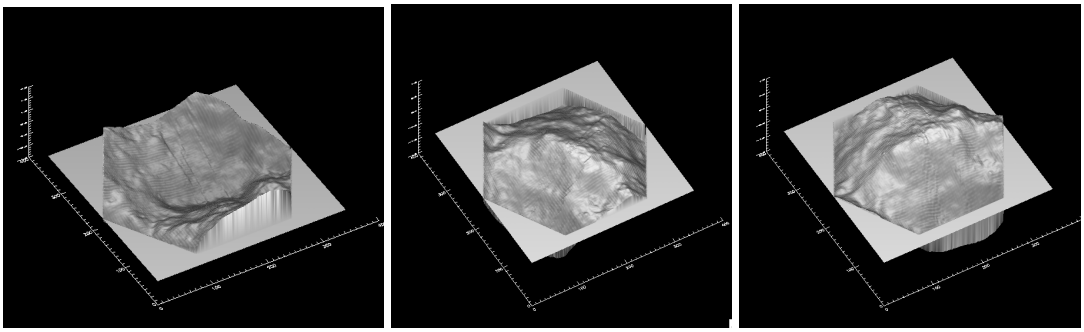

(a) Original flimsy mirror interferogram.

(b) Scaled and rotated version of the original interferogram. Notice that a negative scaling value was applied.

(c) The sum of the PTT segment and the flimsy mirror segment.

Figure 4.9: The interferogram in Figure 4.9(a) is randomly scaled and rotated some random interval of 60° (shown in Figure 4.9(b)). The flimsy mirror WFE is then added to the PTT WFE to get a segment that contains both PTT and flimsy mirror aberrations (shown in Figure 4.9(c)).

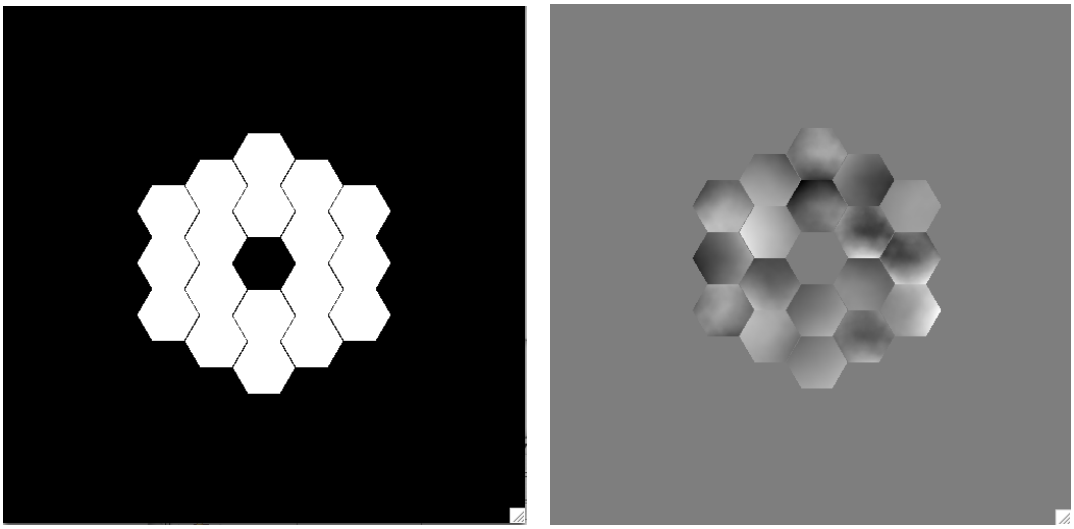

(a) Magnitude

(b) WFE

Figure 4.10: This Figure shows the magnitude and WFE of a pupil function that has .1 RMS PTT WFE and .1 RMS Flimsy WFE.

system transfer function comes from the pupil function. If there is no WFE knowledge of the segments then the magnitude of the pupil function can be used in the transfer function calculation. However, if WFE knowledge is going to be incorporated into the transfer function then the optimal situation would be to have full knowledge of the pupil's WFE. This is usually never the case. In this effort we will incorporate WFE knowledge into the system transfer function used in the restoration filter. We do this by introducing some random error to the original pupil function we used in the modeling process. This is simply done by creating another pupil function using the same techniques as before only this time it will have a $\sigma_{PPT,WFE\ knowledge}$ and $\sigma_{flimsy,WFE\ knowledge}$ (shown in Eq. 4.12 and Eq. 4.13). It is important to note that the random number (R_5) that determined how much the flimsy mirror would be rotated is used again in this calculation.

$$\begin{aligned} PTT\ Segment\ WFE\ knowledge &= SegmentMagnitude\big(\sigma_{PTT,WFE\ knowledge} \\ &\quad (R_6 x + R_7 y + R_8)\big) \end{aligned} \tag{4.12}$$

$$Flimsy\ Segment\ WFE\ knowledge = Rotate(R_5)\{\sigma_{flimsy,WFE\ knowledge}\ R_9\ Segment\} \tag{4.13}$$

The pupil function knowledge is then computed by adding the PPT knowledge and flimsy knowledge to the system pupil function.

$$\begin{aligned} Segment\ WFE\ knowledge &= Segment\ WFE \\ &\quad + PTT\ Segment\ WFE\ knowledge \\ &\quad + Flimsy\ Segment\ WFE\ knowledge \end{aligned} \tag{4.14}$$

In the initial stages of this work there was a comparison between having a WFE knowledge to within $.05$ and $.1$ RMS [waves] with a reference wavelength of 550nm. The results showed very little (if any) improvement was made by increasing WFE knowledge from $.1$ to

.05. This is discussed in more detail in Section 4.7. All experiments that utilized the Wiener-Helstrom Filter use pupil functions that have phase knowledge to within .05 PTT and Flimsy WFE.

4.6 MTF Modeling

This section describes the various types of transfer functions modeled and how they were adapted to this problem. The first section is perhaps the most important as it is about the modeling the OTF. The next section presents a novel technique for modeling a jitter MTF. And finally the last two sections briefly describe the detector MTF modeling and system OTF modeling, and provide references to other areas of this document that contain more information.

4.6.1 OTF Modeling

Once the complex pupil function is generated, it is Fourier transformed, applied to Eq. 3.24, then inverse transformed, and normalized so that the magnitude of the OTF equals 1. The spectral effects discussed in Section 3.11 are introduced by first creating a new pupil function that has a phase scaled using Eq. 3.79. Also, as mentioned in Section 3.11 the range of spatial frequencies that reach the detector is spectrally dependent. A system that is designed for green light will observe higher spatial frequencies for blue light and lower spatial frequencies for red light. That means that the blue light is aliased by the detector and the red light is always undersampled. This model has been **chosen** to be centered at the green band; Fienup (1999) describes how the pupil function can be scaled using the equation below:

$$M_l = M_0 \frac{\lambda_0}{\lambda_l} \tag{4.15}$$

where M_0 is the array size of the pupil function at the reference wavelength (λ_0). It should be noted for the following discussion that M_0 is also the size of the image. Figure 4.11 will aid in the description of how the pupil is treated for different wavelengths.

Each one of these pupils was scaled from the original reference wavelength (λ_{550nm}). The

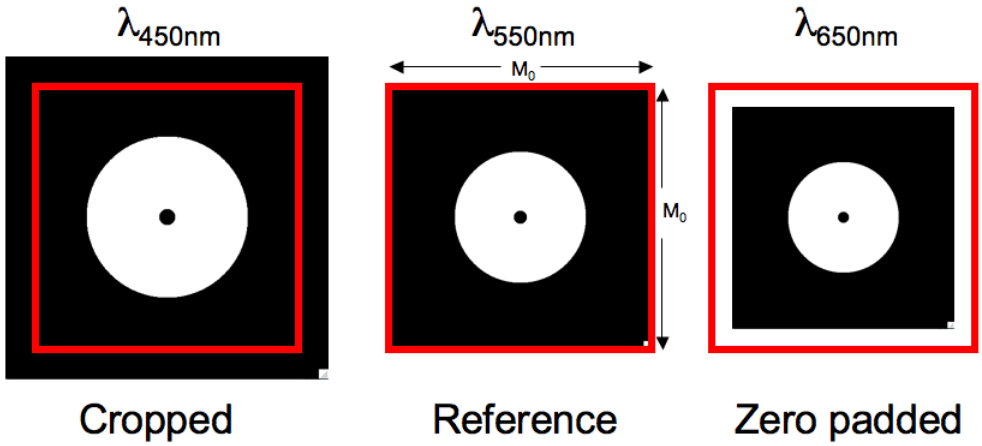

Figure 4.11: Each figure is for a different spectral band. The OTF from the wavelength $< \lambda_0$ is cropped and the OTF from the wavelength $> \lambda_0$ is zero padded.

important thing to remember is that the scale on the OTF of the pupil function ($\Delta\frac{cyles}{pixel}$) does not change. Again, this means that the focal plane will observe higher spatial frequencies for the blue and lower spatial frequencies for the red. This causes aliasing for the blue and undersampling for the red. Aliasing is done here when the MTF is created; the aliased spatial frequencies are wrapped around by the autocorrelation and in turn weight the appropriate lower spatial frequencies. The red pupil function was zero padded so that it had an array size of M_0, this means that the red channel will never be sampled at the Nyquist frequency (always undersampled). This is seen in Figure 4.12. Notice how the highest spatial frequencies close to the ξ and η axis of the blue band OTF are amplified slightly by the aliasing, the green band OTF stops right at the highest spatial frequency (Nyquist), and the red band will always be undersampled.

4.6.2 Jitter MTF Modeling

Jitter was described in Section 3.10 as Gaussian and isotropic over T_{int}. This idea is a rather poor assumption for a space telescope such as the one being modeled. The reason for this is that the integration time is more than likely going to be fast ($< 1/1000$[sec]). Under certain circumstances the telescope might be made out of lightweight optics which are rather flimsy.

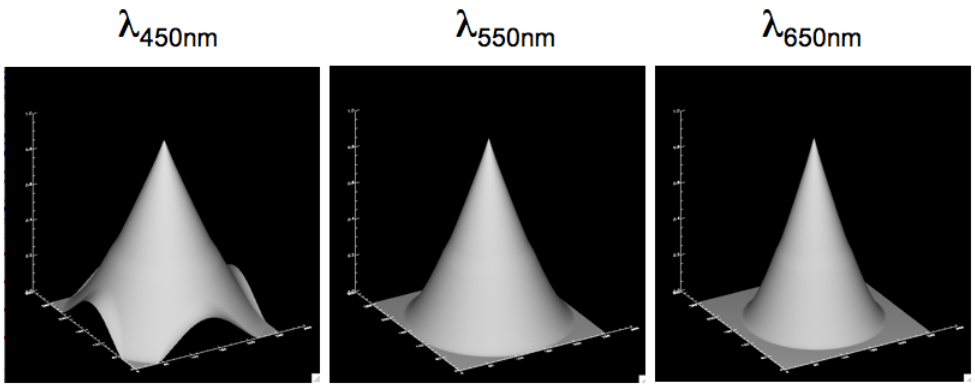

Figure 4.12: Each figure is a different OTF at the wavelength shown above the diagram.

A flimsy mirror will vibrate at a much lower frequency than a rigid mirror. If the vibrations are low enough and the integration time is short enough the jitter can no longer be assumed to be isotropic over the integration time. This means that over T_{int} the image motion might look more like a smear.

The JWST has a fine steering mirror that compensates for large line of sight jitter. One might imagine that there are different amounts (or amplitudes) of jitter at different frequencies. From this reasoning one might then imagine that the telescope has a jitter spectrum. Structural models of the JWST have shown that the jitter spectrum is closely related to the telescope's actuating system (Mather (2004)).

In this modeling example there are currently no available jitter spectra; therefore, a reasonable jitter spectrum has been developed where low frequency movements have large amplitudes and high frequency movements have low amplitudes. This could be done in the frequency domain by defining the amplitude as $1/\sqrt{f}$ and defining a random Gaussian phase. It would be convenient if the user could define the mean and standard deviation of the jitter function. This is done by first setting the mean to zero through usage of the Central Ordinate Theorem, which states that the magnitude of the central ordinate defines the mean value of

the transformed data. Therefore, the central ordinate (f=0) is set to 0.

$$|\mathcal{JITTER}(f)| = \frac{1}{\sqrt{f}} \; with \; |\mathcal{JITTER}(f=0)| = 0 \tag{4.16}$$

$$\Phi\{\mathcal{JITTER}(f)\} = Random(0,1) \tag{4.17}$$

$Random(0,1)$ is a random array with a zero mean and standard deviation of 1. This function can be Fourier transformed into the spatial domain and separated into real and imaginary parts to define the x and y-axis respectively.

$$Jitter(x) = Real\{\mathcal{F}\{\mathcal{JITTER}(f)\}\} \tag{4.18}$$

$$Jitter(y) = Imaginary\{\mathcal{F}\{\mathcal{JITTER}(f)\}\} \tag{4.19}$$

The standard deviation of the jitter for each axis is then calculated and that value is divided from the jitter function for each respective axis. This simply scales the amplitude of the jitter function so that its standard deviation is unity. By multiplying the jitter function by the desired standard deviation the end function has zero mean and a user defined STD.

$$Jitter_{\sigma_x}(x) = \sigma_x \frac{Jitter(x)}{std(Jitter(x))} \tag{4.20}$$

$$Jitter_{\sigma_y}(y) = \sigma_y \frac{Jitter(y)}{std(Jitter(y))} \tag{4.21}$$

Figure 4.13 shows the $1/\sqrt{f}$, random phase, x-coordinates, and y-coordinates centered at 255 for a 512x512 array.

When the x-coordinates and y-coordinates are combined they present a plausible line of sight jitter. This is shown in Figure 4.14.

The jitter function can be converted into a PSF and subsequently into an MTF. This can be done by creating a “floating pixel” that is centered above the line of sight projection onto the CCD at any point during the integration time. If the LOS is projected perfectly on the center of a pixel, 100% of the floating pixel will sit above that projected pixel (refer to Figure 4.15). If the LOS is not perfectly projected onto the center of a pixel, different percentages of the floating pixel will fall on neighboring pixels (refer to Figure 4.16). These different

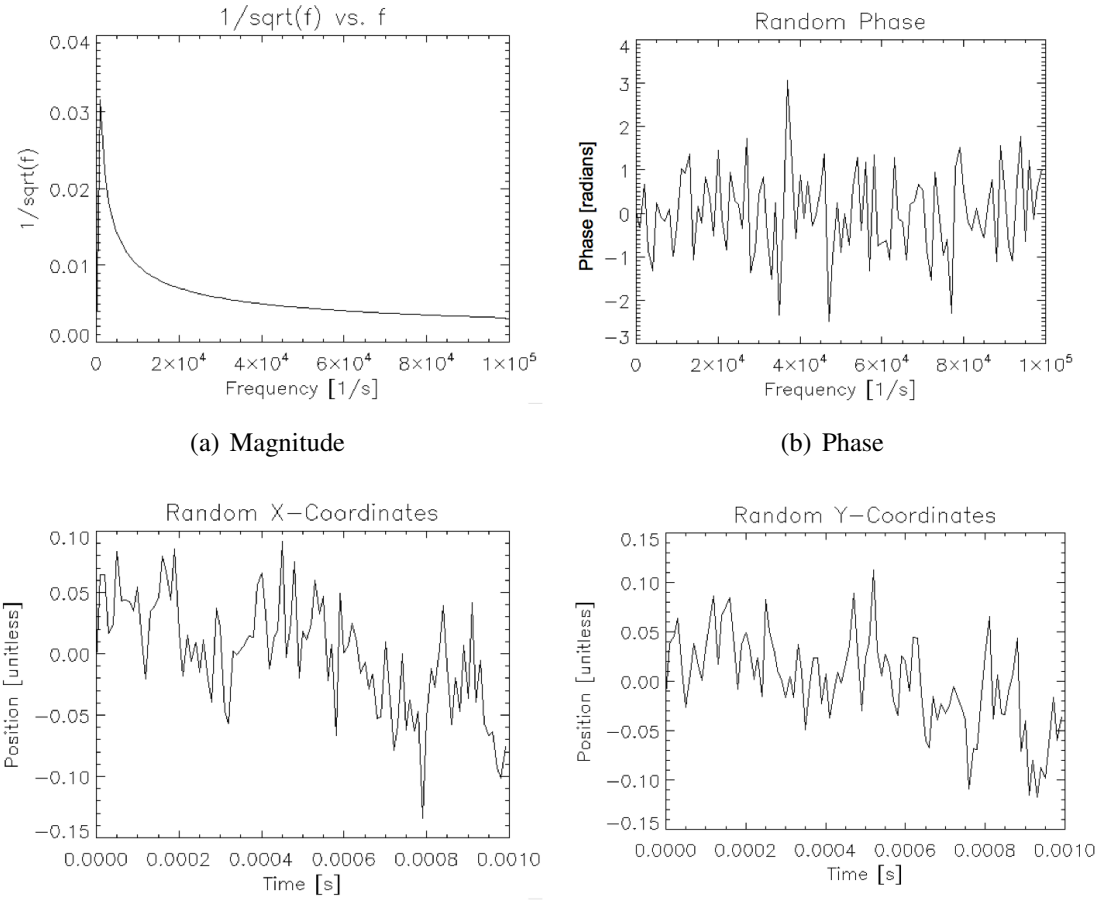

(a) Magnitude

(b) Phase

(c) x-axis

(d) y-axis

Figure 4.13: The top plots show the magnitude and phase. The bottom plots show the x and y coordinates for the jitter over 1/1000 of a second.

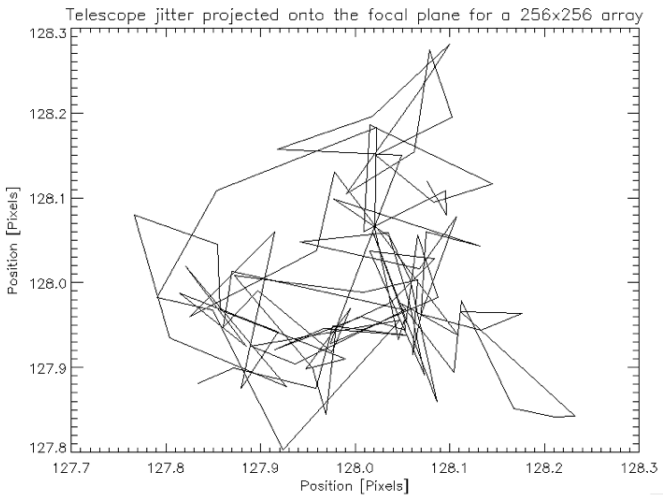

Figure 4.14: Plausible jitter over 1/1000 of a second.

percentages can be used to form a PSF for that one moment in time because it shows where a point on the ground would spread its energy if there were perfect optics. If for each movement the percentages are calculated, saved, and then finally summed to create a cumulative PSF over T_{int} (refer to Figure 4.17). This cumulative PSF can then be Fourier transformed and normalized to produce a MTF_{Jitter} (refer to Figure 4.18).

It is worth mentioning that the example presented above produced an MTF that looks quite Gaussian, which is just what the traditional modeling approach would have produced. The importance here is that this is a result of the prescribed jitter spectrum; another jitter spectrum might produce an MTF that looks nothing like a Gaussian. Using this technique in another potential situation where the integration time is on the order of a "jitter oscillation" we would find this technique produced a smear. Or with a few simple modifications this technique could also be used on systems where the x and y jitter spectra are significantly different.

This technique could be improved by using the system PSF instead of a floating pixel. The impulse response of the system is not going to be a square, and therefore this technique is mildly inaccurate.

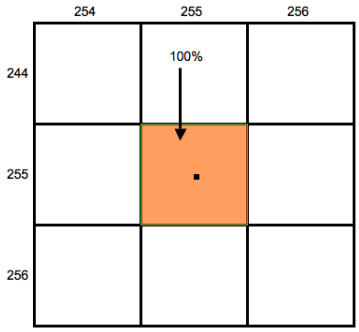

Figure 4.15: The LOS is projected perfectly onto the center of a pixel. The orange region is the floating pixel.

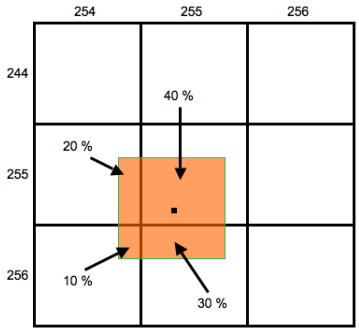

Figure 4.16: The LOS is *not* projected onto the center of a pixel. Here there are different percentages of the floating pixel spread over four pixels.

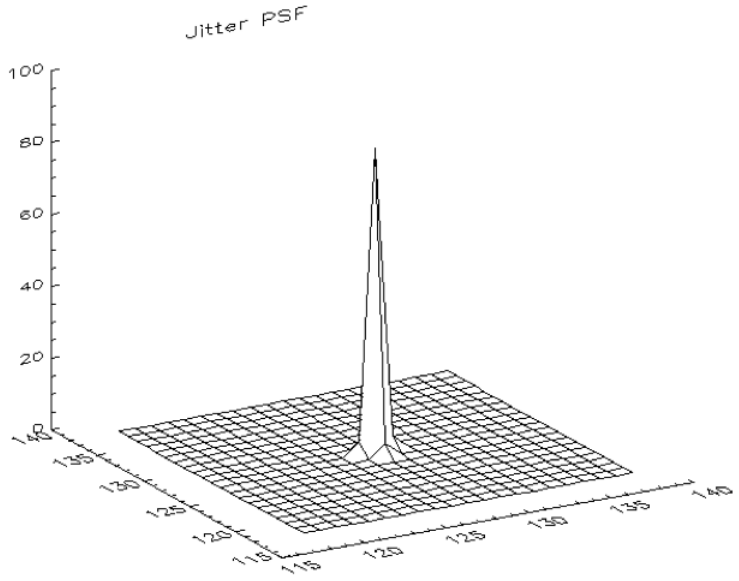

Figure 4.17: The cumulative PSF.

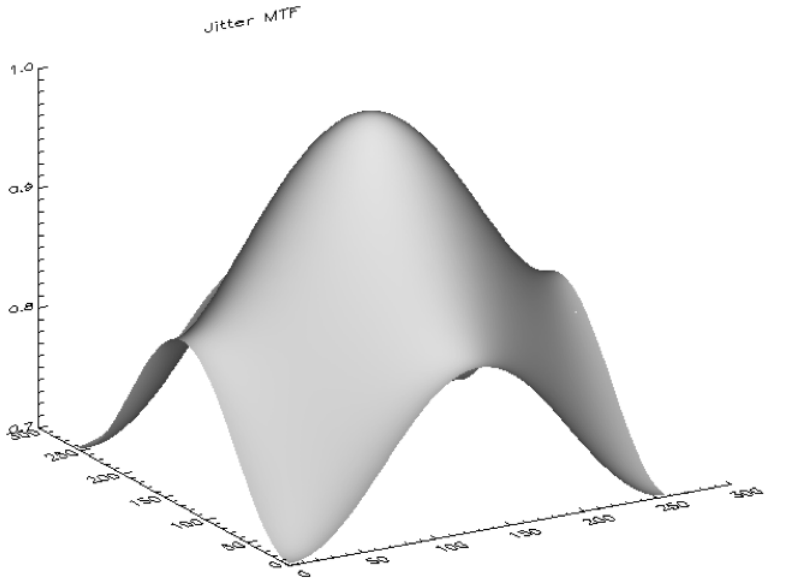

Figure 4.18: The MTF_{Jitter}.

4.6.3 Detector MTF Modeling

The detector MTF is modeled as was described in Section 3.4.

4.6.4 The System OTF

The system OTF is created by first replicating the detector and jitter MTFs so that there is one for each spectral band and then multiplying the detector MTF, jitter MTF, and the spectral OTF together to form a system OTF for each spectral band. This is shown below in Figure 4.19.

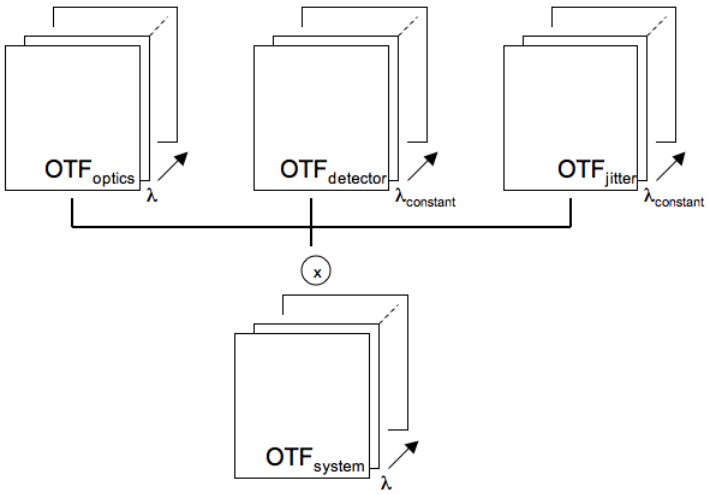

Figure 4.19: The system OTF.

4.7 Image Restoration via Wiener Filter

The final stage before image output is to apply the Wiener-Helstrom Restoration Filter described in Section 3.7. It may be necessary to adjust the noise-to-signal power ratio in Eq. 3.72 to improve the final image sharpness. If phase knowledge of the mirrors is available it can be used in the calculation of the transfer function. If it is not available the unaberratted pupil function should be used. Initial motion detection experiments showed us that changing

the pupil function phase knowledge from .05 RMS WFE to .1 RMS WFE did not produce any noticeable improvement in the % of motion detected.

The restoration filter does have positive effects on the motion detection experiments. Determining the noise-to-signal power ratio was done by first stepping the noise-to-signal power ratio incrementally from 0 to 2 in increments of .5 and selecting the minimum value. Then the process was repeated from .1 to .4 in increments of .1. And finally from .27 to .33 in increments of .01. All experiments were done with moderate aberrations (RMS PTT WFE of .15 [waves] and RMS flimsy WFE of .3 [waves]), good pupil phase knowledge (RMS PTT WFE knowledge of .5 [waves] and RMS flimsy WFE knowledge of .5 [waves]), and a moderate SNR of 50. The best motion detection was achieved by a noise-to-signal power ratio of .3.

4.8 Image Quality

The main objective of this project is to compare and contrast a variety of different imaging scenarios. Perhaps the most accurate method would be to ask an analyst to view images from different systems and then rank them in terms of image quality. Unfortunately, these resources are not available and a more automated approach is necessary. Traditionally systems designers have relied on the Generalized Image Quality Equation (GIQE) to provide them with an estimate of image quality. This document will utilize the GIQE for some of the tests carried out. Other MTF based techniques are proposed as well. The objective here is to show that the GIQE does not work well with poorly behaved MTFs. This will hopefully provide an understanding of why an image utility approach (see section 4.9) is a better technique for assessing system performance.

4.8.1 The Generalized Image Quality Equation (GIQE)

The traditional approach to determining image quality associated with reconnaissance systems is the *National Imagery Interpretability Scale* (NIIRS) [Schott (2007)]. The scale relates the analyst's ability to perform exploitation tasks and ranges from 0 to 9, where 0 means the

imagery is uninterpretable and 9 means that small objects such as spikes on railroad ties are viewable. The scale is designed so that fractional values of .2 are usually perceptible.

Since the introduction of the NIIRS there has been a drive to relate system design parameters to the NIIRS value. Leachtenauer et al. (1997) developed the *General Image Quality Equation* (GIQE) to relate system design parameters or measurable quantities within the image to the subjective NIIRS system. The GIQE is written as:

$$NIIRS = 10.251 - aLog_{10}GSD_{GM} + bLog_{10}RER_{GM} - 0.656H_{GM} - 3.44G/SNR \quad (4.22)$$

where GSD_{GM} is the geometric mean of the GSD in inches, RER_{GM} is the geometric mean of the normalized relative edge response (RER), H_{GM} is the geometric mean height overshoot caused by the edge sharpening, G is the gain due to the edge sharpening, SNR is the signal to noise ratio, a = 3.32 if RER $\geq$ 0.9 and 3.16 if RER $<$ 0.9, and b = 1.559 if RER $\geq$ 0.9 and 2.817 if RER $<$ 0.9. Descriptions of how to obtain these values is well documented in Leachtenauer et al. (1997) and Schott (2007).

There is a problem with this method. If the reader looks back to Section 3.8, all of the noncicularly symmetric apertures have non-circular MTFs, this means that the RER will change depending on the direction of the edge and thereby produce inaccurate ΔNIIRS values. This was demonstrated in Fiete et al. (2002) where there were large errors in ΔNIIRS values for the triarm and Golay 6 aperture types. Fiete calls for an additional study to formulate a new image quality equation that better suites sparse apertures.

A portion of Fiete et al. (2002)'s work will be repeated, however this time aberrated segmented apertures will be tested in place of sparse systems. With the introduction of aberrations the problem becomes somewhat more complicated because of global tip and tilt errors. Tip and tilt errors cause the center of the edge spread function to shift making it impossible to consistently determine the RER and the mean height overshoot. In order to get around this problem a different approach must be taken; the RER is the slope of the normalized edge spread function. Traditionally the RER is determined by blurring an oversampled edge with the system MTF and then computing the slope between the center pixel and 1.25 pixels to either side of the center. In this case because the center pixel moves due to global tip tilt errors a different technique is employed in determining the RER. The normalized edge response can

be found by numerically integrating the psf (see Figure 4.20(a) and Figure 4.20(b)) along the x and y axis and then dividing by the total area under the psf slice. The RER is determined by taking the numerical derivative (see Figure 4.20(c)) of the normalized edge spread function and then finding the maximum value.

The height edge overshoot (H) is computed by applying the Wiener Filter to the edge (see Figure 4.20(d)) and taking the maximum value of the sharpened edge.

The next term that had to be determined was the noise gain which is computed from the 3x3 MTFC restoration kernel. Unfortunately, the kernel could not be determined. The approach for determining the kernel was to Fourier Transform the Wiener Filter and then crop out a 3x3 kernel around the central ordinate. This technique proved to be unsuccessful and unrealistic noise gain terms were obtained. Therefore all GIQE results given in this research effort are for high SNR scenarios where noise is not an issue (where it would create less than .2 ΔNIIRS).

If we take the values from the plots in Figure 4.20 and plug them into Eq. 4.23 then we get the answer displayed below. The author believes that this is about right for the imagery created from such a system [see Figure 4.21].

$$NIIRS = 10.251 - 3.16 * Log_{10} * 39.4 + 2.817 * Log_{10} * 1.5 = 2.75 \tag{4.23}$$

4.8.2 Other Approaches for Assessing Image Quality

There are several other ways of assessing image quality using image based parameters. The *Image Quality Model* (IQM) judges image information content from the power spectrum of the image Leachtenauer and Driggers (2001). Another approach that might prove useful is using an idea derived from an analogue optical power spectrum classifier called a digital ring-wedge detector [Leachtenauer and Driggers (2001)]. The ring-wedge is composed of wedge shaped detectors on half a circle and ring shaped detectors on the other half of the circle, it is used together with neural network software on the FFT of the image. This technique has proven to be successful in sorting JPEG and gaussian blurred images with an accuracy of a

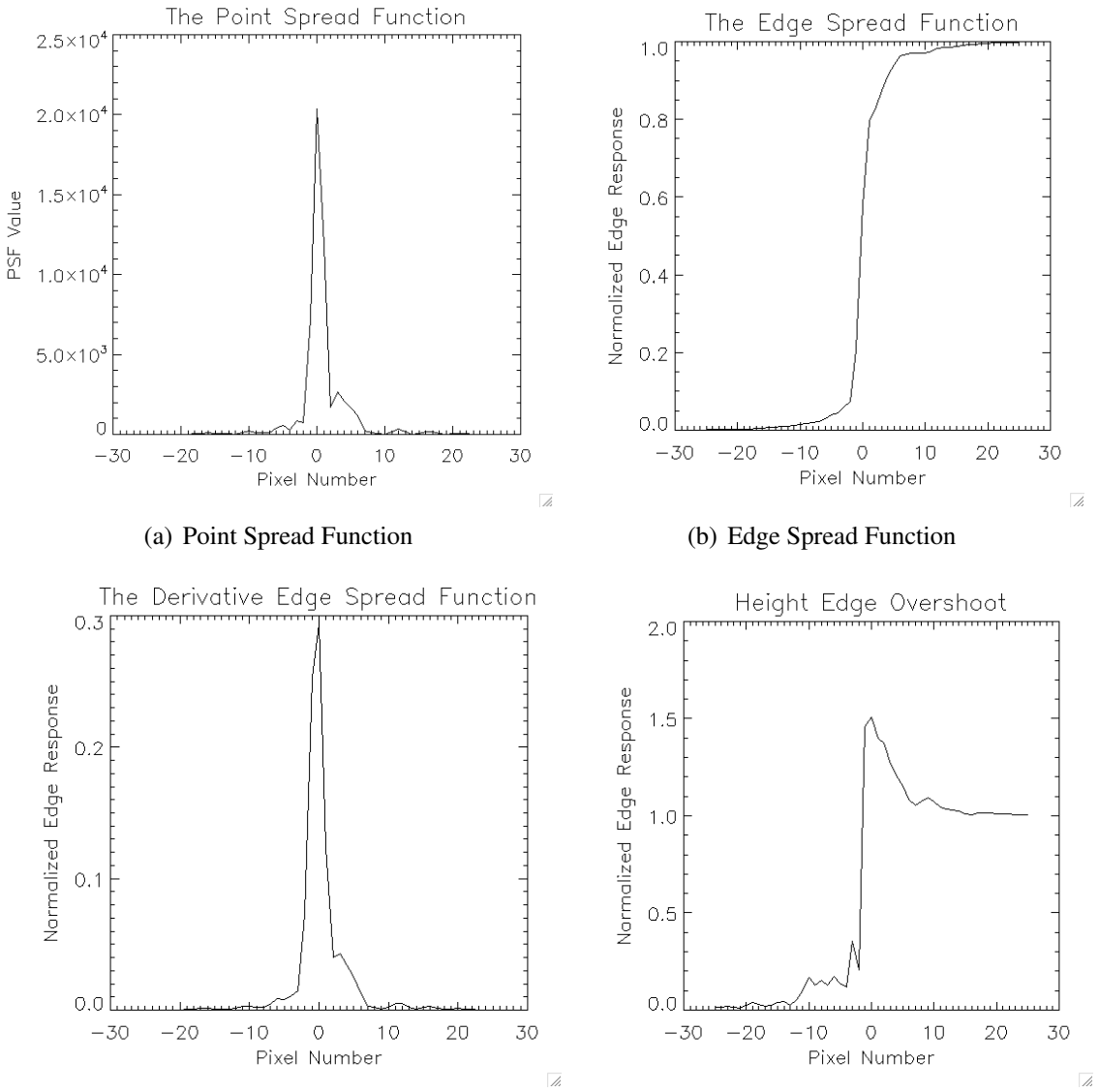

(a) Point Spread Function

(b) Edge Spread Function

(c) Edge Slope

(d) Height Edge Overshoot

Figure 4.20: This figure contains several plots important to understanding the GIQE.

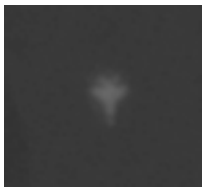

Figure 4.21: This is a simulated blue band image of a swept wing aircraft created by the imaging system that was analyzed by GIQE in Eq. 4.23.

95%. This might prove successful because of the shape of the FFT of the image will certainly have some of the attributes that the non-circularly symmetric MTFs possessed.

A novel parameter based approach might involve the digital ring edge detector (or some variant) used to assert the image quality from the system MTF. By using the pixel pitch and the focal length of the system it is possible to convert the MTF of the system into ground based units of cycles/meter (observe Eq. 4.24). In words, the MTF would be scaled by the pixel pitch, focal length, and sensor altitude. The area under the MTF would then have some indication of the image quality of the system.

$$MTF\left(\rho_{ground}\left[\frac{cycles}{m}\right]\right) = MTF\left(\rho_{focalplane}\left[\frac{cycles}{pixel}\right] * \frac{focallength[m]}{pixelpitch\left[\frac{m}{pixel}\right]} * \frac{1}{Altitude[m]}\right) \tag{4.24}$$

Where ρ is the spatial frequency value in units of $\left[\frac{cycles}{pixel}\right]$ on the focal plane and units of $\left[\frac{cycles}{m}\right]$ on the ground. This can be used as an image quality metric if it is weighted by ρ_{ground} and integrated under.

$$Image\ Quality = \int_0^{\rho_{max}} \rho_{ground} * MTF(\rho_{ground}) d\rho_{ground} \tag{4.25}$$

This technique is based upon the MTF and therefore does not include the effects of noise. This is a potential technique for quantifying image quality, but was not evaluated in this effort.

4.9 Alternative Techniques for Judging System Perfomance via Image Utility

In Section 4.8.1, it was referenced that Fiete et al. (2002) demonstrated that GIQE is an unreliable technique for estimating system performance for sparse aperture telescopes. Another method of characterizing image quality that uses the MTF was also proposed. In this section we take another look at how to solve the problem, not from an image quality stand point but more an image utility stand point. This is done using spatial target detection and video detection to judge an imaging scenario's ability to carry out specific tasks. For example, the first experiment will examine how mirror aberration causes the detectability of an object to decrease using only spatial characteristics, and the second experiment will use motion and some spectral information to find the point at which motion can no longer be detected.

4.9.1 Spatial Target Detection

Using spatial target detection algorithms, such as a matched filter along with a peak-to-sidelobe ratio (PSR) post processing step, users can find small objects ($<$ 150 pixels) in cluttered noisy scenes [Easton (2005)]. Assuming one has an idea of the shape of a target one could create a type of image quality metric that would be based on a system's ability to recognize shapes.

4.9.1.1 Matched Filter

The matched filter is used to detect known signals in clutter [Easton (2005)]. A measured signal $g(x)$ is made up of a known signal $f(x)$ positioned at some unknown coordinate x_0 with noise n(x) (see Eq. 4.26).

$$g(x) = f(x - x_0) + n(x) \tag{4.26}$$

The desired result is to construct a filter $m(x)$ that when applied to $g(x)$ will reveal the location of x_0. The impulse response, $m(x)$, will be a function of the known signal, $f(x)$,

and is commonly referred to as the "matched filter". This is shown below in Eq. 4.27.

$$g(x) * m(x) = f(x - x_0) * m(x) + n(x) * m(x) \tag{4.27}$$

The result of this convolution will be used to identify the location of x_0 by taking the maximum of the correlation plane.

$$x_0 = max(g(x) * m(x)) \tag{4.28}$$

It is possible to derive an ideal matched filter by thinking of two criteria that an ideal matched filter would have. The first is that when the matched filter passes over x_0 it would have an infinite amplitude and a relatively small (ideally zero) amplitude everywhere else. This can be expressed using the Dirac Delta function:

$$\begin{aligned} g(x) * m(x) &= \delta(x - x_0) * f(x) * m_{ideal}(x) + n(x) * m_{ideal}(x) \\ &= \delta(x - x_0) + 0(x). \end{aligned} \tag{4.29}$$

This expression can be restated in the frequency domain as:

$$\begin{aligned} G(\xi) * M_{ideal}(\xi) &= (F(\xi)e^{-2\pi i \xi x_0}) \cdot M_{ideal}(\xi) + N(\xi) \cdot M_{ideal}(\xi) \\ &= e^{-2\pi i \xi x_0} + 0(\xi). \end{aligned} \tag{4.30}$$

So from Eq. 4.29 and Eq. 4.30 we can see that two conditions must be satisfied in both the spatial and frequency domains:

$$f(x) * m_{ideal}(x) = \delta(x) \Longrightarrow \mathcal{F}\{\} \Longrightarrow F(\xi) \cdot M_{ideal}(\xi) = 1(\xi) \tag{4.31}$$

$$n(x) * m_{ideal}(x) = 0(x) \Longrightarrow \mathcal{F}\{\} \Longrightarrow N(\xi) \cdot M_{ideal}(\xi) = 0(\xi). \tag{4.32}$$

The ideal filter in the Fourier domain is evaluated as:

$$M_{ideal} = \frac{1}{F(\xi)} = \frac{F^*(\xi)}{|F(\xi)|^2} = \frac{e^{-i\Phi\{F(\xi)\}}}{|F(\xi)|}. \tag{4.33}$$

This is derived in the spatial domain as:

$$m_{ideal} = \mathcal{F}^{-1}\{F^*(\xi)\} * \mathcal{F}^{-1}\left\{\frac{1}{|F(\xi)|^2}\right\} = f^*(-x) * \mathcal{F}^{-1}\left\{\frac{1}{|F(\xi)|^2}\right\}. \tag{4.34}$$

Equations 4.33 and 4.34 clearly show the problem with the ideal matched filter. If $g(x)$ contains wideband random noise the filter will amplify noise frequencies at any frequency where $|F(\xi)| < 1$. One way of obviating this problem is to throw out the second term in Eq. 4.34:

$$M(\xi) = F^*(\xi) \Longrightarrow m(x) = f^*(-x). \tag{4.35}$$

The correlation plane will often contain "false" peaks just as high as the peak created by the actual object. In this case simply taking the maximum of the correlation plane (as specified in Eq. 4.28) will often result in a false alarm. Luckily these erroneous peaks will also have sidelobes that can be used to our advantage in a post-processing step shown by Kumar et al. (2005). This is simply done by convolving a window over the correlation plane, and within the window finding the standard deviation and mean, which can be used with the pixel value the window is centered over (labeled as "peak" in Eq. 4.36) to calculate a peak-to-sidelobe ratio. The user can define the size of the window from which the PSR is calculated. In this effort the window size was the same size and dimension as the array that held the target for the matched filter.

$$PSR = \frac{peak - \mu}{\sigma} \tag{4.36}$$

This makes perfect sense because an area with sidelobes will have a large standard deviation and a large mean which will subsequently reduce the PSR value. Conversely, the correlation plane over a target will have no sidelobes and therefore a lower mean and a lower standard deviation, which will result in a higher PSR.

An example of this procedure is provided in the following paragraphs and figures. The matched filter is applied to a green band $(500 - 590nm)$ "imaged" by a system with primary aperture aberrations of .2 PTT and .2 flimsy WFE. The first step taken is to isolate the target (shown in Figure 4.22(a)) and threshold it (shown in Figure 4.22(b)). If you have knowledge

of your system OTF it can be used to degrade the target to produce an estimate of what it might look like (shown in Figure 4.22(c), in this case we have .05 RMS WFE knowledge).

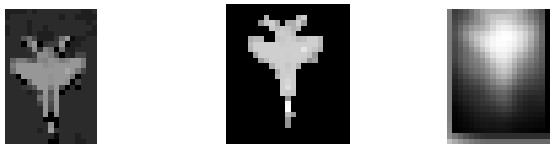

(a) Original jet target (b) Thresholded jet target (c) Degraded estimate of jet target

Figure 4.22: This figure shows several zoomed views the jet target at various stages of the algorithm.

The original image (shown in Figure 4.23(a)) is then degraded using the model (shown in Figure 4.23(b)) and the matched filter is applied. Figure 4.23(c) shows the correlation plane of the matched filter. Notice that the peak above the target does not come to a sharp point, to analyze how sharp the peak is we can use the PSR. Another thing to point out is that the values above the buildings in the upper right of the image are noticeably higher than the target value. These peaks would create false alarms in a target detection scenario; however, the after the PSR is applied these false alarms are reduced to values below target value. This can be seen in both Figure 4.23(d) and Figure 4.24. Figure 4.24 shows the column of correlation values and PSR values that the target sits in. Notice for the correlation plane values (shown in black) at approximately location 280 there is a spike corresponding to the target. Also notice the peak at approximately location 460, this peak corresponds to the peak caused by the building. After the PSR is applied the value over the target remains relatively high (observe red line) while the value over the building is comparatively much lower. There is a further discussion of how the target PSR value stands in relation to the PSR values of the scene (expressed in standard deviations from the mean PSR value) in Section 5.4.

4.9.1.2 The Spatial Target Detection Experiment

The match filter relies heavily on good training data, this experiment will use synthetic DIRSIG data which allow us to build a very good matched filter. In this experiment a fighter

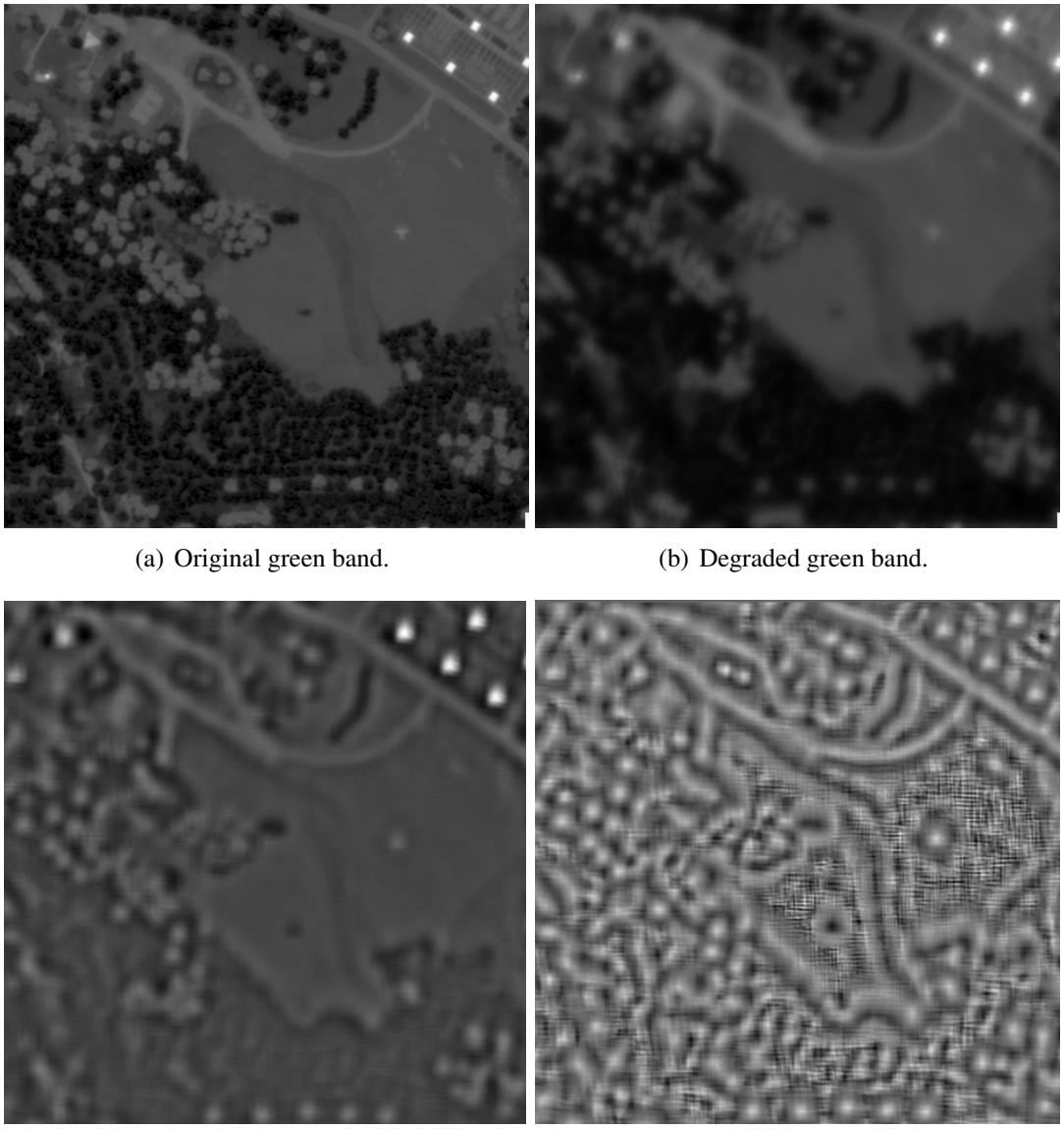

(a) Original green band. (b) Degraded green band.

(c) Correlation plane. (d) PSR plane.

Figure 4.23: This figure show various stages of the input image as it is fed through this experiment.

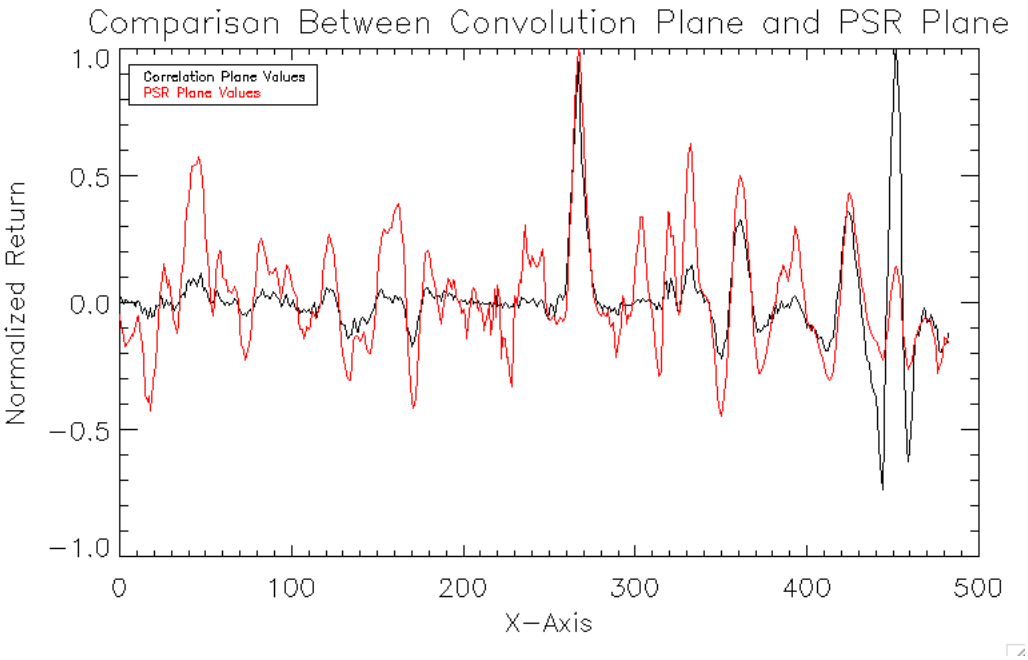

Figure 4.24: .

jet (see Figure 4.22) will be the target of interest and the main goal will be to observe the peak corresponding to the target in the PSR plane for a multitude of imaging sensors. By observing the peak over the target in the PSR plane for a given system scenario one could get an idea of how well that system performs. The operator could then alter one parameter in the system model, output another image, apply the matched filter and again observe the height of the peak in the PSR plane. This process could be repeated many times (observe Figure 4.25) By recording all of the input values and heights of the PSR one could rank the different imaging systems based on their ability to perform spatial target detection. There was some interest in repeating these tests with the object rotated and/or scaled, but this was dismissed because we are only interested in the relative performance between systems. We therefore decided we would know the scaling and rotation and that we didn't need to look into any rotation or scaling invariant detectors.

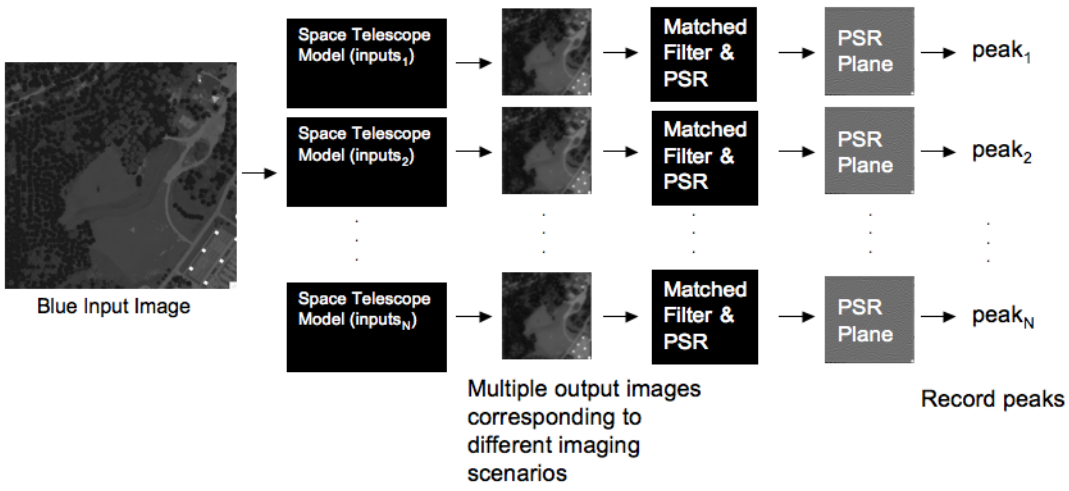

Figure 4.25: The output peak values can be used to understand the system parameters important to spatial target detection.

4.9.2 Motion Detection

Another way of quantifying the potential utility of an imaging system is to process video data with the system model and then use the degraded output video with a motion detection algorithm that will give us some information about how much motion was detected. A DIRSIG video has been rendered that includes moving cars, trucks, a battle tank, helicopter, a flying fighter jet, and several walking people (see 4.26). This video signal can easily be broken up frame by frame and processed through the space telescope simulation tool. After the video is run through the space telescope simulation tool it can be used with a motion detection algorithm that Andrew Adams developed (Adams (2008)). Because the data came from DIRSIG it is trivial to generate truth data that the algorithm will use to determine the number of false alarms and missed detections. These two output values can be used to rank a system's performance.

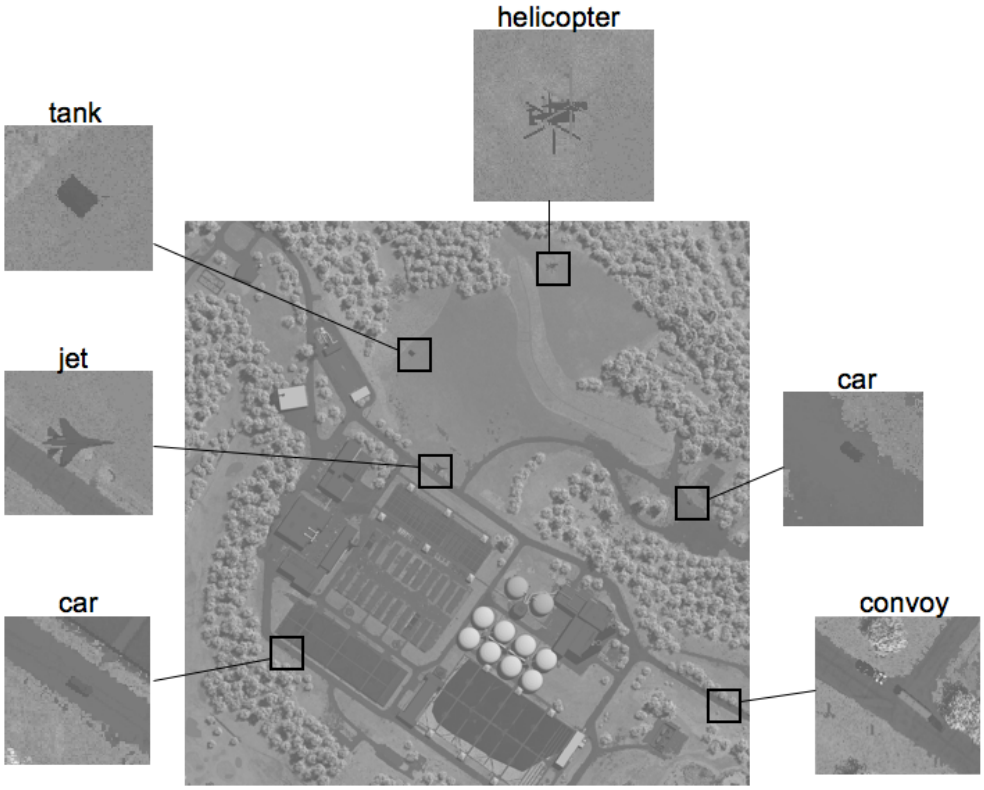

Figure 4.26: This is a NIR image with the moving objects labeled (except for the people).

4.9.2.1 Motion Detection Algorithm

This section will provide a brief overview of Andrew Adams's motion detection algorithm. Figure 4.27 describes the algorithm in its most basic form. The author will refer back to this figure through out the description of the motion detection algorithm.

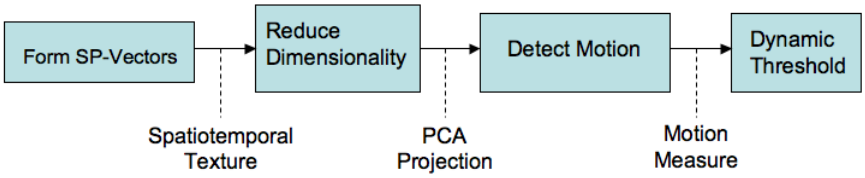

Figure 4.27: Motion detection algorithm flowchart.

The interesting thing about this algorithm is that it is a hybrid algorithm that uses both temporal and spectral information. The algorithm's foundation depends upon two simplifying assumptions: first, the scene collection was assumed to be from a stationary platform, and second, the pixels were assumed to be registered to within one pixel of accuracy.

The algorithm begins by breaking each spectral image into 3x3 blocks (in this example). It is within these blocks that the algorithm will "look" for motion over several temporal frames. However, before it does this it first uses information from 1 (or more) frame(s) ahead and 1 (or more) frame(s) behind its current temporal location. The pixels within each block are then reordered into spatiotemporal texture (SP) vectors as shown in Figure 4.28. This is also shown in the first box of Figure 4.27.

Figure 4.28 shows the single band case looking ahead and behind 1 frame, we therefore have 27 values. If there are more bands, for example 3 bands, we would have 81 brightness values. So turning this single band motion detection algorithm into a multi-spectral algorithm is quite easy.

The dimensionality is reduced by doing Principle Components Analysis (PCA) on the SP-vectors. This is done by processing one spatial block location (i,j) over the entire video sequence (consisting of N frames). The SP vectors first are placed in the rows of a N x 27 matrix (for the single band case). PCA is then performed on the rows of this matrix which reduces the dimensionality to N x k, where k is the number of principle components

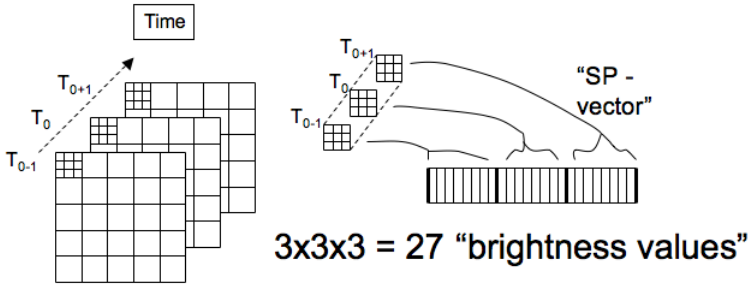

Figure 4.28: The diagram above shows how the image is broken up into 3x3 blocks. And then how the 3x3 blocks are reordered into vectors.

that are kept. Observe Figure 4.29 where k = 10. To restate this more clearly, we had 27 brightness values that represented 1 block over one band at 3 different times, and if there is any motion within this block there will be some variability within these 27 brightness values. If PCA is performed on these 27 values and it is found that only 10 values are needed to accurately explain the motion in the block, the motion detection algorithm will become far more computationally efficient. So just to again restate what is going on here with an example. Say we have 300x300 pixel images over 3 bands at 3 times, this would get broken into 3x3 blocks, the resulting PCA output would be reordered into one 100x100x10 PCA image. Each pixel in the PCA image would represent the variability over the three bands over the three times within the 3 x 3 block.

The motion detection part occurs when the algorithm looks ahead and behind the current frame. The algorithm takes a pixel in the PCA stack - which consists of 10 PCA values - for the current frame, the past three frames, and the future three frames, and reorders each "PCA pixel" into the rows of a 7x10 matrix, where 7 represents the 7 frames and 10 represents the 10 PCA values (observe Figure 4.30). The (10x10) covariance of the (7x10) array is computed. Basically, this is just a simple measure of the variability between the 10 PCA terms. Finally, the largest eigenvalue of this covariance matrix is computed and labeled as the "motion measure" (mm). Standing back what we have just done is simple, we broke the frame up into little blocks and labeled each block with a single mm value where a large mm value corresponds to a large amount of motion. Of course, there will be noise in the sensor, and the trick now is to label motion that is not noise. This is done using the dynamic

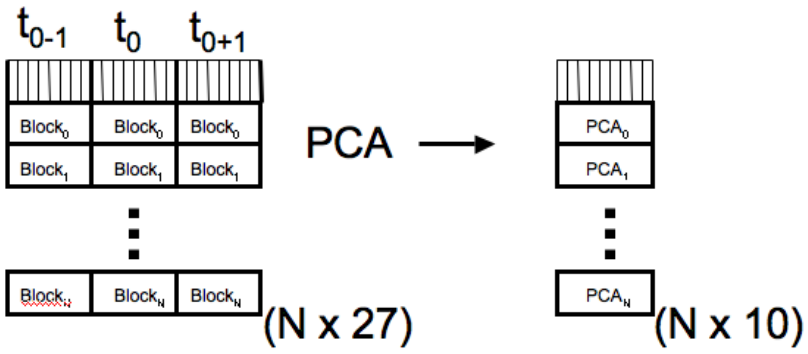

Figure 4.29: This diagram shows how the block data is placed into the rows of an N x 27 matrix. PCA is then performed on the rows of the data and the dimensionality is reduced from N x 27 to N x 10.

threshold.

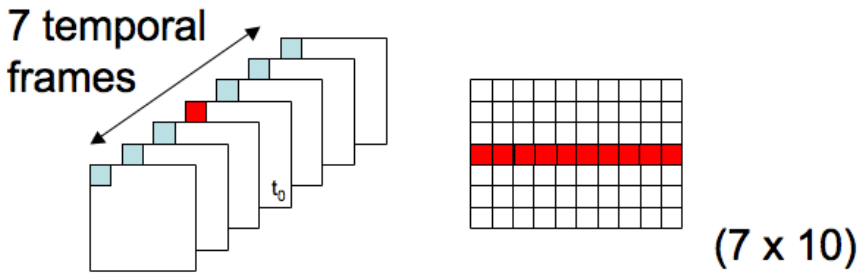

Figure 4.30: This figure shows the reordering of the PCA image for 3 frames ahead and 3 frames behind the current frame.

The dynamic threshold looks at the mm-value of the current block and uses information of all previous mm-values for that block (observe Eq. 4.37). If it exceeds the threshold C_1 the block is labeled as containing motion.

$$\frac{f(t) - mean(f(t_0, t_1, ...t))}{std(f(t_0, t_1, ...t))} < C_1 \tag{4.37}$$

The block will remain labeled as containing motion until the computed value falls below

C_2.

$$\frac{f(t) - mean(f(t_0, t_1, ...t))}{std(f(t_0, t_1, ...t))} < C_1 \; where \; C_2 < C_1 \tag{4.38}$$

Adams (2008) gives common values for C_1 and C_2 as 50 and 10 respectively.

The final step is to convert the detection data from pixel space to object space. Object space is chosen over pixel space because this is what analysts care most about. Object space pertains to the objects moving through the scene NOT the pixels that make up the moving object. It doesn't matter if an object fills 100 pixels or 1 pixel, the algorithm will detect and record only one object. Ultimately, it will reduce the number of false alarms because in pixel space if an object is blurred the detection algorithm will falsely detect pixels adjacent to the object. In other words, in object space we don't concern ourselves with erroneous detections at the edge of the objects.

To convert the data from pixel space to object space we first reduce the size of the motion map; by doing this the singular detections that are usually caused by white noise are removed. The reduced motion map is then dilated to its original size, the remaining motion map contains only the large moving objects. Doing this reduction and dilation is analogous to low pass filtering the motion map. And because of this low pass filtering the blobs that remain have lost much of their fine (high frequency) detail. Some of the original features can be restored by comparing the filtered motion map to the original motion map and then eroding the larger 'rough' blobs to match the original ones. The resulting motion map contains only the objects that are larger than or equal in size to the reduction factor. The reduction factor is a factor that describes the amount that the original motion map is resized. For example, a reduction factor of 2 would reduce a 2x2 object to 1x1.

Because we are using synthetic imagery that contains no noise or global scene motion it is easy to create motion truth. Motion truth data was created by first averaging 20 unprocessed frames around the current frame (that is 10 frames ahead and 10 frames behind the current frame). By differencing the average and the current frame the pixels that contain motion will be the only pixels with any value. The differenced frame can then be thresholded and the pixels containing motion can be given a numerical label. Once this is done Adams's algorithm will use the motion truth to present a number of missed detections and false alarms. These two numbers can be used to calculate the percentage of moving objects detected.

4.9.2.2 Output Interpretation

The algorithm will use the motion truth data to count the total number of moving objects in all the frames. It then repeats this, counting the total number of moving objects in the detected motion map. Then it compares the truth motion map to the detected motion map and counts the number of correctly identified moving objects. Using this information the algorithm can compute the percentage of detected motion and the percentage of false alarms. The percentage of detected motion is calculated as:

$$\%DetectedMotion = 100 * \left(1 - \frac{TotalTruth - TotalCorrect}{TotalTruth}\right) \tag{4.39}$$

The percentage of false alarms is calculated as:

$$\%FalseAlarms = 100 * \left(1 - \frac{TotalDetected - TotalCorrect}{TotalTruth}\right) \tag{4.40}$$

Chapter 5

Results

The results presented in this section will begin with a study of space telescope capabilities and demonstrate the model's effectiveness as a tool for this problem. It then covers the results from the motion detection experiments and uses several different visualization techniques to illustrate the main results. Lastly it covers the spatial target detection and GIQE results.

It is important to say that when the author writes about a particular amount of aberration, such as '.3 RMS PTT aberration' the units are in waves with a reference wavelength of 550nm. This means that '.3 RMS PTT aberration' could be more clearly stated as '.3 RMS waves of PTT aberration with a reference wavelength of 550nm'.

5.1 Practical Space Telescope Capabilities

This section will provide several examples of segmented aperture space telescopes and their capabilities in areas such as field of view, GSD and SNR. The objective of this section is to give the reader an understanding of the capabilities of these systems. Hopefully they will understand that a lot can be done to change the design of these telescopes. The very few examples presented here should give a general idea of some potential design parameters and the characteristics these systems will possesses. The effects of aperture aberrations will not be considered here.

5.1.1 Space Telescope Field of View

The telescope can be designed so that multiple sensors can be placed on the focal plane. A diagram of the James Webb Space Telescope's (JWST) focal plane is below in Figure 5.1. Any detector placed within the orange region of the focal plane will produce clean images even at the shortest spectral wavelengths the JWST is capable of operating at. The field of view can be determined by simple math: $(|-5.7|+|3.4|)*(|-9.1|+|9.1|) = 165.6 arcmin^2$ This doesn't take into account the regions that lie outside of the focal plane which are marked as black, so this value is not accurate but it does give the reader an idea of size of FOV. The amount of ground this would cover at a geo-stationary orbit (35,786,000 [m]) can be determined easily. An arc minute is $\frac{1}{60}$ of a degree. The horizontal length is $tan(\frac{18.2}{60})*35,786,000[m] = 189458.77[m] = 189.5[km]$ and the vertical length is $tan(\frac{9.1}{60})*35,786,000[m] = 94728.72[m] = 94.7[km]$.

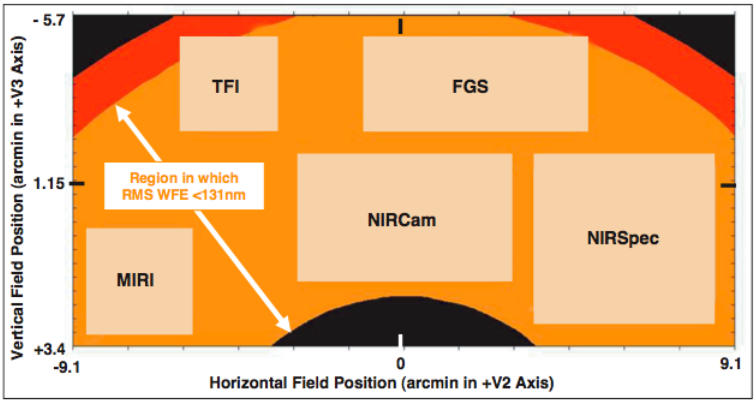

Figure 5.1: Focal Plane of the JWST [Gardner and et. al. (2006)]

The systems described in this paper operate at lower spectral wavelengths than the JWST, and the amount of allowable error off the optical axis will be reduced; therefore the telescope will likely have a smaller focal plane and subsequently a smaller FOV. Much of this discussion really depends on the design. For the purpose of this discussion we will assign a conservative value for the system's FOV spanning 10 arc minutes in the horizontal direction and 5 arc minutes in the vertical direction. If we converted this to kilometers on the ground it would be $tan(\frac{10}{60}) * 35,786,000[m] = 104097.55[m] = 104.1[km]$ and the vertical length

would be $tan(\frac{5}{60}) * 35,786,000[m] = 52048.664[m] = 52.0[km]$. Just so the reader gets an idea of the amount of land that is covered by this FOV observe the image of a 52[km] x 104[km] section of New England that was taken from a Google Earth image in Figure 5.2. This figure shows downstate New York, and Northern New Jersey; it was chosen because it is a well known part of the world that readers will likely be familiar with. The telescope would be capable of viewing any land within this FOV immediately. The resolution of the images depend on a several parameters lightly discussed in the next section (5.1.2).

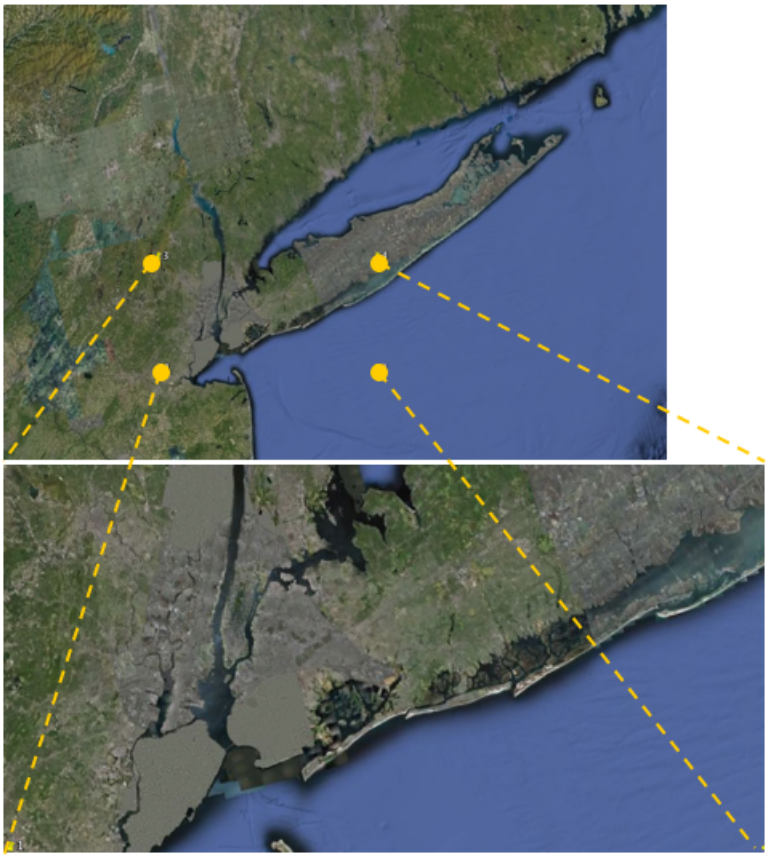

Figure 5.2: This figure shows the amount of land that is covered by the FOV.

5.1.2 Segmented Aperture System Examples

This section is included so that in the following sections when the reader sees a system that has 1m GSD and an SNR of 100 they understand what system parameters are necessary to build such a system. The data that was used was created by DIRSIG and models a suburban neighborhood on the equator during the summer at noon. Looking back to Figure 4.4, all parameters in this figure were kept constant except the values showing change in Figure 5.3. All detectors modeled here used the same read and dark noise values for each scenario.

pixel pitch [um]	GSD [m]	Aperture Diameter [m]	Focal Length [m]	F#
6.50E-06	1.163045	8.4615385	200	23.636364
7.50E-06	1.07358	9.1666667	250	27.272727
4.50E-06	1.07358	9.1666667	150	16.363636
4.50E-06	1.61037	6.1111111	100	16.363636
6.50E-06	1.5507267	6.3461538	150	23.636364
6.50E-06	2.32609	4.2307692	100	23.636364

std(dark)	std(read)	SNR-Blue (e^-)	SNR-Green (e^-)	SNR (Red)	SNR (NIR)
2.93E-06	20	88.769471	150.02137	118.9396	329.43456
2.93E-06	20	78.312857	130.17758	105.03387	281.48428
2.93E-06	20	78.249055	130.17147	105.38436	280.04114
2.93E-06	20	153.06021	261.49927	204.27	606.19747
2.93E-06	20	144.54972	249.13489	195.20647	560.7876
2.93E-06	20	277.54993	460.7609	356.21422	942.42671

Figure 5.3: Plausible system parameters.

5.2 Effects of Aberrations and Spectral Wavelength

Once work began with the more aberrated apertures it was apparent there was an interesting paradox between the optical cutoff frequency and the aperture aberrations. This can be better understood by viewing the equation for optical cutoff frequency:

$$\nu_c = \frac{D}{\lambda_l f} = \frac{1}{\lambda_l f\#}. \tag{5.1}$$

where D is the diameter of the primary mirror, λ_l is the wavelength, and f is the focal length. The equation for the pupil function is:

$$p(x,y) = |p(x,y)|e^{\frac{2\pi i}{\lambda_0} WFE(x,y)\left(\frac{\lambda_0}{\lambda_l}\right)}. \tag{5.2}$$

where λ_0 is the reference wavelength and the phase error is proportional to $\frac{1}{\lambda_l}$. The important thing to notice is that as the wavelength increases the cutoff frequency decreases, this means that only progressively lower valued spatial frequencies will be passed to the focal plane - **decreasing** image quality. Conversely an increase in wavelength causes the apparent wavefront error $\left(\frac{WFE}{\lambda_0}\frac{\lambda_0}{\lambda_l}\right)$ from Eq. 5.2 to decrease, which results in an **increase** of image quality. We find that in severely aberrated scenarios this becomes quite important. An example of this is covered in the following paragraphs.

Figure 5.4(a) shows the MTF of the blue (450nm) band calculated from a highly aberrated pupil function. The cutoff frequency extends beyond the Nyquist sampling frequency, this results in some aliasing near the ξ and η axis. Note that the MTF is hardly passing any energy at the mid and high spatial frequencies; this is a result of the large phase error caused by using a relatively small (450nm) wavelength compared to the reference wavelength (550nm). The effects of this are detrimental to the sharpness of the image. Figure 5.4(b) is a gray scale image of the unrestored blue band; notice how the roads and buildings are not clear.

Figure 5.5(a) gives us some perspective on how the apparent aberration and spectral wavelength can impact image sharpness. Here (at 800nm) we find that the cutoff frequency is much lower. However, the apparent aberrations levels are now diminished and the effects of these aberrations are not nearly as sever; this allows the MTF to inflate and pass mid-range spatial frequencies. Notice in Figure 5.5(b) how the unrestored image shows the roads and buildings are clearer and in the bottom center a swept wing airplane is now visible. The end result is that the image sharpness for the NIR band is visibly better than the blue band. Image sharpness is in many ways directly related to the information content of the image. Having knowledge of the aberration level can be very useful because an estimate of image-information content can be made. And in this case we can find out at what levels of aberration a band should be dropped from a data set.

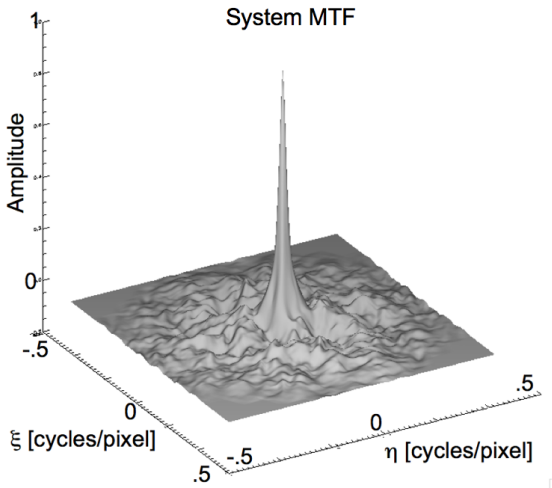

(a) System MTF

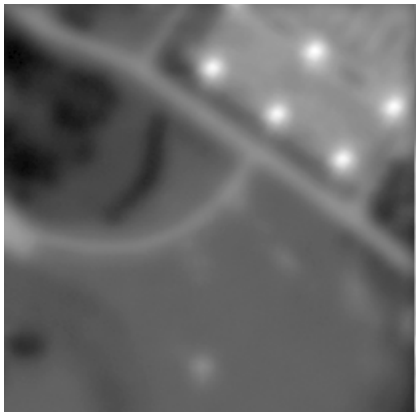

(b) Blue channel.

Figure 5.4: This figure shows MTF for the blue channel and a grey scale image of the unrestored blue channel.

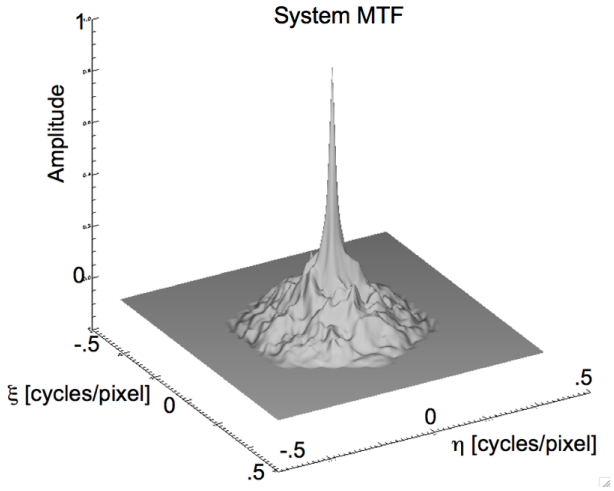

(a) System MTF

(b) NIR channel.

Figure 5.5: The MTF for the NIR channel and a grey scale image of the unrestored NIR channel.

5.3 Results from Motion Detection Experiments

The following subsections will look at the data from a variety of different ways. Mostly the sections will compare different band configurations, SNR levels, and GSD using surface plots where the x and y axis represent flimsy and PTT aberration levels respectively, while he z-axis will represent the % of motion detection. The last subsection utilizes iso-performance plots to visualize the same data in another insightful way.

The data used in this experiment is appropriate because it has objects of all different sizes, shapes, and spectral character - we assumed that having this kind of a varied environment would give us a general idea of a imaging scenarios capability. The reader can imagine that if all the objects were all the same shape, size, spectral character, and against the same background, that once a certain limit of aberration level, GSD, or band configuration, were approached the percentage of motion detection would drop dramatically.

The moving objects include two people, two cars, a convoy of cars and trucks, a battle tank, a helicopter, and a swept wing aircraft. All of these objects are accounted for in the motion truth. The reader might notice that even at the very best of imaging scenarios the highest % of motion detected is 80%. This 20% left undetected is the walking people which are too small to detect at 1m GSD. Acronyms were used to name the band combinations - "B" is "blue", "R" is "red", "G" is "green", and "N" is "near-infrared". "BGRN" would be a system that utilized blue, green, red, and near-infrared bands.

5.3.1 Comparison of 1m GSD, BGRN, and BGR Systems

This section compares BGRN and BGR systems at 1m GSD and three SNR levels. Each figure below has two subplots that show the front and side profiles of the motion detection data. The plots reveal a few general results that we would hope to find. In all cases as the aberrations increase the % of motion detection decreases. Notice that even at the lowest aberration levels the people are not detected and the highest % of motion detection is about 80%. An interesting result that can be seen in all figures is that the flimsy aberrations are not nearly as detrimental to motion detection as PTT aberrations. An example of this can be seen on the the BGRN surface in Figure 5.6(a). This figure shows that .1 RMS PTT and .6 RMS

flimsy system produces an equal % of detection as a .3 RMS PTT and .1 RMS flimsy system would - slightly under 60% detection. When comparing the flimsy aberrations to the PTT, the flimsy aberrations will have about twice as high % of motion detection for equal amounts of RMS WFE. This will be seen in every example presented in this document.

Many interesting things begin to happen when the SNR is lowered from 100 to 50 and then lowered again from 50 to 25. Figure 5.6 shows the data for the SNR of 100 scenario. We see that the BGRN setup produces a higher percentage of detection than the BGR. This is because adding the NIR band increases the amount of information that is useful to the motion detection algorithm. Figure 5.6(b) shows us a side profile of the data. Observe the BGR surface and notice that once aberrations increase to .3 RMS flimsy and .2 RMS PTT there is a rapid decline in motion detection. Thinking back to Eq. 5.2 we might expect this; as aberration levels increase linearly their effect on the pupil function is exponential and they therefore cause a rapid decrease in sharpness. The BGRN system is helped by the NIR band; the NIR band which is centered around 800nm has a longer wavelength and is therefore not affected as drastically by the aberrations. This is also a relationship that was predicted after viewing Eq. 5.2. In summary, the results presented here in this high SNR case could be easily understood and even predicted after viewing a few simple equations. The following results, which express system performance at lower SNR show that these systems have a more complex behavior.

Figure 5.7 shows BGRN and BGR systems with 1m GSD at an SNR of 50. At low aberration levels the BGR system outperforms the BGRN. As aberration levels increase the two systems have similar performance levels. Finally, as aberrations increase to high levels we see that the BGRN system outperforms the BGR. To understand this we must think back to the motion detection algorithm and realize that adding more bands doesn't necessarily provide more information. In fact, when working at low aberration levels adding the NIR band actually adds more noise than useful information to the data. This causes the % motion detection to drop. As aberration levels increase, the introduction of the NIR band provides no additional information to the data and the BGRN and BGR systems therefore produce equal performance. As aberration levels increase even further the NIR band is only band that still contains usable information, this increase in the % detection causes superior performance in

the BGRN system.

As SNR decreases to 25 the overall performance drops substantially; it is therefore only necessary to test low and mid range aberration levels. This can be seen in Figure 5.8. In this test we find that BGR systems consistently outperform the BGRN; this is a complete reversal from what was observed when the SNR was 100. What we find in this case is that the NIR band always brings more noise than information to the data. This causes the performance to decrease under all levels of aberration.

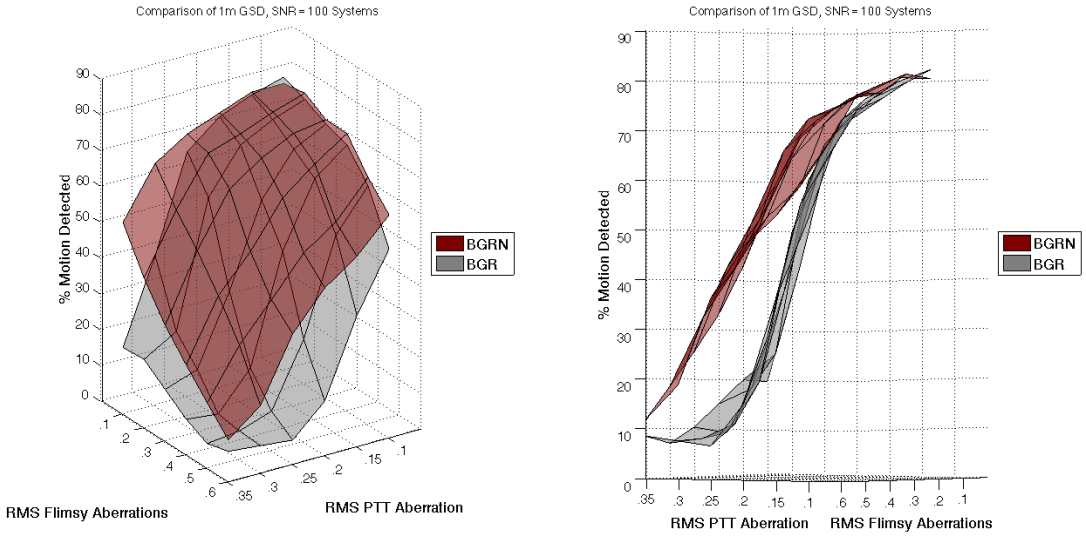

(a) Front view (b) Side view

Figure 5.6: BGRN and BGR, SNR = 100, and GSD = 1m.

5.3.2 Comparison of 1m GSD, BGRN, and RN Systems

This section compares BGRN and RN systems that have 1m GSD, allowing us to examine the importance of the blue and green bands. This experiment was done because the blue and green bands become optically degraded first as aberration levels increase.

When looking at Figure 5.9 we see that if the SNR equals 100 and aberration levels are low the BGRN systems have a higher % of motion detection than the RN systems. This

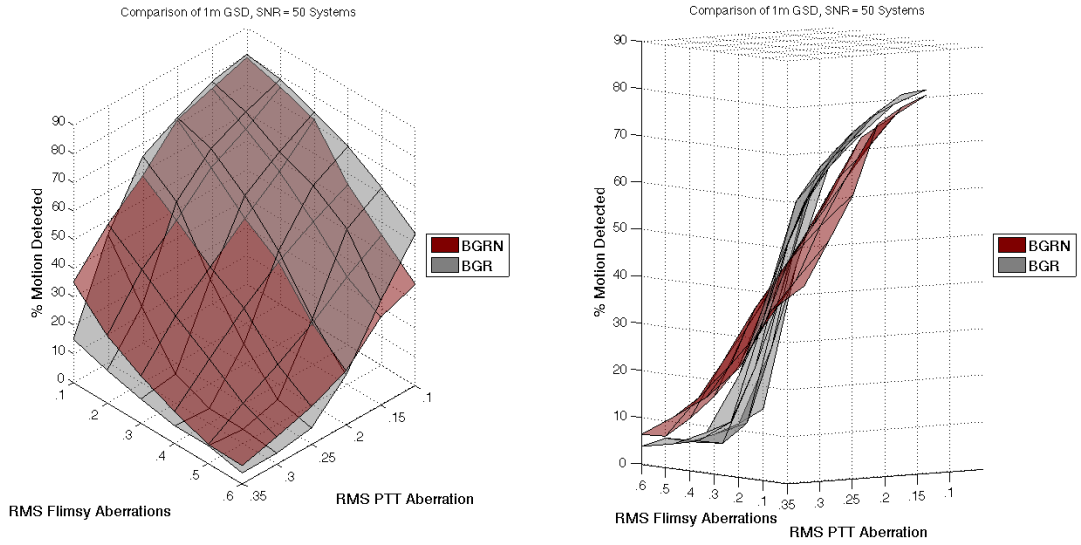

(a) Front view (b) Side view

Figure 5.7: BGRN and BGR, SNR = 50, and GSD = 1m.

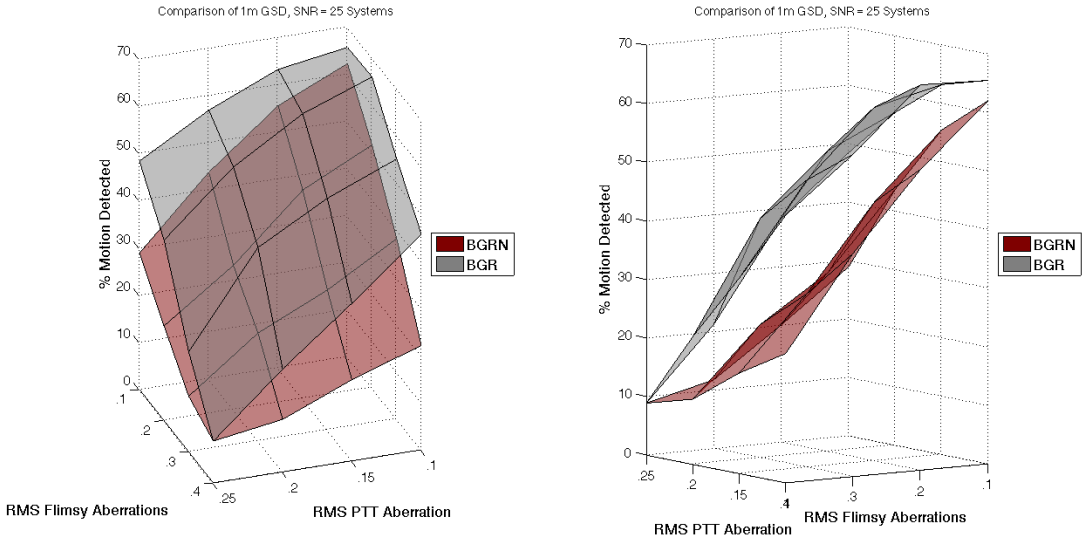

(a) Front view (b) Side view

Figure 5.8: BGRN and BGR, SNR = 25, and GSD = 1m.

is expected because the blue and green bands still have a good quality and provide useful information. However, as the aberration levels increase towards moderate levels, and the blue and green bands blur, the RN performs slightly better than the BGRN. Introducing aberrated blue and green bands brings more noise than useful information to the data when the aperture is moderately to highly aberrated.

As SNR decreases to 50 (observe Figure 5.10) we find that the RN scenario mimics that of the BGR system described in Section 5.3.1. At low aberration levels the RN system slightly outperforms the BGRN, however at mid and high level aberrations it underperforms. With the addition of more sensor noise and higher levels of aberration the blue and green bands contain a small amount of information that is not available within the RN bands. This is interesting because with a higher SNR (of 100) we deduced that the highly aberrated blue and green bands introduced noise to the data, however now that there is an increase in sensor noise the effects of the aberrations is somehow not as severe in a relative spectral sense.

Figure 5.11 shows systems with an SNR of 25. Here we see that the BGRN systems narrowly (but consistently) outperform the RN systems. The blue and green bands bring some useful information to the data in this high sensor noise case.

5.3.3 Comparison of 1m GSD, GRN, and RN Systems

The GRN and RN systems appear to perform equally well; this section will compare the two. Looking at Figure 5.12, we see when the SNR equals 100 the GRN outperforms the RN systems at most levels of aberration; however, overall the two systems have similar performance characteristics. There doesn't appear to be any trend that could be followed in these results that would allow us to say one system performs better than the other.

For an SNR of 50 (shown in Figure 5.13) we see some similarities between the results discussed in Section 5.3.2, only here the GRN system acts as a dampened version of the BGRN system. These band configurations have very similar performances; though, at low levels of aberration the RN band systems consistently outperform the GRN systems and at mid to high levels of aberration the GRN systems outperform the RN systems.

When the SNR is lowered to 25 (in Figure 5.14) we find that the GRN systems are consistently (although only slightly) better than RN systems. Again this mimics the SNR of 25

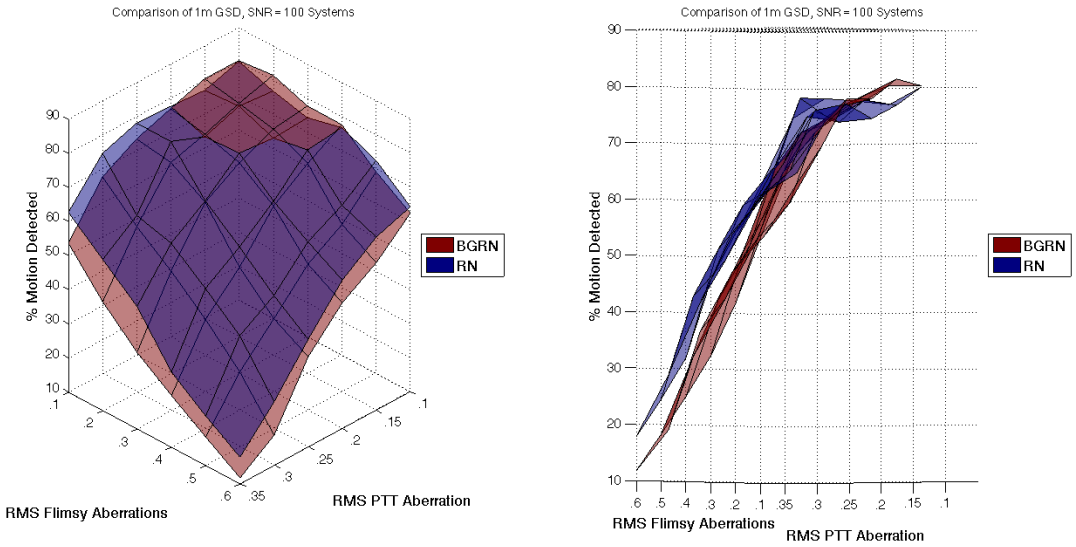

(a) Front view (b) Side view

Figure 5.9: BGRN and RN, SNR = 100, and GSD = 1m.

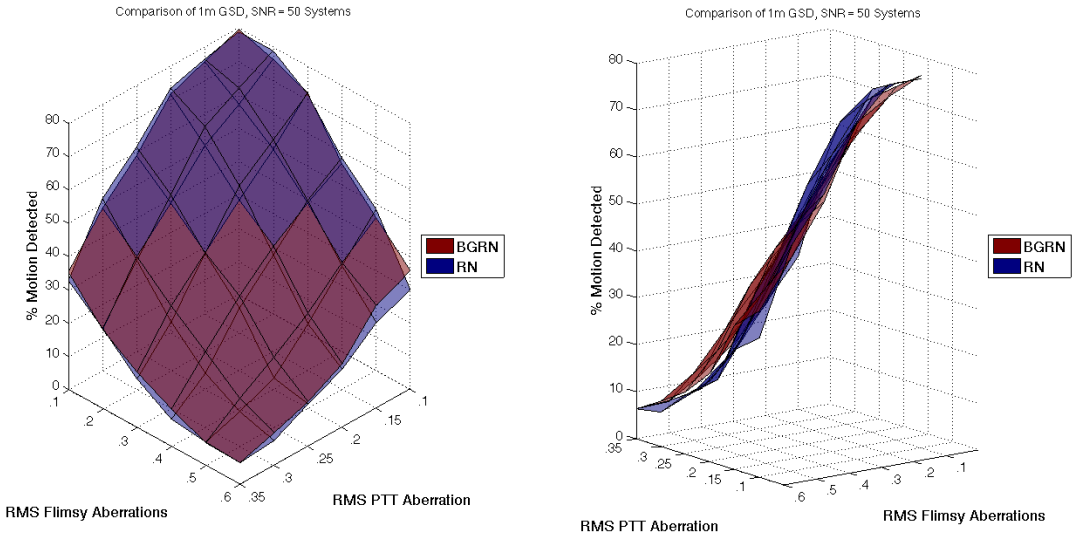

(a) Front view (b) Side view

Figure 5.10: BGRN and RN, SNR = 50, and GSD = 1m.

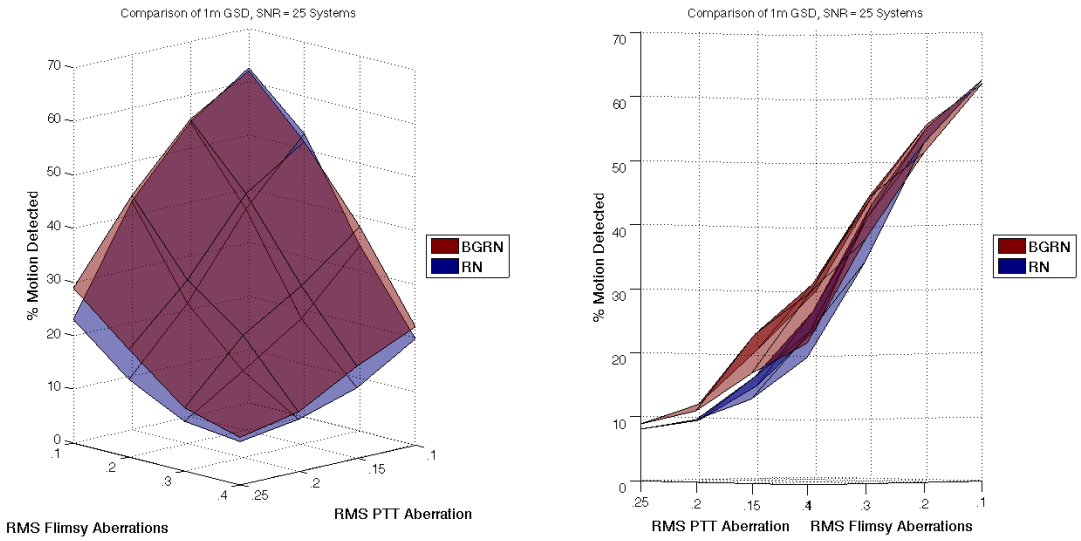

(a) Front view (b) Side view

Figure 5.11: BGRN and RN, SNR = 25, and GSD = 1m.

results of Section 5.3.2.

5.3.4 Comparison of 1m GSD, GRN, and BGR Systems

Up until this point we have observed how BGR and GRN system compare against other systems. It is only natural to compare the two and determine if there is a superior band configuration. What we find is that these results closely resemble those of 5.3.1.

Figure 5.15 shows the SNR of 100 scenario and the GRN system consistently outperforms the BGR system. However, at the lowest aberration level the BGR does have a higher value. This can be explained when we realize that the blue band (which is still sharp) has a higher cut off frequency than the NIR band and is therefore sharper (and containing more useful information). Please note that in these scenarios the background is quite important. If the NIR band produced higher contrast than the blue band this result could be different.

In Figure 5.16 we see that lowering from 100 to 50 has a large effect on the GRN scenario. Initially, at low levels of aberrations the BGR system is superior. Then, once aberration levels

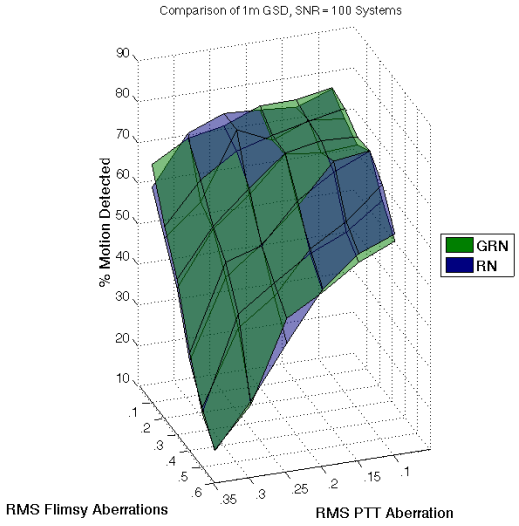

(a) Front view

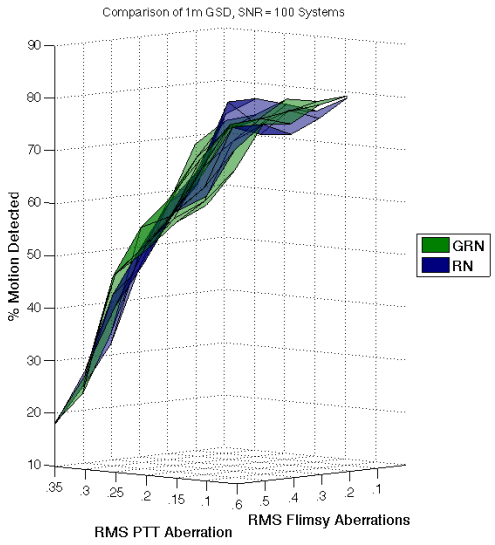

(b) Side view

Figure 5.12: SNR = 100

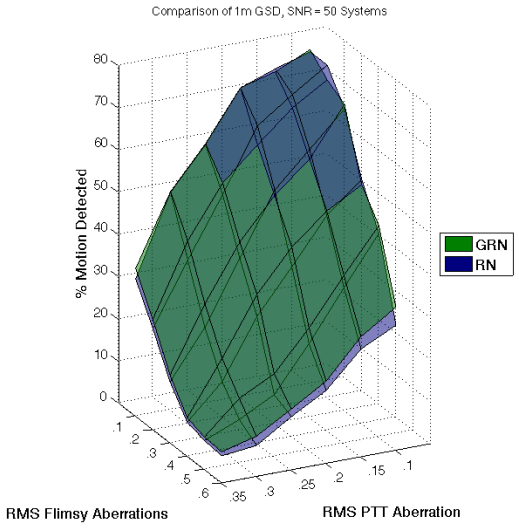

(a) Front view

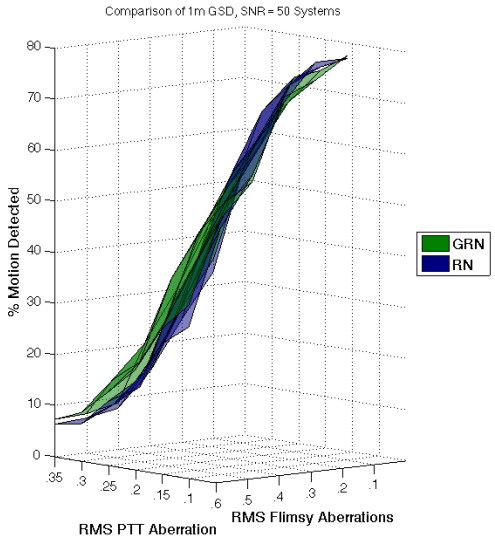

(b) Side view

Figure 5.13: SNR = 50

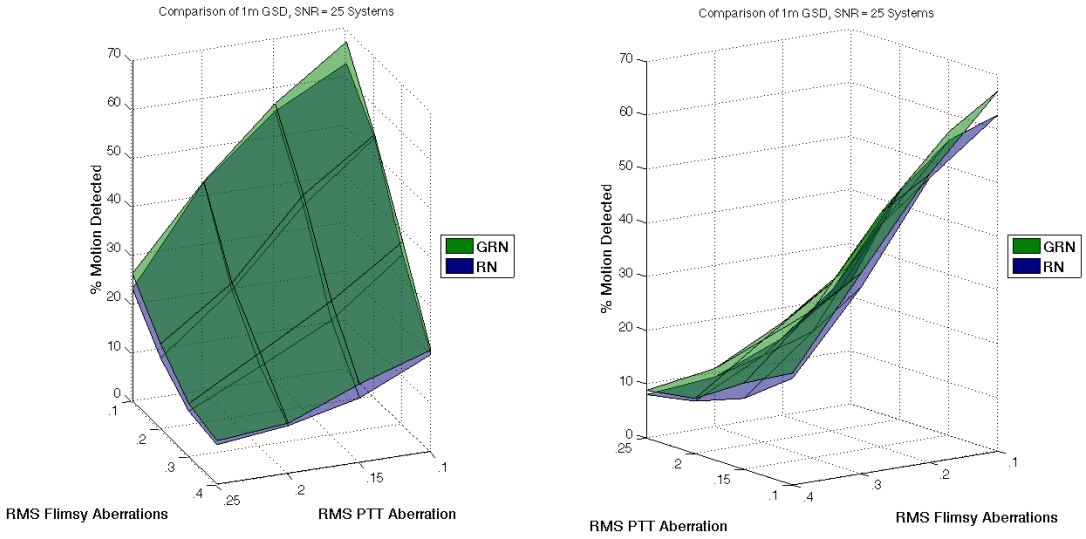

(a) Front view (b) Side view

Figure 5.14: SNR = 25

increase to moderate levels the two systems have equal performance. Finally, at the highest levels of aberration the GRN system outperform the BGR. This is because the NIR band is less aberrated than the other three and significantly improves detection performance.

If the SNR is lowered to 25 (shown in Figure 5.17) we see a complete reversal from what was observed in Figure 5.15. Here the BGR systems have better performance than the GRN systems. What we can conclude from this section and Section 5.3.1 is that the NIR band is not improving % motion detection when the SNR is low. This is an unusual result because with higher SNR the NIR band improves % motion detection. What we can infer from this is that the contrast between the moving objects and the background is low for the NIR band. This idea is reinforced when when we think about the comparison between BGR and GRN. The blue band has more contrast in between the objects and the background so even though it is less sharp than the NIR band (when the system is aberrated) it still provides more information in a low SNR scenario.

Notice that when the SNR equals 100 and the aberrations are low the % motion detection

is about equal (about 80% motion detection) for all band combinations.

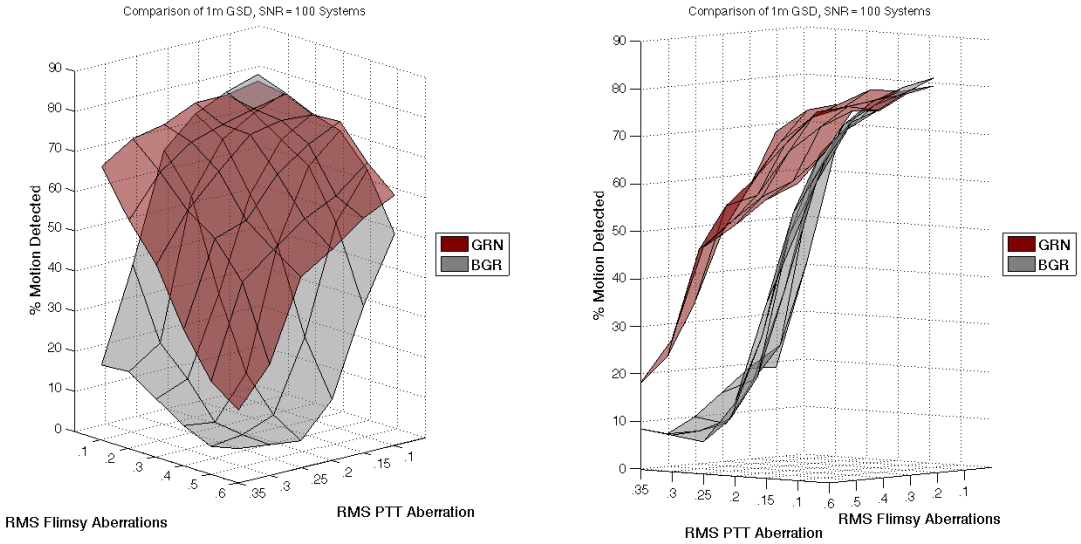

(a) Front view (b) Side view

Figure 5.15: GRN and BGR, SNR = 100, and GSD = 1m.

5.3.5 Comparison of 1m GSD, BGRN, GRN, and RN Systems at Isolated Levels of Noise

This section shows how the BGRN, GRN, RN, and BGR perform at noise levels of 100, 50, and 25. Figure 5.18 shows surface plots for BGRN systems at three noise levels. With each reduction in SNR we observe the expected drop in % of detected objects. One should note that the performance drops off more for the SNR interval of 50 to 25 than it does from 100 to 50.

Looking at Figure 5.19 we find surface plots of GRN systems at the three noise levels. The overall performance at an SNR of 100 might be a little better than the BGRN systems; at SNRs of 50 and 25 the performance looks very similar to the BGRN systems.

The RN systems shown in Figure 5.20 show how well these systems can operate as the

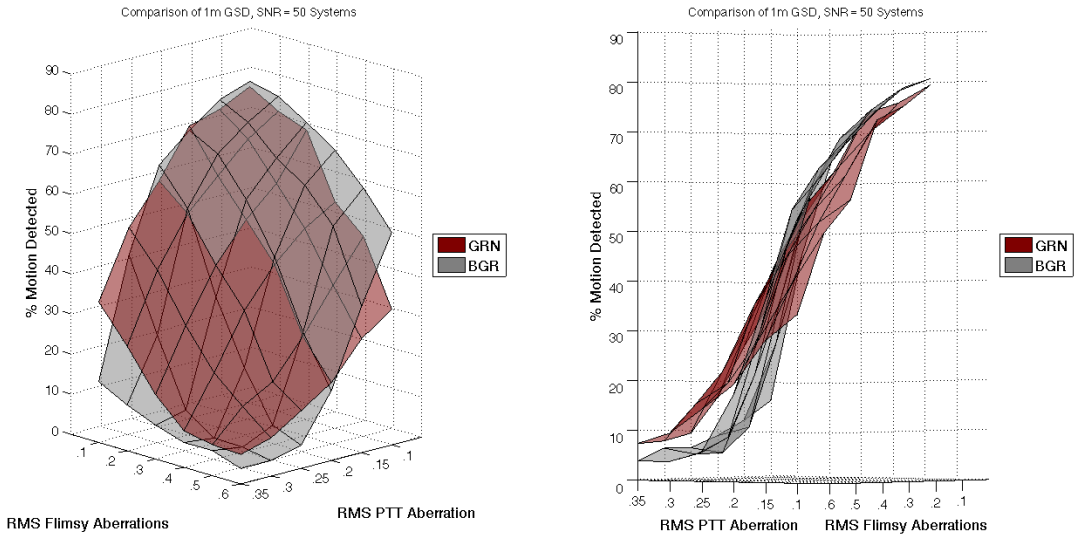

(a) Front view (b) Side view

Figure 5.16: GRN and BGR, SNR = 50, and GSD = 1m.

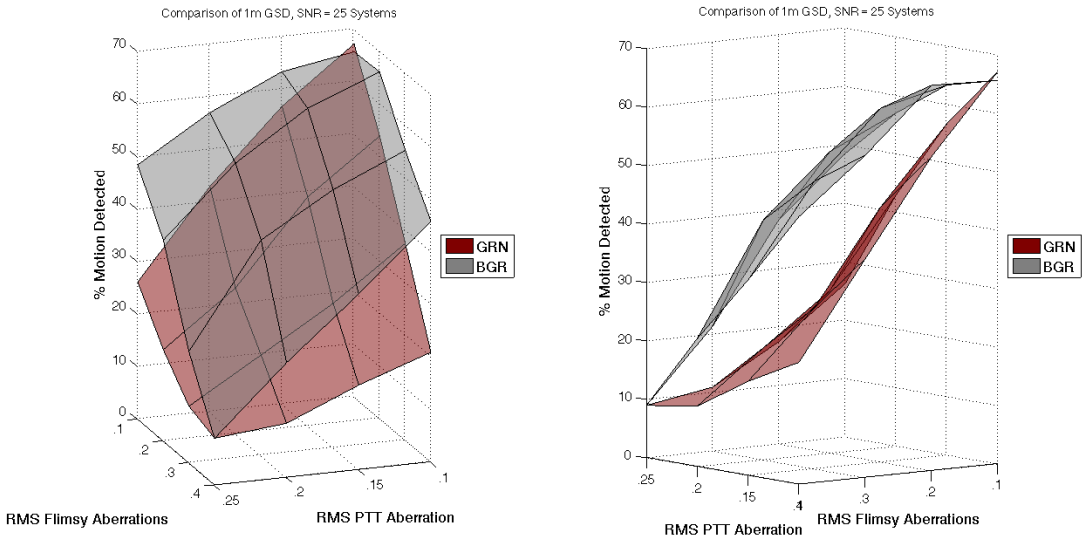

(a) Front view (b) Side view

Figure 5.17: GRN and BGR, SNR = 25, and GSD = 1m.

optics become slightly aberrated. In the SNR of 100 scenario this is particularly true. However, once a certain level of aberration is reached the performance drops off steeply with every subsequent addition of aberration. This can also be seen when the SNR equals 50; the performance is quite good at the first levels of aberration and then suddenly it drops off steeply.

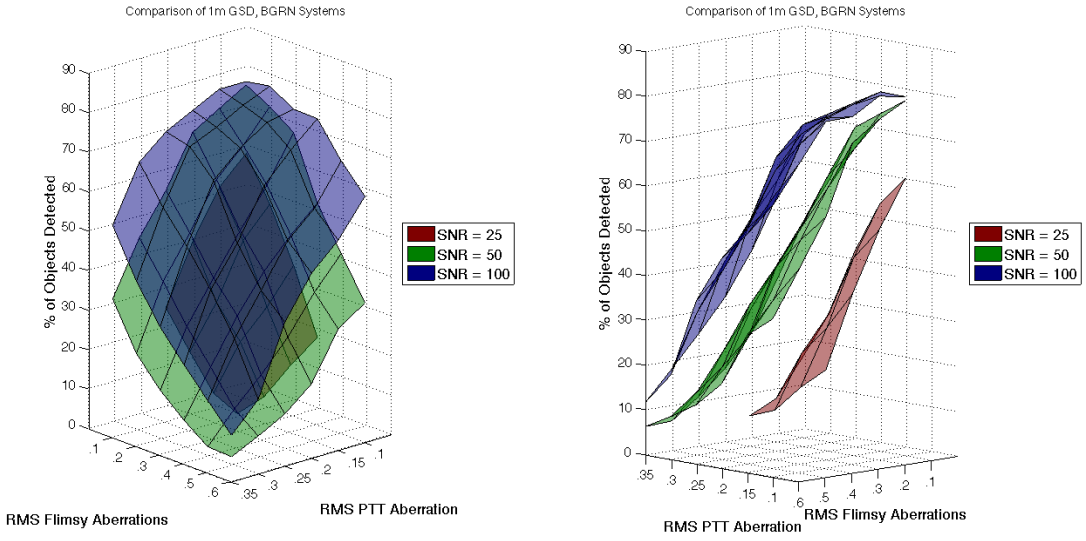

(a) Front view (b) Side view

Figure 5.18: BGRN Systems

5.3.6 Comparison of 1m and 1.5m GSD BGRN Systems

This section compares 1m and 1.5m GSD BGRN systems at SNR levels of 100, 50, and 25. Looking at Figure 5.21 we see 1m and 1.5m systems at an SNR of 100. At the lowest level of aberration (.1 RMS flimsy and .1 RMS PTT) the 1m GSD system can detect about 80% of the motion; the 1.5m GSD system performs almost equally well at about 75% motion detection. Observing values along the axis, as aberrations increase to either .2 RMS flimsy or .15 RMS PTT there is no change in performance for the 1m GSD system, while the 1.5m GSD system's performance decreases dramatically. With every increase in aberration level

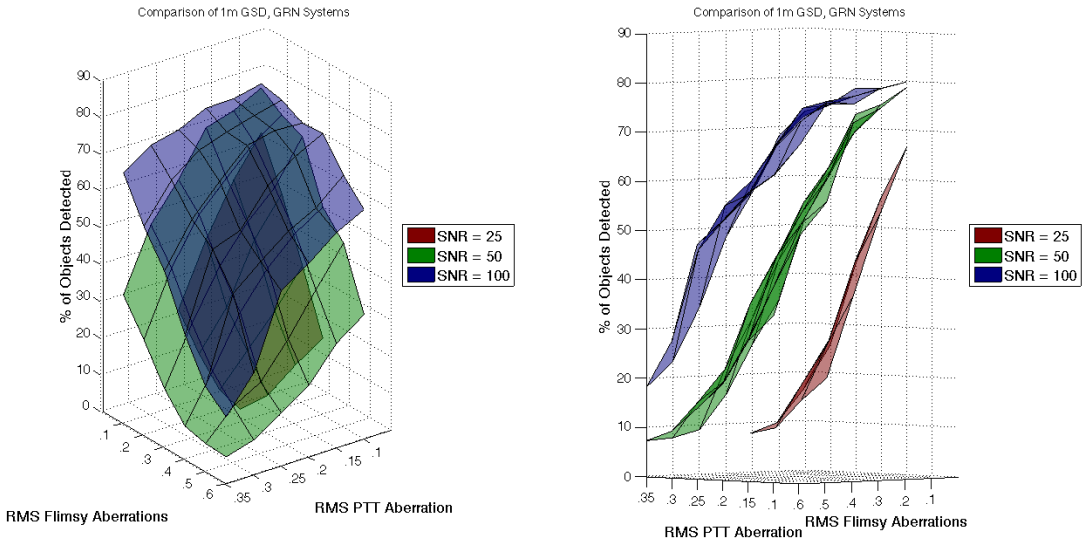

(a) Front view (b) Side view

Figure 5.19: GRN Systems

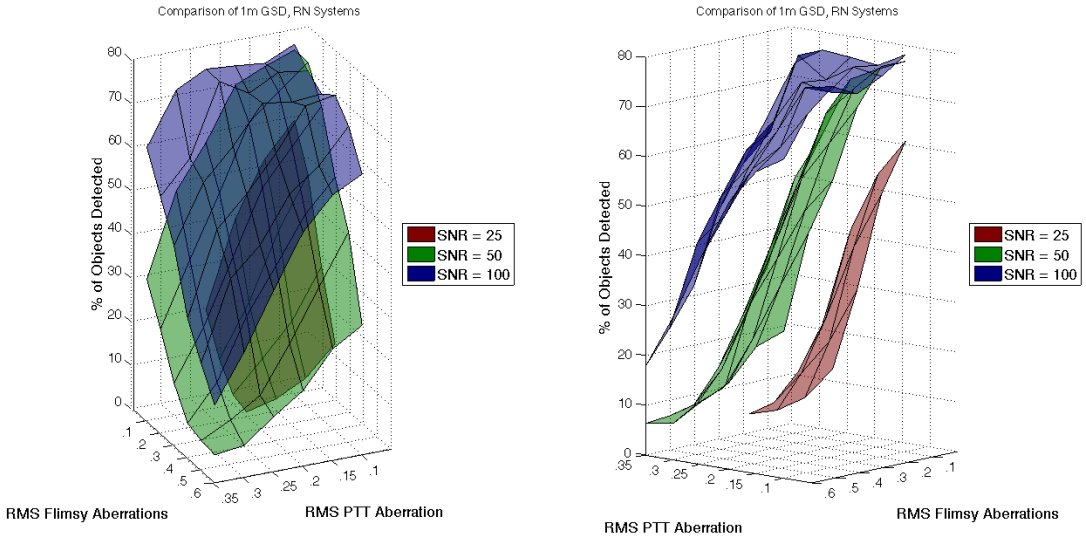

(a) Front view (b) Side view

Figure 5.20: RN Systems

there is a decrease in detection performance until high levels of aberration are reached and the detection performance begins to stabilize under 10%.

When the SNR equals 50 (see 5.22) we see that the 1m GSD system has only decreased a few percent for the .1 RMS flimsy and .1 RMS PTT case; however, the 1.5m GSD system has decreased from about 75% to about 63%. This is a substantial decrease in performance when compared to that of the 1m GSD. Again we see the 1.5m GSD case steadily declines with every increase in aberration level until higher levels of aberration are reached. In this medium level noise scenario we see that it does level out earlier than the low noise level scenario.

Figure 5.23 shows that the 1.5m GSD system is largely affected by detector noise. Here the SNR was again reduced by half, down to an SNR of 25, and the % of motion detection was also nearly reduced by half to about 35%. The 1m case also showed a relatively smaller decline from just under 80% down to just over 60%.

System engineers should pay attention here because a system's GSD often relates to important design characteristics such as F-number and SNR. This shows that a smaller diameter telescope with very low aberrations can perform as well as a potentially larger system that has a 1m GSD and moderate level aberrations. Smaller overall size could lead to a dramatic reduction in system cost because much of the total cost is related to payload size and weight. In addition to this a smaller system might be easier to build and operate.

Lastly, the results from 2m GSD experiments were not shown here or in the results chapter because they were completely unsuccessful. The motion contained in this video could not be detected at 2m GSD.

5.3.7 Comparison of 1.5m GSD, BGRN and RN Systems

This section will compare the BGRN systems to the RN systems at 1.5m GSD. Figure 5.24 shows that RN systems almost always outperform the BGRN systems at an SNR of 100. At low and mid-levels of aberration the RN systems significantly outperform the BGRN. At high levels of aberration the two systems are almost always equal and in one case the BGRN system outperforms the RN. As long as the sensor noise and aberrations are low an RN system will outperform a BGRN system. Section 5.3.2 revealed a slightly different behavior for the 1m GSD case.

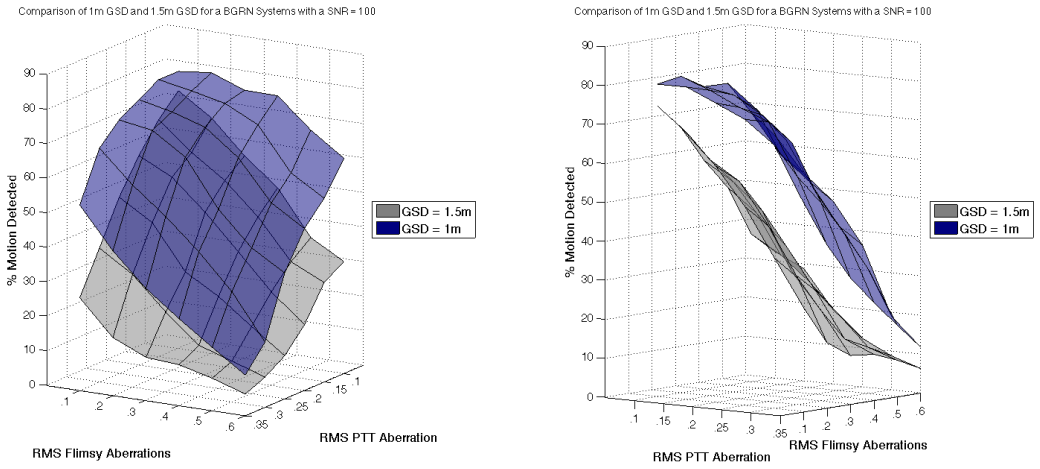

(a) Front view (b) Side view

Figure 5.21: BGRN Systems, with 1m and 1.5m GSD, and an SNR = 100.

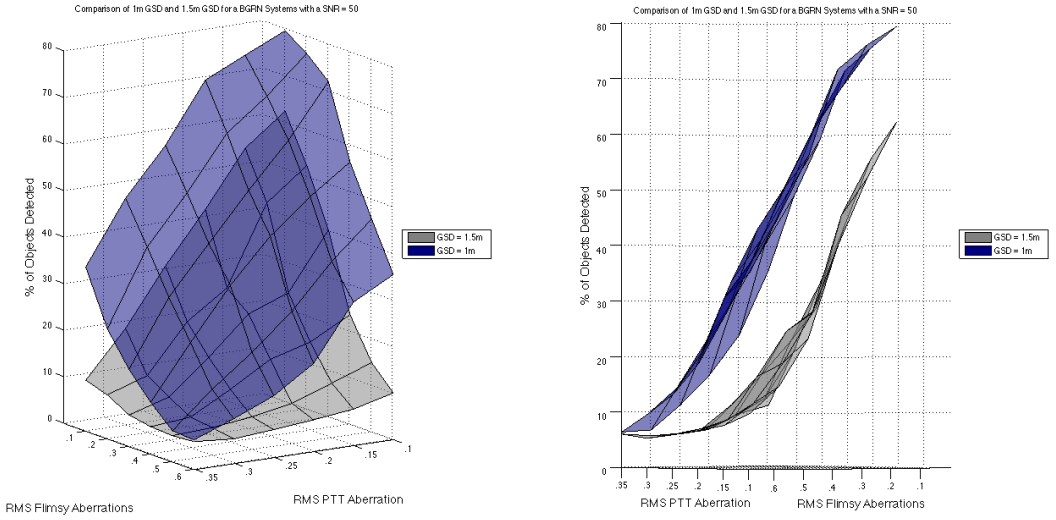

(a) Front view (b) Side view

Figure 5.22: BGRN Systems, with 1m and 1.5m GSD, and an SNR = 50

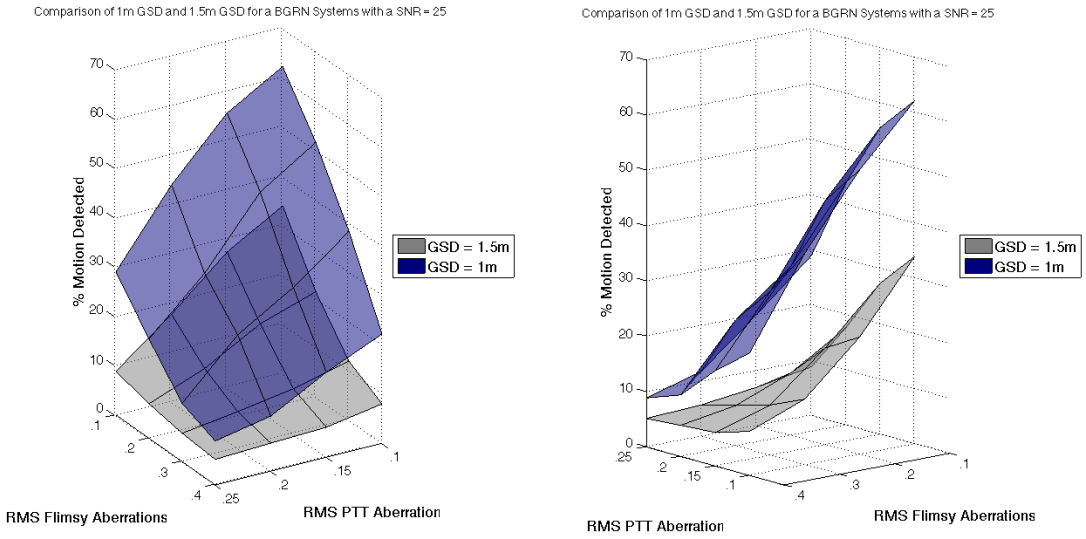

(a) Front view (b) Side view

Figure 5.23: BGRN Systems, with 1m and 1.5m GSD, and an SNR = 25

When the SNR is lowered to 50 (shown in Figure 5.25) the RN systems still outperform the BGRN at low and mid range aberration levels. As aberrations increase to high levels the BGRN systems perform best. These results are nearly identical to those shown in Section 5.3.2, where the main difference is the overall reduction in performance. Other subtler characteristics can be seen, for example in the larger difference in performance between the two systems - particularly at low aberration levels.

The final case where the SNR equals 25 (see Figure 5.26) shows that the BGRN systems always perform better than the BGR systems at low aberration levels (where the % of motion detection is useable). These results closely resemble those found in Section 5.3.2.

5.3.8 Comparison of 1.5m GSD, BGRN and BGR Systems

The results presented in this section will have some resemblance to those presented in Section 5.3.1. This scenario gives us the opportunity of understanding the importance of the NIR band. In Figure 5.27 the red surface represents the BGRN scenarios and the gray surface

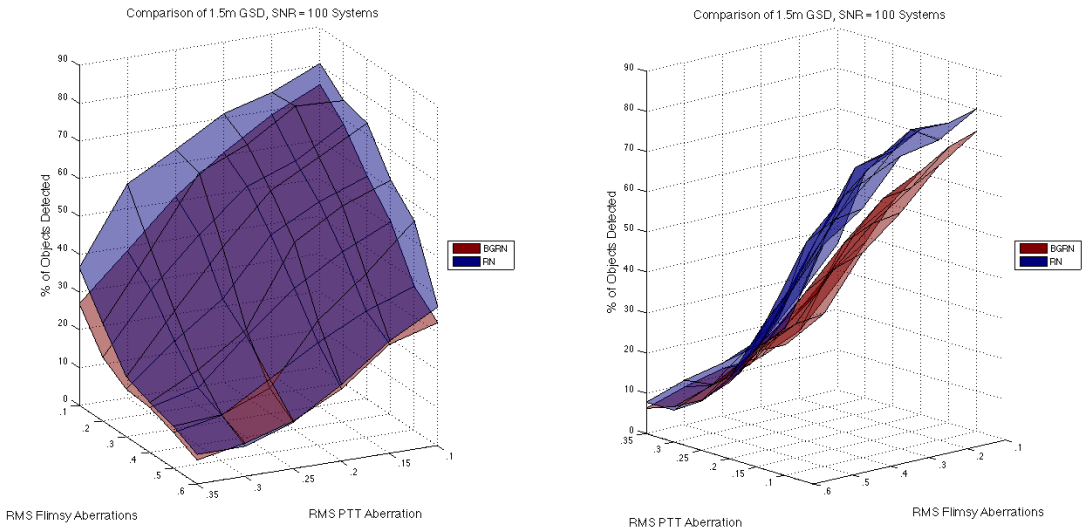

(a) Front view (b) Side view

Figure 5.24: BGRN and RN, SNR = 100, and GSD = 1.5m.

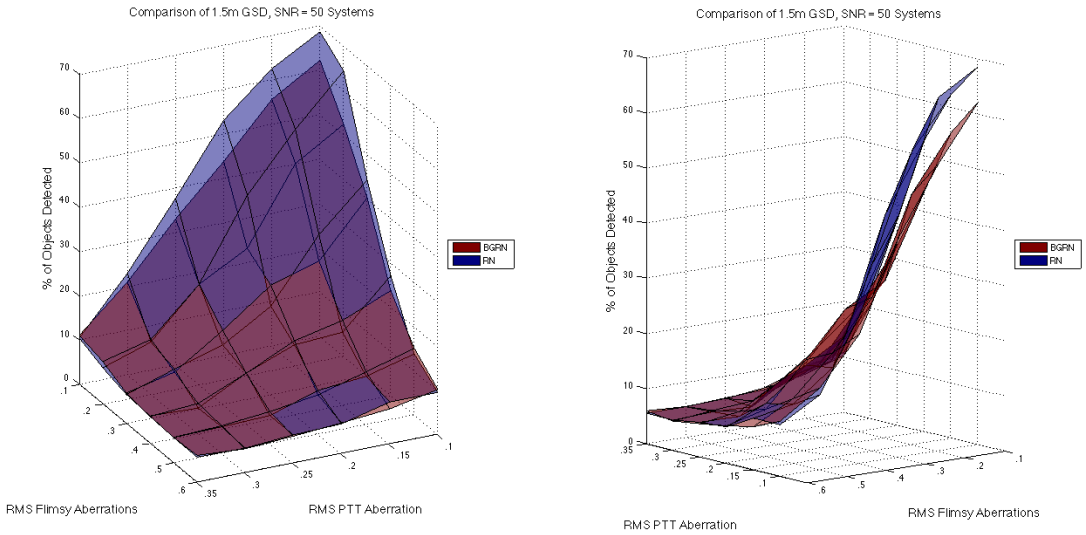

(a) Front view (b) Side view

Figure 5.25: BGRN and RN, SNR = 50, and GSD = 1.5m.

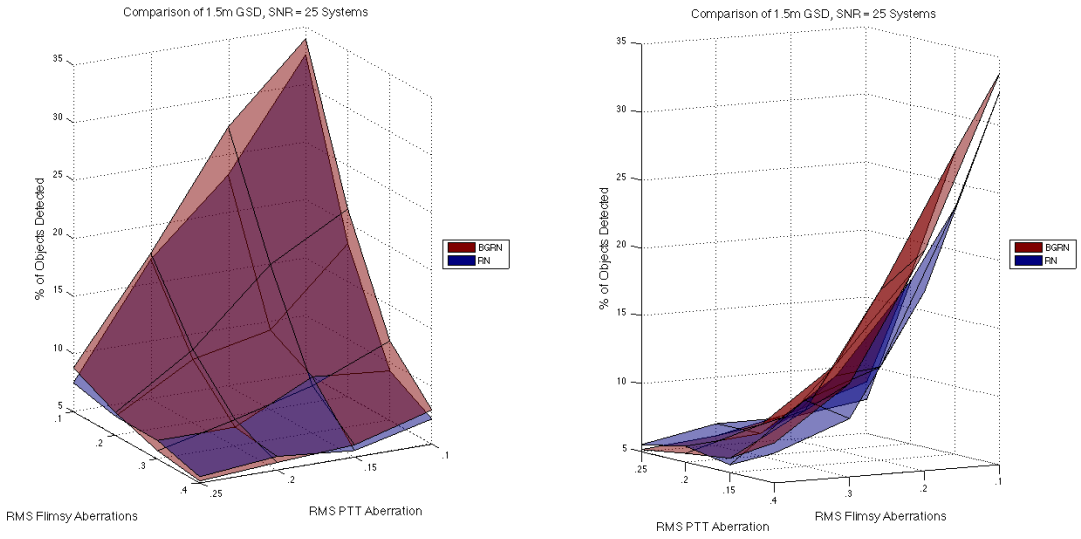

(a) Front view (b) Side view

Figure 5.26: BGRN and RN, SNR = 25, and GSD = 1.5m.

represents the BGR scenarios. We see that in this case adding the NIR band adds useful amounts of information to the data and the BGRN scenario always produces a higher % of detection than BGR.

As the SNR is lowered to 50 (see Figure 5.28) the amount of noise in the data increases. In this case we see that for low and mid-range aberrations the BGR has a higher % of objects detected. Adding the NIR band adds more noise than useful information to the data. This increase in noise confuses the motion detection algorithm and causes a decrease in performance.

When the SNR is lowered to 25 (see Figure 5.29) we see that the BGR system does much better than BGRN at low aberration levels. At higher levels of aberration the BGRN does outperform the BGR, however by this point the % motion detection is so low that this result is of little importance.

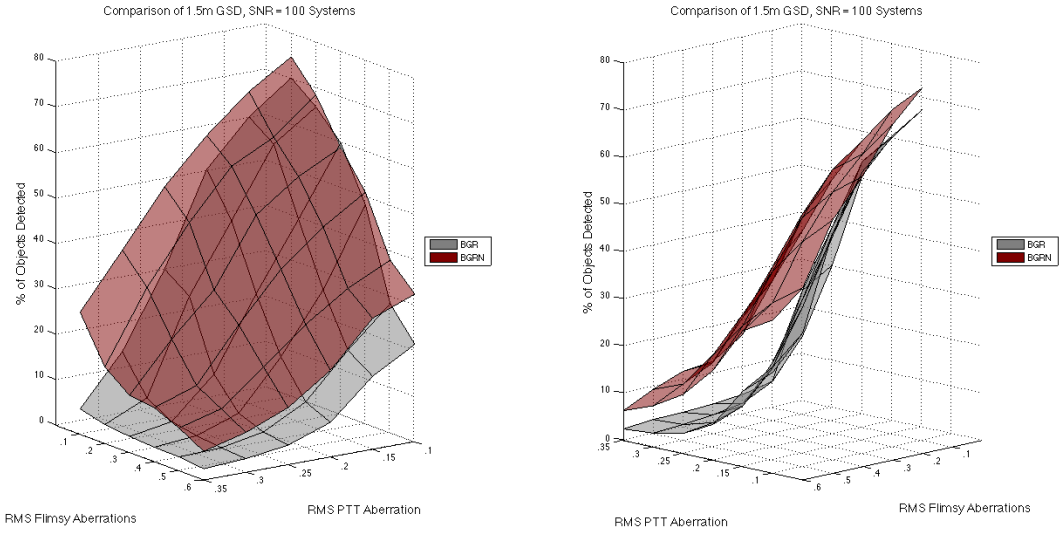

(a) Front view (b) Side view

Figure 5.27: BGRN and BGR, SNR = 100, and GSD = 1.5m.

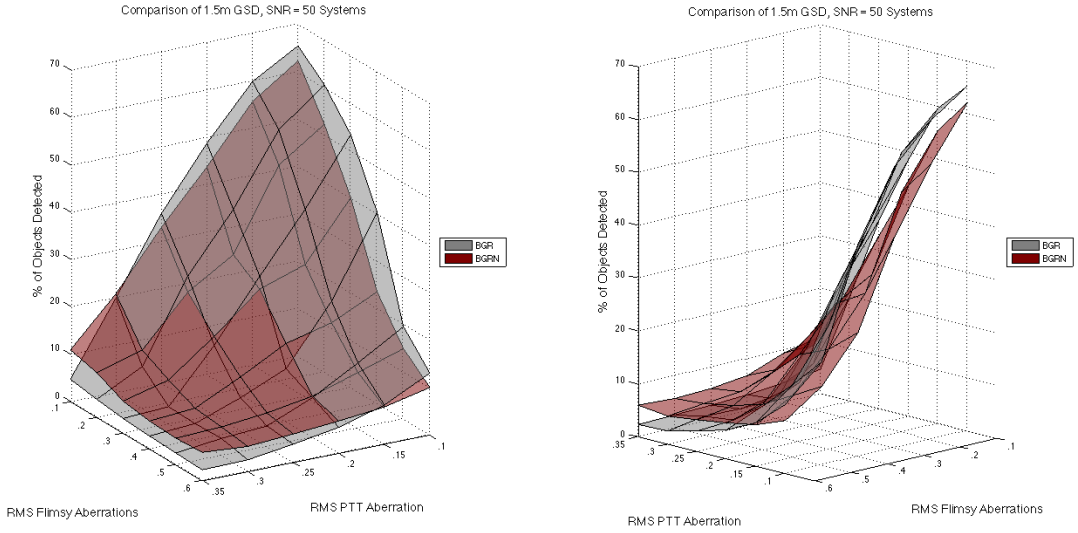

(a) Front view (b) Side view

Figure 5.28: BGRN and BGR, SNR = 50, and GSD = 1.5m.

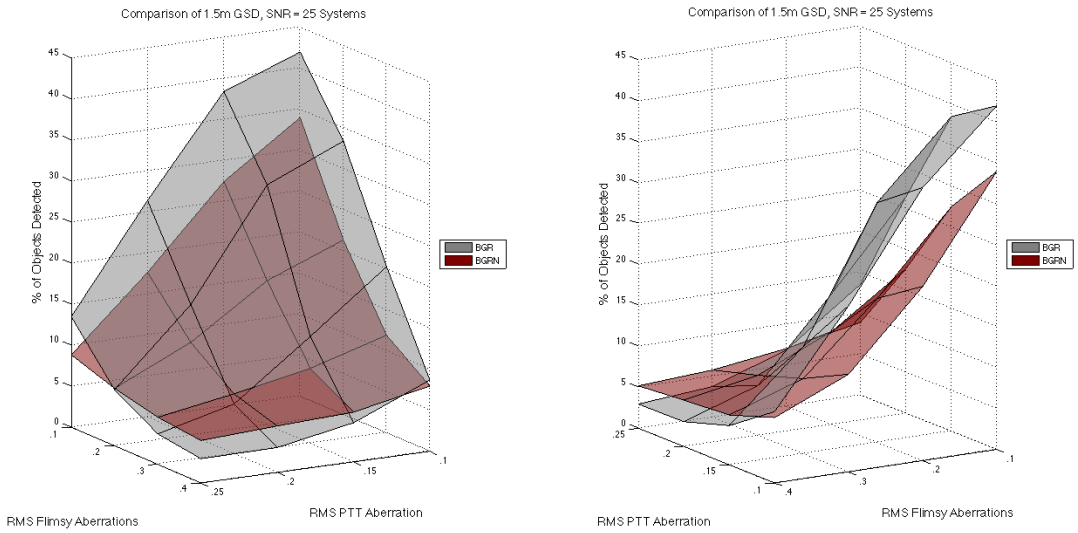

(a) Front view (b) Side view

Figure 5.29: BGRN and BGR, SNR = 25, and GSD = 1.5m.

5.3.9 Comparison of 1.5m GSD, BGRN, GRN, and RN Systems

This section will examine the behavior of BGRN, GRN, and RN systems at a GSD of 1.5m. We see in Figure 5.30 that the overall BGRN systems perform as expected with % of objects detected declining with the SNR and increased aberration levels. Notice that the SNR transition from 100 to 50 produces a smaller decline in system performance than the SNR transition from 50 to 25.

Figure 5.31 shows the GRN systems, notice that they appear to do slightly better than the BGRN. Here we find the overall performance to be slightly higher for all SNR tests. Looking at the SNR of 100 case we see that the values remain high after the first increase of aberration.

The 1.5m GSD RN systems, shown in Figure 5.32, do not perform nearly as well as the 1m GSD RN. At a SNR of 100 the RN system's performance drops off with the first increase in aberration. At an SNR of 50 the 1.5m GSD overall performance is lower than the 1m GSD, however it appears to drop off at a similar rate. The SNR of 25 case is much worse at 1.5m GSD than 1m GSD; at 1.5m GSD it detects only 30% of the motion.

These results are different than those in Section 5.3.5, which showed 1m GSD results, in that they show as expected a slightly lower overall performance and the difference between SNR 100 and SNR 50 is a bit larger.

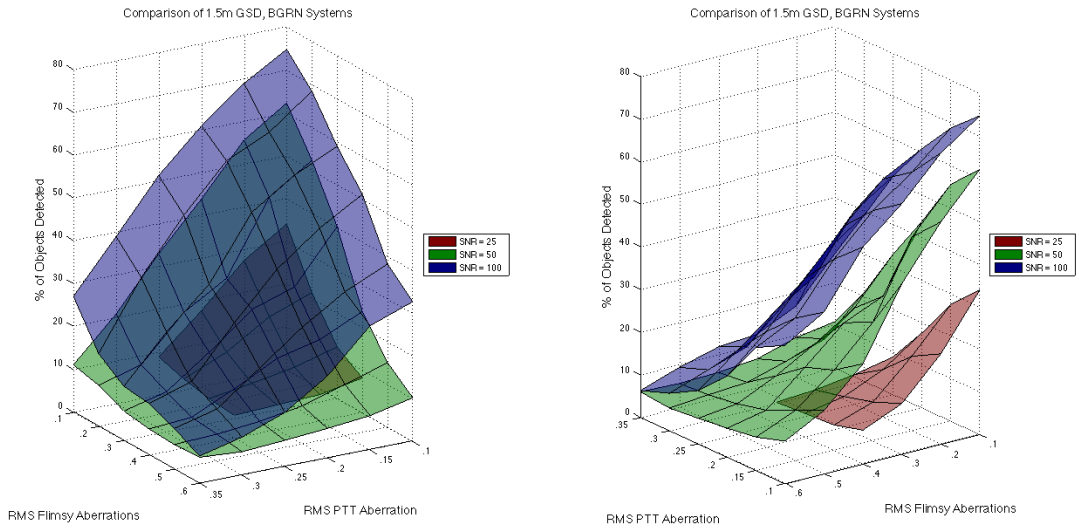

(a) Front view (b) Side view

Figure 5.30: BGRN Systems

5.3.10 Iso-Performance Surfaces Using the Motion Detection Data

Another interesting way of looking at the motion detection data is to make surface plots that show a performance boundary. The purpose of the plots presented in this section is to show boundaries that will produce results at the iso-performance level or better. For example, all experiments at 50% motion detection or better were collected. Surface plots were then made where the x, y, and z axis represented PTT aberrations, flimsy style aberrations, and SNR respectively. In words, there are three independent parameters (PTT, flimsy aberrations, and SNR) and the surface demarcates a boundary where all system designs within this boundary will detect motion at the designated level or better. Notice that there are blue dots within the boundary; these blue dots represent imaging scenarios that detect more motion than the value

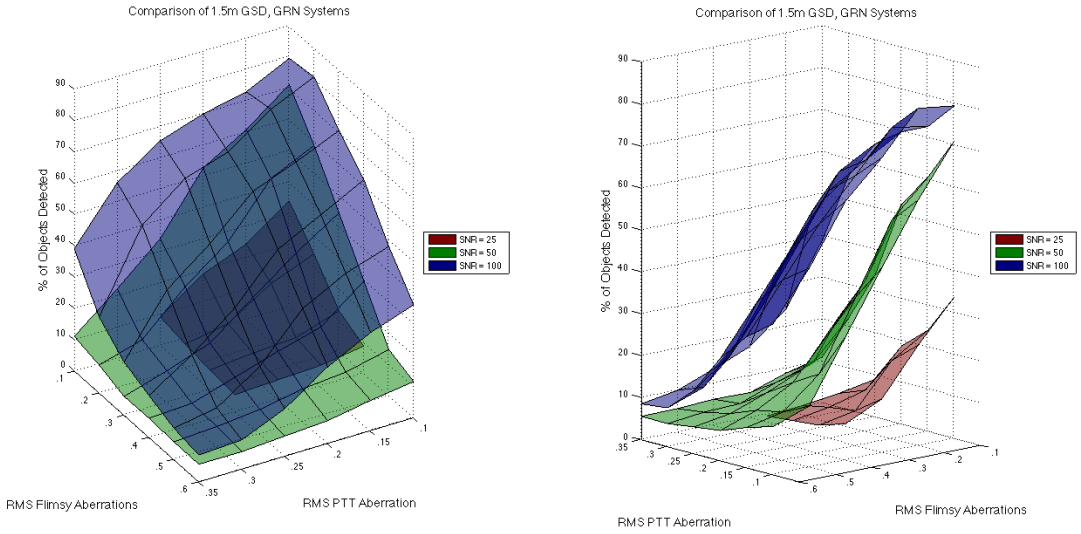

(a) Front view (b) Side view

Figure 5.31: GRN Systems

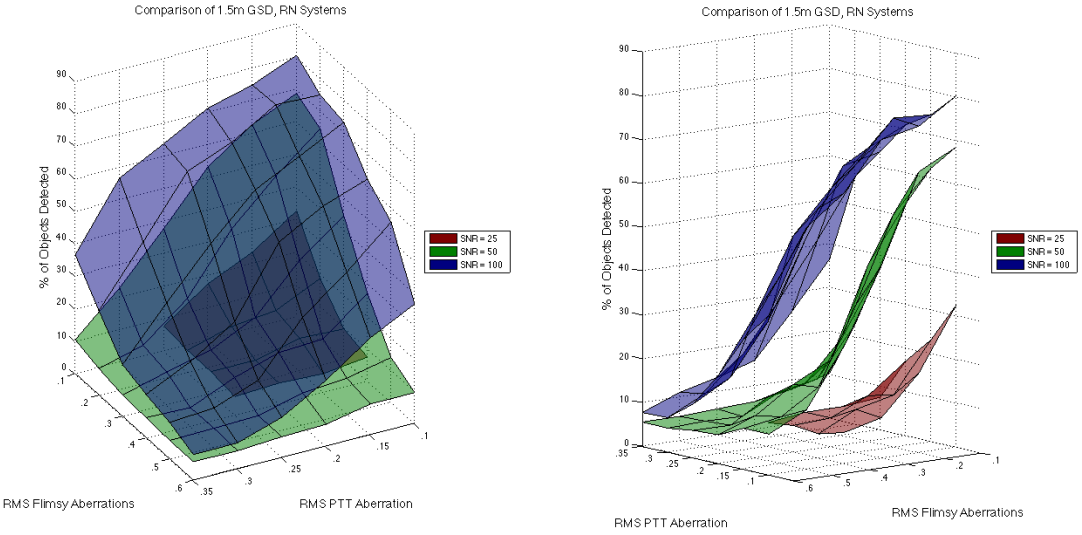

(a) Front view (b) Side view

Figure 5.32: RN Systems

on the boundary. They are also useful to the reader because they make it easier to determine the aberration and SNR levels on the boundary. This technique of displaying the data is very useful to system designers as it clearly shows regions where a given design will perform at a desired level or not.

Figure 5.33 shows two iso-performance surfaces for a BGRN system at 1m GSD. The red surface demarcates systems that will detect 75% of the motion or better. The green surface demarcates systems that will detect 50% of the motion or better. Notice that as SNR decreases from 100 to 25 the tolerable level of aberration goes down as well. At an SNR of 100 you can also see that the flimsy aberration level increases to .6 RMS OPD and still the system can detect 50% of the motion. On the other hand as the PTT aberration increases to .35 RMS OPD we see that the system will NOT detect 50% of the motion. We see this result again for the 75% motion detection surface; the flimsy aberrations increase all the way to .4 RMS OPD before the system is unable to detect 75% of the motion while the PTT aberrations can only increase to .2 RMS OPD. This shows that PTT aberrations have a much larger effect on system performance.

Another thing to note is that the highest level of detection for these systems is just over 80% and that the capability of these systems to detect motion falls apart very quickly. In the previous paragraph it was mentioned that systems with .1 flimsy and .1 to .2 PTT OPD can detect 75% of the motion or more; this is a 5% drop in motion detection. If we were to increase the PTT OPD error from .2 to .3 (which is a equally large jump in phase error) the % of motion detection drops 25%.

If we repeat the experiments described in the above paragraph, but this time drop the blue band we get the results displayed in Figure 5.34. If we compare Figure 5.34 and Figure 5.33 we see that both the 75% and 50% motion detection boundaries expand when the blue band is dropped (Figure 5.33 shows BGRN systems and Figure 5.34 shows GRN systems). This clearly shows that the blue band introduces more noise than useful information - for the experiments that are on the surface and but not necessary within the boundary.

The natural progression of this work is to reduce the number of bands again. Figure 5.35 shows the results if just the RN bands are used. What we find is that using only two bands did not help us and that the there must have been useful information in the green band. The other

interesting thing here is that there are a few data points that are lying separate from the 75% surface. If you observe Figure 5.20 you will see that this is merely a coincidence - there are several values that hover around 75% and these few happen to be over the boundary. What we can conclude from the RN experiments is that 3 bands is a good number to go with. The question then becomes is there a better configuration of bands that could be used. Perhaps BRN would be better than GRN or BGR.

In this research effort the only other 3 band configuration tested was BGR. Comparing GRN surfaces in Figure 5.34 to the BGR surfaces in Figure 5.36 you will notice that the BGR SNR 100 and SNR 50 cases do not perform as well the GRN. However, if you observe the SNR 25 scenario we see that the BGR cases outperform all other sensor configurations (operating at an SNR of 25) presented here.

Figure 5.37 shows difference in the behavior between the GRN and BGR scenarios. Here we can clearly see that the BGR scenario outperforms GRN at low SNR while at high SNR the GRN outperforms BGR. There results agree with those presented in Section 5.3.4.

The last Figure (Figure 5.38) compares all of the systems at 1m GSD that have 50% motion detection. This figure was added because some readers might find it easier to compare the systems on a single graph; this information was displayed previously in the 50% motion detection iso-surfaces in Figures 5.33, 5.34, 5.35, and 5.36. The bad thing about this plot is that there overlap between the different systems; for example, the SNR 25 case for BGRN, GRN, and RN overlap. The interesting thing about this plot is that we can see all the systems at once and we can quickly draw some conclusions between the BGR system and the other systems that include a NIR band. Notice that the SNR 25 BGR system has better performance than the other low SNR systems. The SNR 100 BGR systems have worse performance than the other systems and also notice that the SNR 50 BGR systems have about average performance compared to the other systems. Basically what we can conclude from this is that BGR systems perform better in low SNR scenarios, average in mid-level SNR scenarios, and worse in high SNR scenarios.

The results-data used to make the figures below can be found in Appendix A.

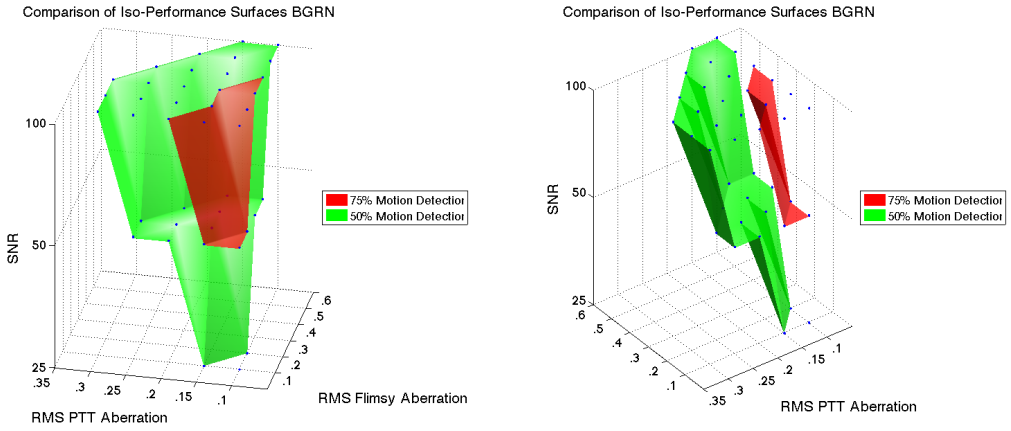

(a) Side view (b) Front view

Figure 5.33: Iso-performance surfaces BGRN at 1m GSD.

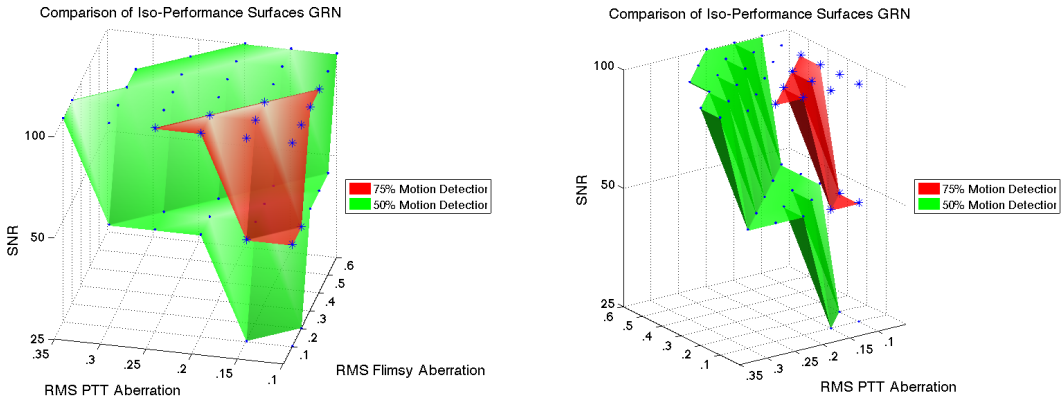

(a) Side view (b) Front view

Figure 5.34: Iso-performance surfaces GRN at 1m GSD.

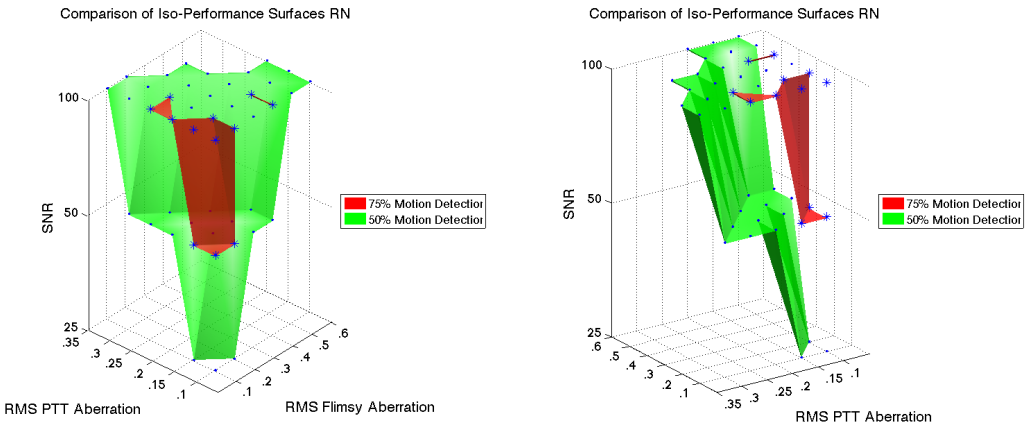

(a) Side view (b) Front view

Figure 5.35: Iso-performance surfaces RN at 1m GSD.

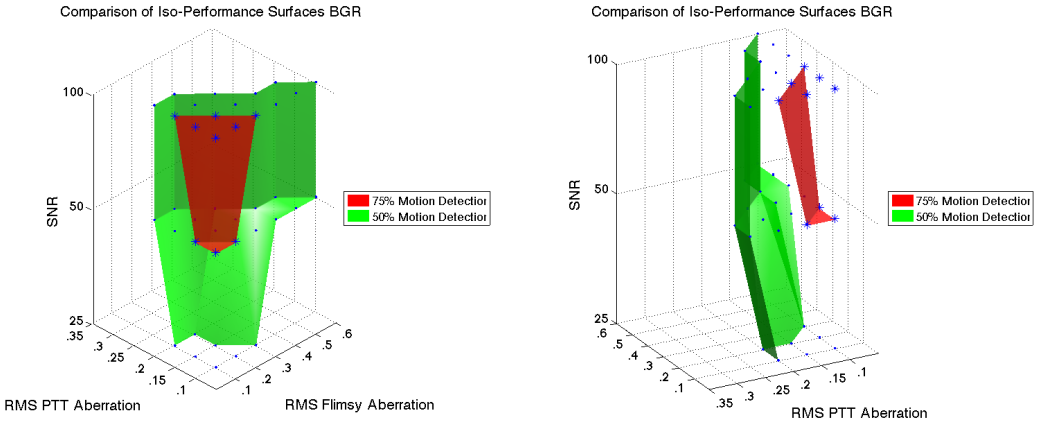

(a) Side view (b) Front view

Figure 5.36: Iso-performance surfaces BGR at 1m GSD.

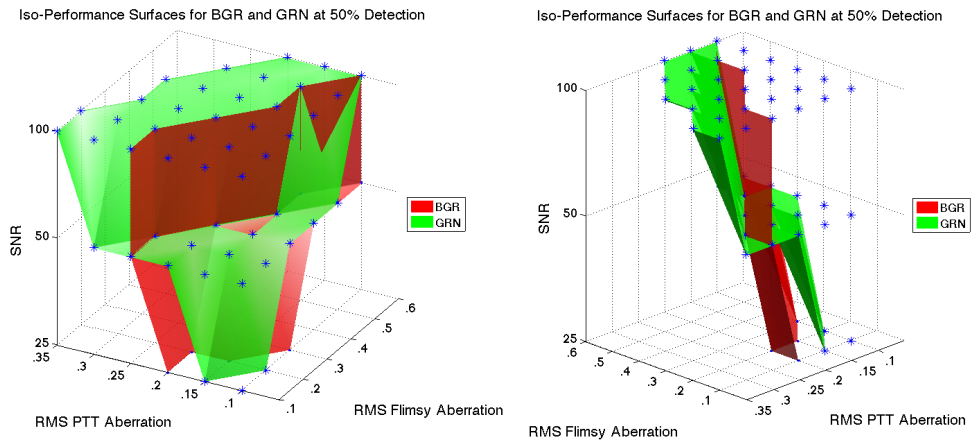

(a) Side view (b) Front view

Figure 5.37: Iso-performance surface comparison for BGR and GRN at 1m GSD and 50% motion detection.

5.4 Spatial Target Detection Results

Section 5.3 compared results using motion detection as an image utility metric. This section covers the results of a similar test of image utility that involves spatial target detection. Here it is demonstrated that using the correlation plane of a matched filter together with a PSR kernel on single bands will produce sound results. It is important to remember when viewing these results that they are scene and target dependent. In these examples a swept wing aircraft was used as the target; this target was quite small - taking up approximately 100 pixels. Had the target been larger then a stronger return would have been observed and the PSR value wouldn't drop off as steeply when the system became aberrated.

Figure 5.39 demonstrates how well the matched filter and PSR detection method work on the blue band with .1 PTT WFE and .1 flimsy WFE. The PSR value (shown in green) above the target is over 4 standard deviations (observe 4 blue lines) above the mean value (observe the red line), this means that it is higher than 99.994% of the PSR values. This shows the technique is producing very high PSR detection levels for a cluttered scene. This analysis was repeated for all experimental setups and in all cases the target PSR value was always 2

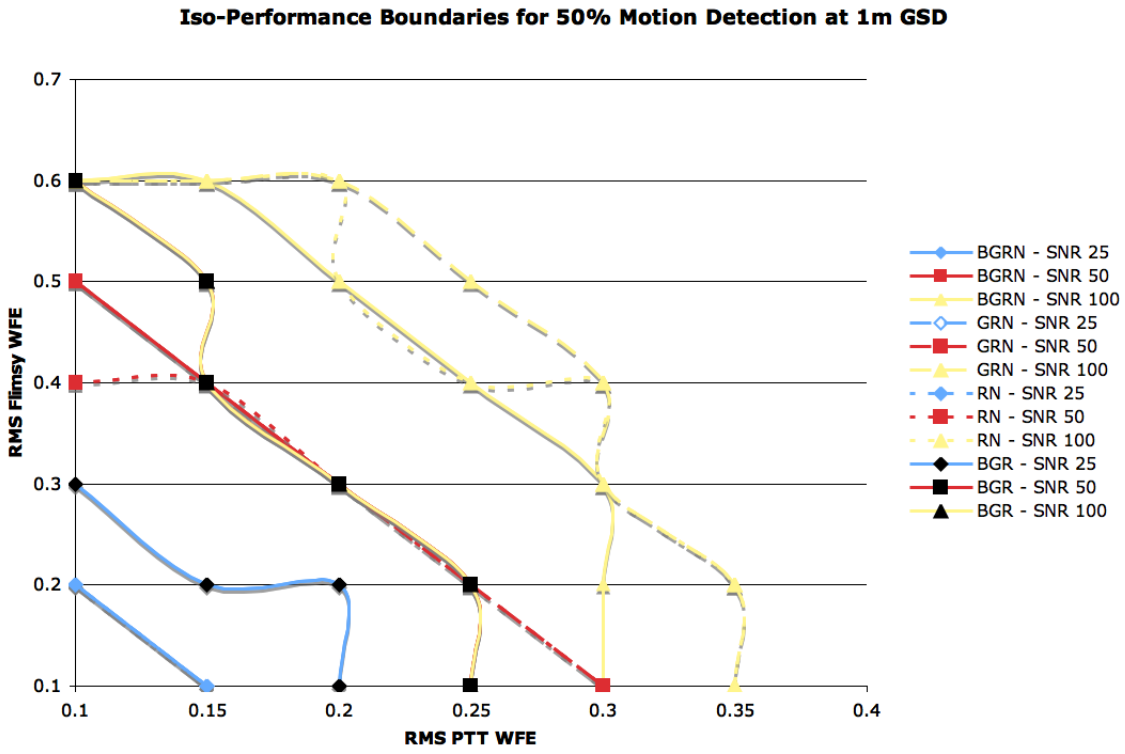

Figure 5.38: Iso-performance boundaries comparing all systems at 1m GSD and 50% motion detection.

standard deviations or more above the mean PSR value.

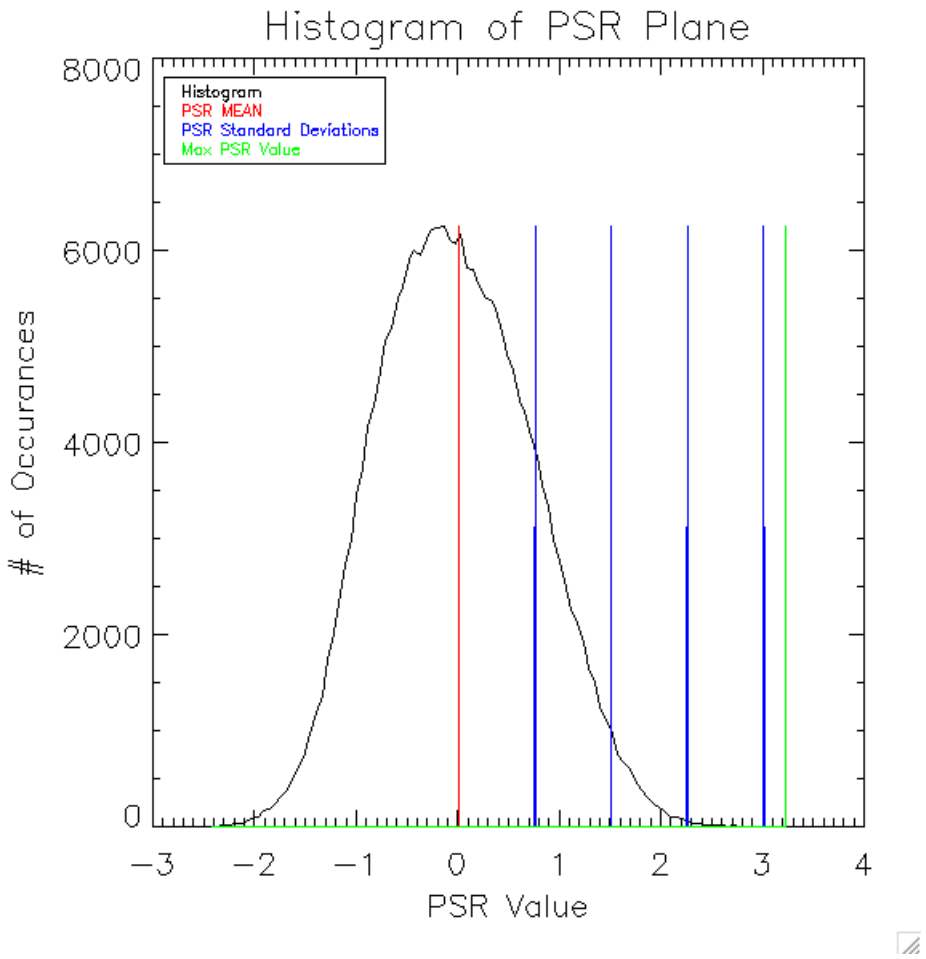

Figure 5.39: This plot shows the histogram of the PSR plane in black; the mean of the PSR plane shown in red; the 1^{st}, 2^{nd}, 3^{rd}, and 4^{th} standard deviations shown in blue; and the PSR value above the target shown in green. What we gather from this plot is that the PSR target value is over 4 standard deviations above the mean of the PSR plane - this is a very high level of detection as over 99.994% of the PSR values are lower than the target PSR value.

Figure 5.40 is a plot of the results generated from the blue band. Notice that the PSR drops off very steeply as aberration levels increase. Remember that the blue band sharpness deteriorates quickly as aberration levels increase, this causes a rapid decrease in spatial target detection performance. As the spectral wavelength becomes longer and the effect of aber-

rations is less we see in Figure 5.41 that the surface inflates slightly. Figures 5.42 and 5.43 represent the results from the red and NIR bands. With each increase in wavelength there is an increase in overall performance (compare the Blue band results with the NIR). This is an interesting because one might also expect a decrease in performance due to a decrease in cutoff frequency as the spectral wavelength increases. Even in the low aberration scenarios there were no observed trends that would indicate this. A reason for this could be different object-background contrast levels at the different spectral bands.

The following figures show the results for a system that has an SNR of 100. The initial investigation of this experiment showed that this technique was not sensitive to noise in any way that was informative. The data used to make the figures below is presented in Appendix B. There is also some data from experiments conducted with SNR values of 25 and 50; the data shows little sensitivity to noise.

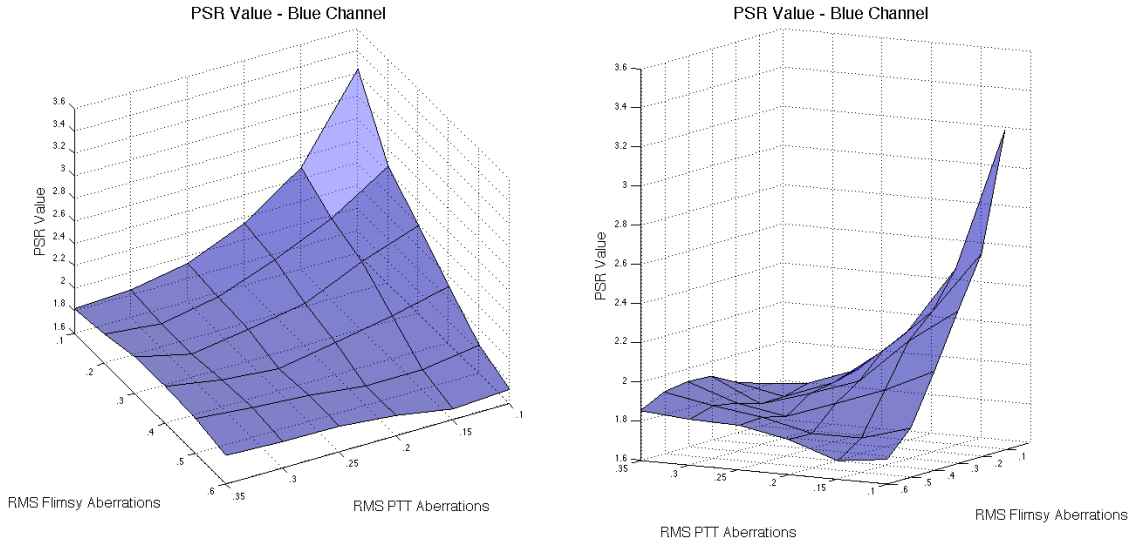

(a) Front view (b) Side view

Figure 5.40: PSR Blue

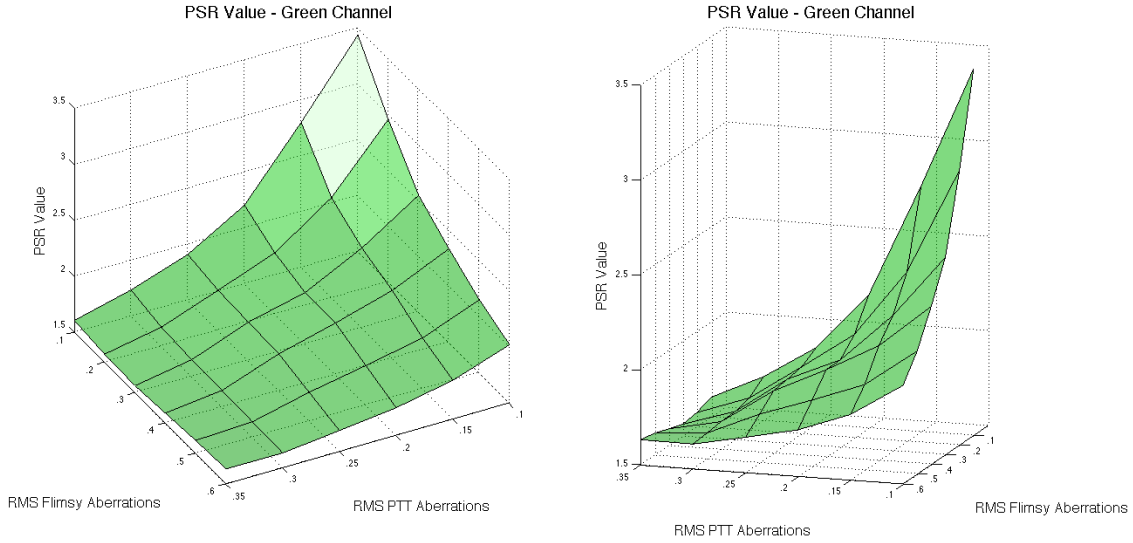

(a) Front view (b) Side view

Figure 5.41: PSR Green

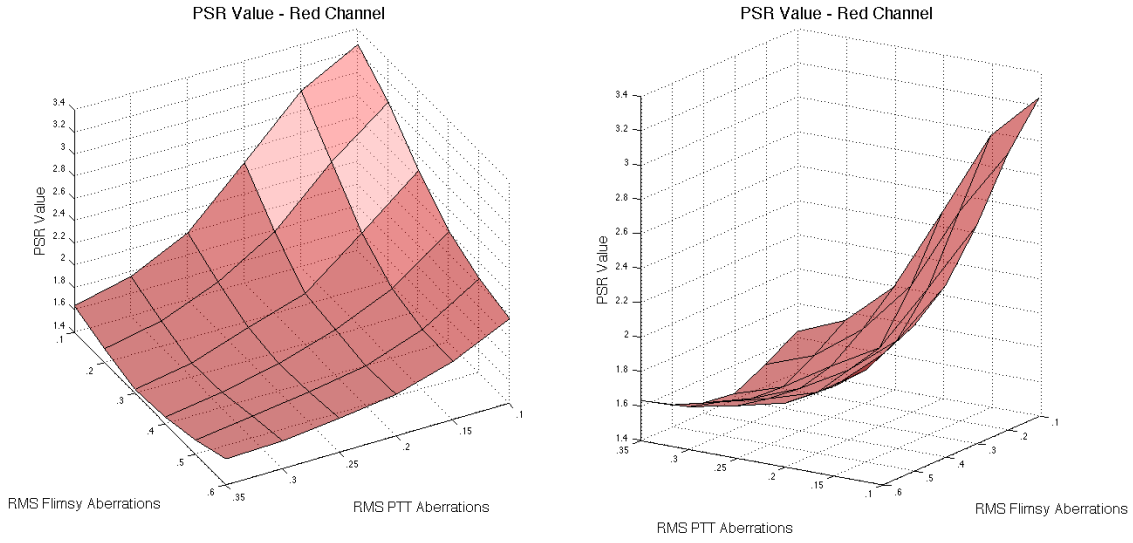

(a) Front view (b) Side view

Figure 5.42: PSR Red

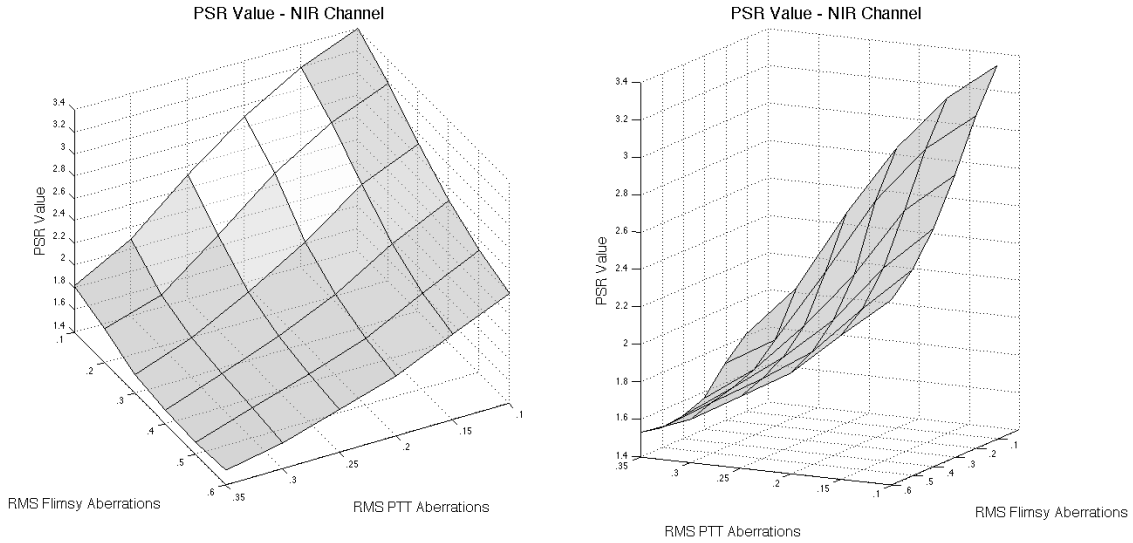

(a) Front view (b) Side view

Figure 5.43: PSR NIR

5.5 GIQE Results

The GIQE technique is the only conventional image quality/utility assessment technique presented in this document. It is also the most popular technique available. Being heavily reliant on a well behaved MTF, it was hypothesized that the GIQE would not produce accurate or consistent results because of the poorly behaved MTF. An attempt was made to find the noise gain term in the GIQE but because of the poorly behaved MTF an appropriate value was not found(refer to Section 4.8.1). The GIQE did function in some capacity, however to truly understand how well it functioned we would need an analyst to help with the determination of accurate NIIRS values for these systems.

As aberration levels increased the NIIRS estimate usually decreased. This is clear in Figure 5.44. However, some of the other figures show some exceptions; in Figures such as Figure 5.45 and Figure 5.46 we see that once PTT aberrations increased to the highest levels (.35 RMS OPD) the NIIRS estimates did not decrease with increased levels of Flimsy aberration. This is likely a problem with the GIQE because the other tests performed in this

document consistently show decreases in performance as aberration levels increase.

While there are similarities between bands the surfaces do have somewhat different structure than those shown in Section 5.4 and Section 5.3. Looking at the four surfaces notice that the effect of the flimsy aberrations are not nearly as great as the PTT aberrations. Also keep in mind that the flimsy aberration levels go up to nearly twice the level of PTT. The GIQE is not very sensitive to flimsy style aberrations. A specific example can be seen in the NIR band data (Figure 5.47) looking at .1 RMS PTT OPD systems with flimsy aberrations ranging from .1 to .6 RMS OPD. Notice that over this range the NIIRS estimate decreases by .2 which on the NIIRS is considered a just noticeable difference Leachtenauer et al. (1997). However, if we look at image created by these two scenarios we can easily observe a large difference between the sharpness and quality of the images.

Despite these problems there are some promising attributes. Upon closer inspection it is possible to see that the surfaces inflated as the spectral wavelength increased. This was a behavior also observed in Section 5.4; it is caused by the decrease in the apparent phase error of the optics as the spectral wavelength increases. This decrease in phase error leads to an increase in image sharpness.

The experiments done here did not include a noise term in the GIQE. It was impossible to include the last term of Eq. 4.22 because the noise gain could not be determined; therefore all results presented here do not include this term.

Since the GIQE assumes a well behaved MTF these results should be interpreted cautiously. To have absolute certainty of what was reported it would be necessary to have a trained analyst determine the actual NIIRS value for an image generated by each system.

The results-data used to make the figures below can be found in Appendix C.

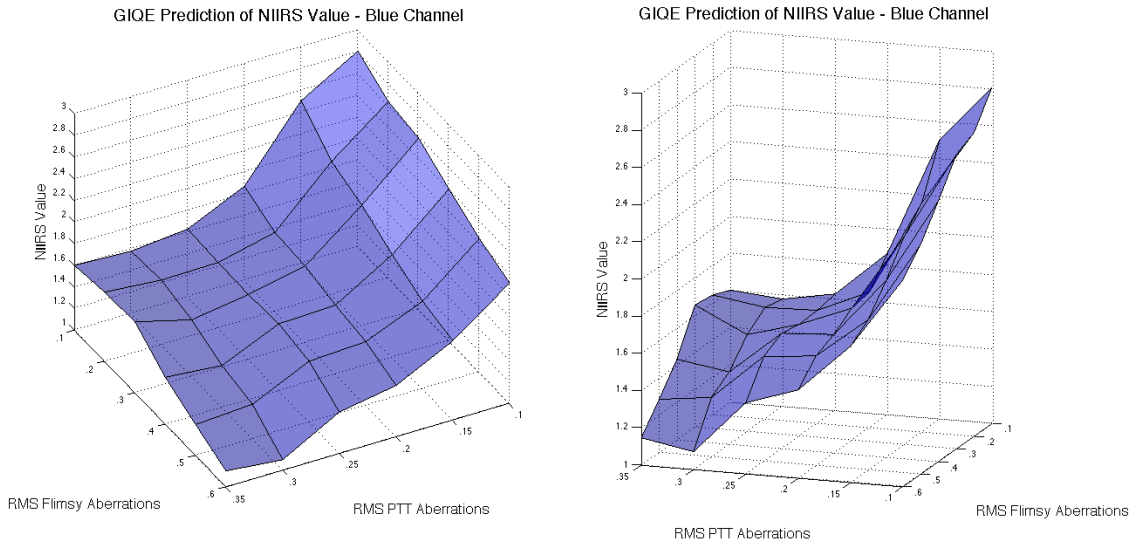

(a) Front view (b) Side view

Figure 5.44: GIQE Blue

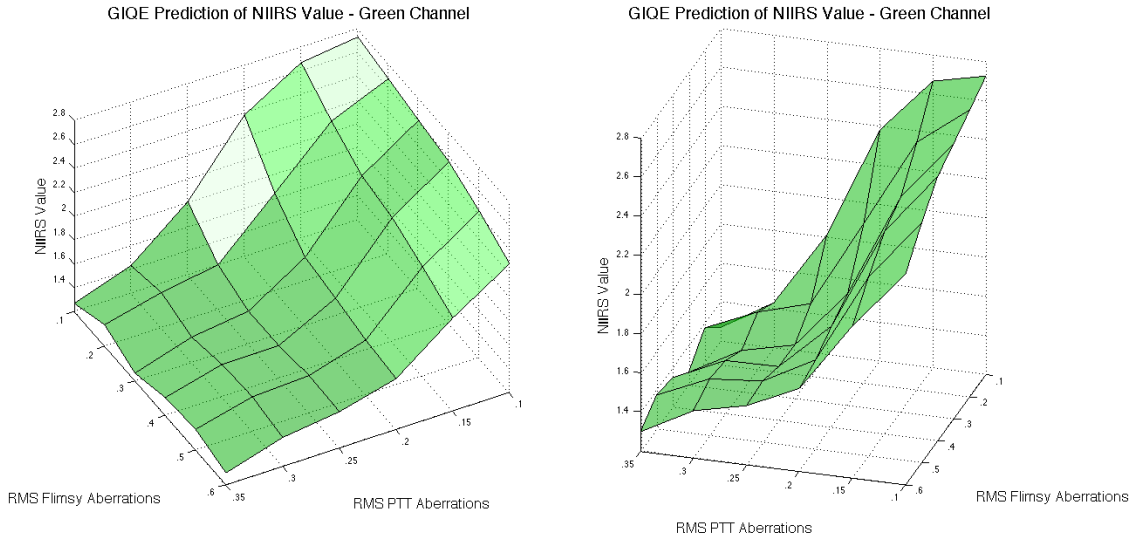

(a) Front view (b) Side view

Figure 5.45: GIQE Green

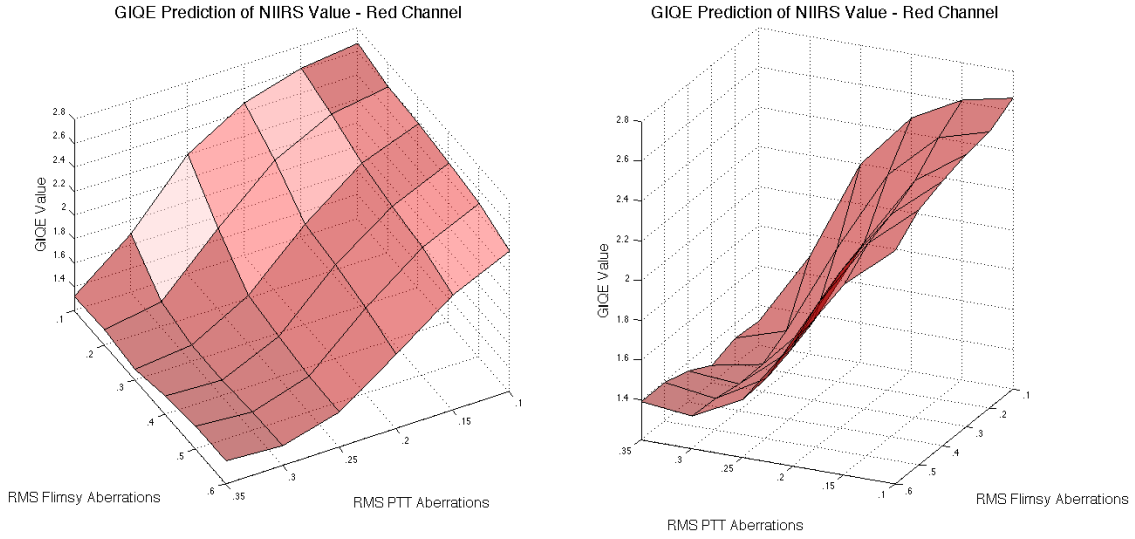

(a) Front view (b) Side view

Figure 5.46: GIQE Red

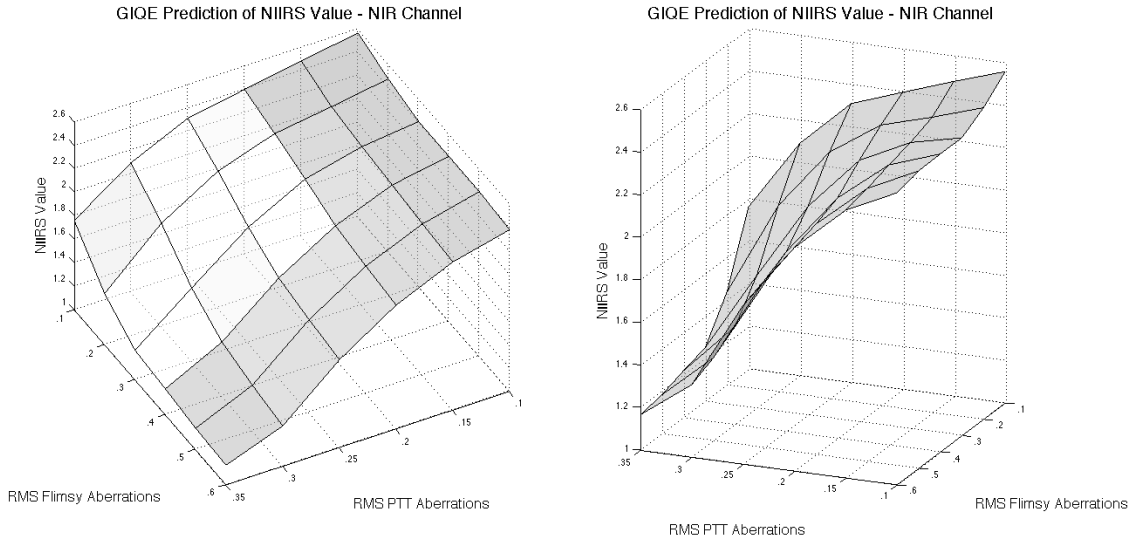

(a) Front view (b) Side view

Figure 5.47: GIQE NIR

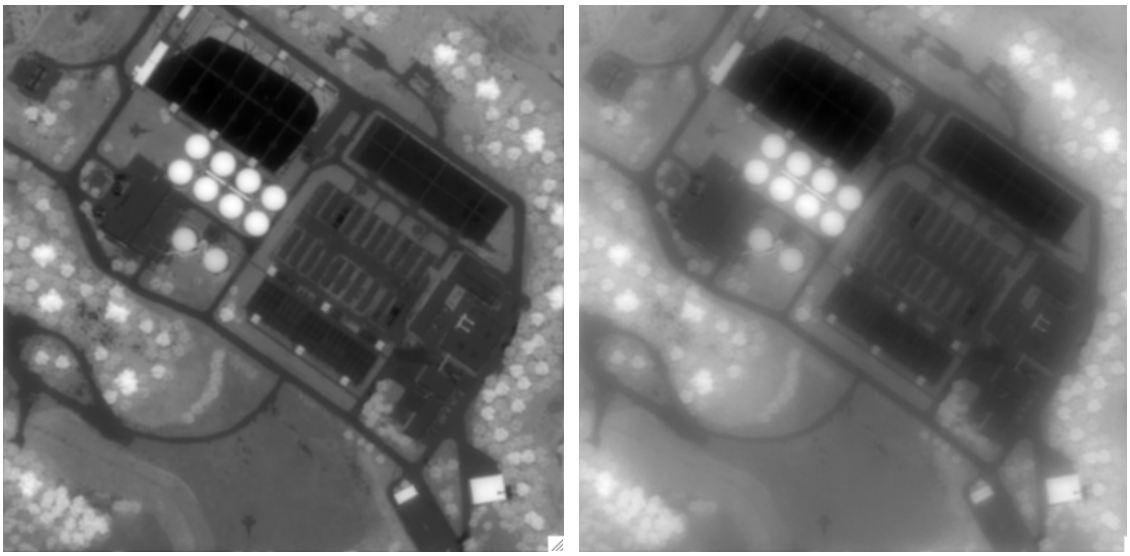

(a) .1 RMS PTT OPD and .1 RMS Flimsy OPD. (b) .1 RMS PTT OPD and .6 RMS Flimsy OPD.

Figure 5.48: NIR bands from systems with different amounts of flimsy aberration.

Chapter 6

Conclusions

The primary goal of this work was to build a flexible imaging modeling tool that could process synthetic data to look like imagery collected from a segmented aperture space telescope at a geosynchronous orbit. The model was successfully built and has full flexibility of reference wavelength, PTT aberration, flimsy aberration, aperture geometry, input data, GSD, detector sampling, spectral resolution, quantum efficiency, focal length, optical transmission, various detector noise effects, altitude, and jitter. It also has a mode where some of these parameters can be overridden and GSD and SNR can be specified by the user.

Other goals that were not included in tests were to model nano-laminant mirror aberrations using fractal Brownian motion. This technique produced mirror segments that appeared visually similar to the interferogram of the mirror, however it is unknown if they are mathematically similar. It is left undetermined if the aberrations observed in the interferogram are in fact fractals.

6.1 Experimental Conclusions

One of the main goals of this work was to demonstrate that there is more than one way of assessing an imaging systems potential. The word "potential" was used here because it is fairly general and traditionally these remote sensing systems are rated using the NIIRS Scale, which is an image interpretability scale. We felt that this metric was lacking - particularly

for today's multispectral systems which have video capability. These systems aren't going to be built for analysts who will manually comb over every image; it is much more likely that a computer will do the majority of the work; therefore, looking at this problem from an image utility standpoint made more sense.

6.1.1 Motion Detection Conclusions

Initially, we were interested in seeing if any of these techniques worked. The motion detection experiment was perhaps the most promising. This experiment revealed all the things we knew would happen, which allowed us to build confidence in what the results were telling us and then look more closely to find some of the more interesting and subtle behavior of these systems.

Upon first viewing these results we could see that if either the GSD or aberrations increased or the SNR decreased there would be a decrease in performance. These were expected results because changing these parameters would naturally lead to a decrease in the amount of information in the data.

The first surprising result was that the flimsy aberrations did not have the same proportional negative effect that the piston, tip, and tilt did. Looking at any of the result plots from the motion detection algorithm we can see that a ΔWFE_{flimsy} = .1 would produce approximately the same change as a $\Delta WFE_{PTT} = .05$. This is a particularly interesting result because if we wanted to spend money on reducing the mirror aberrations it makes much more sense to invest in better PTT alignment.

Another thing that we suspected would impact performance was the band selection. We knew that the NIR band would sustain a higher level of aberration than the other bands, and therefore any configuration that contained the NIR band would perform well in highly aberrated scenarios. What wasn't known was how the systems would perform at low levels of aberration. This was answered with the comparison of BGR and GRN (Section 5.3.4). This is perhaps the best example to show the complexity of these systems when band selections, aberrations, and SNR are taken into account.

In Figure 5.15, when the SNR is very high and there are little to no aberrations we see that the BGR has a better performance than GRN. In some ways this is an expected results

because the blue MTF will pass more information than the NIR. The catch here is that the objects in the blue band must have enough contrast against the background so that it adds more information to the data than the NIR band does. Once aberration levels increase the blue band is the first band to experience the effects of the aberrations, while GRN bands remain relatively unaltered. This causes the GRN systems to outperform the BGR.

Things get more interesting though when the SNR is lowered to 50. At this level the BGR systems achieve the best performance at low aberration levels. Once the aberration levels increase to mid range the GRN systems don't experience the same rate of decline in performance as the BGR systems do because they have the NIR band which remains fairly sharp. From mid to high aberration levels the GRN systems outperform the BGR.

Once the SNR is lowered even further to 25 the BGR systems consistently and significantly outperform the GRN systems. In this case, we have a blue band that is blurry but has a large amount of contrast between the moving objects and the background, while the NIR band is relatively sharper but has a relatively smaller amount of contrast between the moving objects and the background. Another way of thinking about this is to realize that the NIR band is introducing more noise than useful information when compared to the amount of noise and information being introduced by the blue band. This shows us that in low SNR scenarios it is important to select bands that will have a large amount of contrast even if they will be blurred by the optics.

6.1.2 Spatial Target Detection Test Conclusions

This test is heavily dependent on the shape and size of the object being searched for. In our case we used a small swept wing fighter. These results show some of the basic features that were observed in the motion detection results (in Section 6.1.1). Here we have to observe the effects on individual bands that have a high SNR. The most general result is that the flimsy aberrations do not have the same substantial effect on performance as the PTT.

The next thing that can be observed as we increase in wavelength from blue to NIR is that the performance increases with wavelength. As the blue band's aberration levels increase we see that the performance quickly drops away. However if we look at the NIR band we see that performance doesn't drop off as quickly. This is the result of the reduced optical phase

error at the larger wavelengths.

6.1.3 GIQE Conclusions

The GIQE produced some interesting results. Remember that the GIQE does not take full account of the effects of the complex MTFs we have in this work. The previous sections have shown that the flimsy aberrations do cause a decrease in performance that is about half of what PTT aberration level would produce. The GIQE tells us that the flimsy optics have even less of an effect on performance than the other tests show. This demonstrates how the GIQE may not be as sensitive a test for these types of systems.

6.2 Limitations

There are quite a few limitations for this work. Most of the limitations are related to the computational time needed to process data and complete tests.

For the system model the largest limitation is the processing time and memory requirements. The CCDs available now have many mega pixels producing 16-bit data. Accurately modeling the large images that would come from those systems is not possible on the computers used in this research.

The motion detection experiments had some limitations. The spectral resolution of the data was very poor (bandwidths of 100nm or more) and because of this the spectral effects of the MTF could have been modeled better. However, if higher spectral resolution data were available the amount of storage space needed would have been so large that conventional hard drives would not have had enough room. In addition to this the processing time would have also increased and the computers that were available would not have been fast enough.

The primary limitation for the spatial target detection experiment was that it didn't reveal the deleterious effects of noise. The GIQE also had this problem in addition to not fully accounting for the MTF effects.

6.3 Future Work

There is a great deal of future work that could be done. Other optical effects cause by the secondary and tertiary mirrors could be tested. The focusing effects of the detector's position on the focal plane array could be modeled. All of these experiments were carried out from a geostationary orbit looking straight at the equator. These experiments could be repeated using oblique imagery. The sensor's altitude could be changed. This would call for other motion effects such as smear to be incorporated into the model. The motion detection experiment could be repeated using different integration times and frame refresh rates. The objects also could have been tested against a different background such as a desert scene.

6.4 Closing Statement

What was done in this research should be taken with the proverbial grain of salt. The experiments carried out were not of the highest fidelity and there were certainly sources of error. What this work *did* do was demonstrate that it is possible to look at these systems from a different perspective than what is traditionally done. We need to understand how these system will perform doing the tasks they are built for - the system modeling approach is the best way of doing this. What we ultimately showed was that these systems are not simple and that understanding their performance can't be determined from system parameters like GSD and SNR. Additional tests must be done; preferably ones that are similar to the tasks the system will be assigned to do in the real world.

Appendix A

Motion Detection Data

N.B. All experimental results reported in this document were carried out with a noise to signal power ratio of .3 (variable within Wiener-Helstrom Filter), PTT RMS WFE knowledge of .5 [waves], and flimsy RMS WFE knowledge of .5 [waves].

GSD [m]	SNR	PTT WFE [waves]	Flimsy WFE [waves]	% M.D. BGR	% M.D. BGRN	% M.D. GRN	% M.D. RN
1	25	0.1	0.1	65.4408692	61.98899371	66.95245518	62.55319149
1	25	0.1	0.2	65.77561766	51.37090632	53.59477124	52.88239816
1	25	0.1	0.3	55.01156515	38.11881188	37.31911653	34.66819222
1	25	0.1	0.4	45.69561875	22.08682407	20.79207921	19.84006093
1	25	0.15	0.1	63.14115308	55.42307692	56.55172414	54.93395493
1	25	0.15	0.2	60.33938437	44.16475973	43.48819497	41.27951257
1	25	0.15	0.3	49.01960784	29.5887281	27.41812643	23.45773039
1	25	0.15	0.4	33.35872049	17.17440975	16.03198781	13.17593298
1	25	0.2	0.1	56.81995323	43.68783474	42.80274181	42.63920671
1	25	0.2	0.2	51.37931034	30.54074638	27.64661081	26.19954303
1	25	0.2	0.3	40.92295957	22.81035796	19.07844631	16.18431074
1	25	0.2	0.4	21.78217822	11.1195735	10.24371668	9.748667174
1	25	0.25	0.1	48.38833461	28.90327494	26.12338157	23.03884235
1	25	0.25	0.2	38.23305407	20.06854532	17.40289414	14.47067784
1	25	0.25	0.3	21.21096725	11.76694593	10.81492765	9.253617669
1	25	0.25	0.4	8.834729627	8.872810358	8.872810358	8.073115004
1	50	0.1	0.1	80.40657439	79.27287923	79.09768212	78.55980472
1	50	0.1	0.2	78.76106195	76.02040816	75.04222973	78.57142857
1	50	0.1	0.3	74.33516252	71.69811321	72.43772969	71.34693878
1	50	0.1	0.4	69.45126945	56.11001965	56.53518948	57.81860829
1	50	0.1	0.5	62.09710322	45.56913675	50.01913509	48.13404417
1	50	0.1	0.6	53.05019305	35.33891851	33.85376999	29.5887281
1	50	0.15	0.1	77.79171895	75.34129693	75.38525614	76.06490872
1	50	0.15	0.2	74.22723475	68.2160804	70.0122399	73.14168378
1	50	0.15	0.3	67.34104046	60.41584935	61.04100946	63.28963051
1	50	0.15	0.4	62.65772871	50	51.87739464	50.76394194
1	50	0.15	0.5	54.53143078	37.79648049	39.77011494	36.84210526
1	50	0.15	0.6	36.59558264	30.73115004	28.44630617	25.51408987
1	50	0.2	0.1	72.06375839	71.28712871	73.18087318	73.10996564

Figure A.1: Motion detection data.

GSD [m]	SNR	PTT WFE [waves]	Flimsy WFE [waves]	% M.D. BGR	% M.D. BGRN	% M.D. GRN	% M.D. RN
1	50	0.2	0.2	68.27640361	61.59045726	62.7824019	67.28273692
1	50	0.2	0.3	58.97336936	50.95932464	53.93215112	55.24100995
1	50	0.2	0.4	46.68697639	42.84082254	44.85910129	40.20657995
1	50	0.2	0.5	29.96953542	28.40822544	28.86519421	25.17136329
1	50	0.2	0.6	17.44097487	18.88804265	19.45925362	17.25057121
1	50	0.25	0.1	65.3907496	58.61122009	61.46283917	61.22047244
1	50	0.25	0.2	56.61820964	50.07686395	55.29685681	52.53115265
1	50	0.25	0.3	36.5575019	40.89870526	44.49120122	40.63214014
1	50	0.25	0.4	21.02056359	33.58720487	35.22467631	29.96953542
1	50	0.25	0.5	8.682406702	20.9063214	19.57349581	14.66108149
1	50	0.25	0.6	5.788271135	13.25209444	14.39451637	12.56664128
1	50	0.3	0.1	44.93476592	48.58454476	51.70563434	51.51631478
1	50	0.3	0.2	26.88499619	39.79436405	43.15225708	38.59984698
1	50	0.3	0.3	10.31987814	30.65498858	31.4166032	25.85681645
1	50	0.3	0.4	5.369383092	22.6199543	21.66793602	16.14623001
1	50	0.3	0.5	5.178979436	14.28027418	15.30845392	10.31987814
1	50	0.3	0.6	3.884234577	9.634424981	9.520182788	7.311500381
1	50	0.35	0.1	15.19421173	35.14851485	35.03427266	32.59710586
1	50	0.35	0.2	11.42421935	23.57197258	26.12338157	23.95277989
1	50	0.35	0.3	8.492003046	16.52703732	16.07006855	14.47067784
1	50	0.35	0.4	6.207159177	11.15765423	9.139375476	8.073115004
1	50	0.35	0.5	6.28332064	6.702208682	7.730388423	6.892612338
1	50	0.35	0.6	3.846153846	6.397562833	7.349581112	6.397562833
1	100	0.1	0.1	81.90997055	80.11409943	80.23255814	79.88386562
1	100	0.1	0.2	79.44716897	81.20522545	79.10807553	76.55662349
1	100	0.1	0.3	76.3803681	77.57903494	76.10949813	74.10341952
1	100	0.1	0.4	74.29401993	77.45640153	76.56710139	76.62389735
1	100	0.1	0.5	66.62703131	68.98759504	68.455551	72.32854864
1	100	0.1	0.6	52.83165244	62.27005871	62.43450222	64.15019763

Figure A.2: Motion detection data continued.

GSD [m]	SNR	PTT WFE [waves]	Flimsy WFE [waves]	% M.D. BGR	% M.D. BGRN	% M.D. GRN	% M.D. RN
1	100	0.15	0.1	79.38706969	80.1992528	78.6287089	76.8179992
1	100	0.15	0.2	76.2987013	78.37139164	77.32893652	77.55186722
1	100	0.15	0.3	71.7959353	76.23931624	76.5372874	73.54497354
1	100	0.15	0.4	67.33176839	71.50515464	72.78884462	75.48387097
1	100	0.15	0.5	55.32897268	59.0086546	62.02830189	64.63654224
1	100	0.15	0.6	36.63366337	53.17035905	58.59554873	60.70734551
1	100	0.2	0.1	75.79038545	76.84563758	78.52604828	77.52273712
1	100	0.2	0.2	71.6194332	74.77253929	75.27629963	74.02327515
1	100	0.2	0.3	60.03913894	71.77225341	74.88789238	74.59114479
1	100	0.2	0.4	49.54163484	64.41476826	67.21115538	65.87620579
1	100	0.2	0.5	28.71287129	52.8055342	58.15686275	59.33384973
1	100	0.2	0.6	15.23229246	46.8344775	52.70164448	53.49016583
1	100	0.25	0.1	68.54552621	73.42304458	75.0111957	78.04557406
1	100	0.25	0.2	59.38215103	71.86507937	72.76765882	78.01742016
1	100	0.25	0.3	37.07093822	65.57441769	67.60676873	65.98905395
1	100	0.25	0.4	19.38309216	51.92012289	57.52895753	57.88655789
1	100	0.25	0.5	11.08149276	42.23153085	52.34587049	49.01960784
1	100	0.25	0.6	6.778370145	36.42257818	47.63899467	41.53318078
1	100	0.3	0.1	41.91570881	67.68316832	73.33629104	74.58912769
1	100	0.3	0.2	24.52399086	58.49203265	67.12275215	61.75282714
1	100	0.3	0.3	17.66945925	50.84162204	59.71165398	59.02211874
1	100	0.3	0.4	9.025133283	42.08317436	54.84375	51.1043412
1	100	0.3	0.5	8.035034273	32.0258949	46.1038961	42.65041889
1	100	0.3	0.6	7.692307692	18.88804265	27.76085301	28.67479056
1	100	0.35	0.1	18.73571973	53.6838066	68.29672607	62.70922538
1	100	0.35	0.2	19.1926885	41.88880427	57.00119	54.28681276
1	100	0.35	0.3	14.5468393	32.45614035	48.06290756	45.87332054
1	100	0.35	0.4	10.01523229	25.17136329	34.00609292	32.0258949
1	100	0.35	0.5	6.9687738	18.35491241	23.229246	24.52399086
1	100	0.35	0.6	8.568164509	11.76694593	18.16450876	17.82178218

Figure A.3: Motion detection data continued.

GSD [m]	SNR	PTT WFE [waves]	Flimsy WFE [waves]	% M.D. BGR	% M.D. BGRN	% M.D. GRN	% M.D. RN
1.5	25	0.1	0.1	41.81227143	33.83124748	33.58901897	32.4586193
1.5	25	0.1	0.2	33.23898099	21.19499394	23.85950747	18.20750908
1.5	25	0.1	0.3	20.22607994	11.86919661	12.83811062	9.285425918
1.5	25	0.1	0.4	8.679854663	7.953169156	8.679854663	7.186112233
1.5	25	0.15	0.1	38.29357056	27.33144933	24.02099314	23.2135648
1.5	25	0.15	0.2	29.18853452	17.52119499	18.57085184	11.86919661
1.5	25	0.15	0.3	12.99959629	9.12394025	8.397254744	9.890997174
1.5	25	0.15	0.4	4.76382721	6.055712556	6.661283811	5.571255551
1.5	25	0.2	0.1	26.32216391	17.56156641	18.65159467	17.03673799
1.5	25	0.2	0.2	15.90633831	11.30399677	9.850625757	10.45619701
1.5	25	0.2	0.3	6.055712556	7.307226484	7.549454986	6.661283811
1.5	25	0.2	0.4	3.027856278	5.651998385	6.096083973	6.176826807
1.5	25	0.25	0.1	13.44368187	8.800968914	9.043197416	7.509083569
1.5	25	0.25	0.2	6.822769479	6.984255147	7.428340735	6.661283811
1.5	25	0.25	0.3	3.714170367	5.732741219	6.297941058	6.620912394
1.5	25	0.25	0.4	2.947113444	5.167541381	5.490512717	5.530884134
1.5	50	0.1	0.1	65.19427403	62.04620462	70.71917808	68.4741488
1.5	50	0.1	0.2	60.34412126	52.05535206	58.39933306	64.07964242
1.5	50	0.1	0.3	53.18458418	39.92733145	44.04521599	43.96447315
1.5	50	0.1	0.4	40.16955995	23.4557933	29.35002019	26.80662091
1.5	50	0.1	0.5	19.45902301	14.85668147	14.61445297	13.60516754
1.5	50	0.1	0.6	13.0399677	10.01211143	11.50585386	9.366168753
1.5	50	0.15	0.1	59.61616987	55.4158215	60.43046358	62.33388704
1.5	50	0.15	0.2	52.8103518	45.37747275	52.00161747	53.0995106
1.5	50	0.15	0.3	39.44287444	27.81590634	35.28461849	33.79087606
1.5	50	0.15	0.4	23.41542188	18.89382317	18.85345176	16.22930965
1.5	50	0.15	0.5	13.76665321	11.74808236	11.54622527	10.73879693
1.5	50	0.15	0.6	8.235769075	7.832054905	9.608397255	9.366168753
1.5	50	0.2	0.1	48.5668147	43.6011304	52.37901586	52.88617886

Figure A.4: Motion detection data continued.

GSD [m]	SNR	PTT WFE [waves]	Flimsy WFE [waves]	% M.D. BGR	% M.D. BGRN	% M.D. GRN	% M.D. RN
1.5	50	0.2	0.2	38.01051355	28.46184901	35.93056116	40.37141704
1.5	50	0.2	0.3	27.2507065	24.54582156	25.23213565	19.82236577
1.5	50	0.2	0.4	11.1425111	16.47153815	15.13928139	15.54299556
1.5	50	0.2	0.5	8.397254744	8.72022608	10.29471134	9.729511506
1.5	50	0.2	0.6	5.490512717	6.822769479	7.22648365	6.620912394
1.5	50	0.25	0.1	35.72870408	32.82196205	33.91199031	37.46467501
1.5	50	0.25	0.2	25.87807832	22.52725071	25.71659265	22.56762212
1.5	50	0.25	0.3	14.65482438	16.55228099	14.81631005	13.28219621
1.5	50	0.25	0.4	6.984255147	11.34436819	11.02139685	11.3847396
1.5	50	0.25	0.5	4.36011304	7.105369398	7.832054905	6.217198224
1.5	50	0.25	0.6	3.875656036	6.015341138	6.419055309	6.297941058
1.5	50	0.3	0.1	19.86273718	20.75090836	22.0427937	22.72910779
1.5	50	0.3	0.2	8.800968914	12.27291078	12.91885345	11.66733952
1.5	50	0.3	0.3	3.67379895	9.325797335	10.13322568	10.01211143
1.5	50	0.3	0.4	3.471941865	6.701655228	6.822769479	5.651998385
1.5	50	0.3	0.5	3.67379895	6.096083973	6.499798143	5.85385547
1.5	50	0.3	0.6	2.503027856	5.329027049	5.530884134	5.490512717
1.5	50	0.35	0.1	4.723455793	10.9002826	11.02139685	10.33508276
1.5	50	0.35	0.2	3.835284618	9.446911587	8.962454582	8.03391199
1.5	50	0.35	0.3	3.148970529	6.782398062	6.015341138	6.459426726
1.5	50	0.35	0.4	2.785627776	5.934598304	6.176826807	6.055712556
1.5	50	0.35	0.5	2.543399273	5.651998385	5.692369802	5.611626968
1.5	50	0.35	0.6	2.341542188	6.015341138	5.611626968	5.611626968
1.5	100	0.1	0.1	69.93006993	74.54850903	79.06877403	80.11314186
1.5	100	0.1	0.2	65.51582409	68.13095731	80.23799405	74.46808511
1.5	100	0.1	0.3	59.63488844	58.61785274	70.21276596	72.65886288
1.5	100	0.1	0.4	48.04198627	50.78724263	61.61869003	61.73913043
1.5	100	0.1	0.5	28.30036334	37.86838918	47.42810855	55.14855515
1.5	100	0.1	0.6	21.35647961	32.41824788	35.93056116	36.53613242

Figure A.5: Motion detection data continued.

GSD [m]	SNR	PTT WFE [waves]	Flimsy WFE [waves]	% M.D. BGR	% M.D. BGRN	% M.D. GRN	% M.D. RN
1.5	100	0.15	0.1	63.02486751	68.59504132	72.5	74.48757087
1.5	100	0.15	0.2	59.02636917	60.56166056	74.04181185	75.01049979
1.5	100	0.15	0.3	44.52082491	53.90214315	64.30653894	65.72912159
1.5	100	0.15	0.4	31.0456197	44.85264433	54.54918033	57.02075702
1.5	100	0.15	0.5	19.74162293	33.34679047	42.99555914	43.23778765
1.5	100	0.15	0.6	16.02745256	28.78482035	31.20710537	29.67299152
1.5	100	0.2	0.1	53.21471896	60.6409203	69.58762887	70.90146751
1.5	100	0.2	0.2	43.88373032	55.87404118	64.5119863	66.92242114
1.5	100	0.2	0.3	29.87484861	47.19418652	59.08529048	58.9198036
1.5	100	0.2	0.4	18.005652	37.26281792	47.6382721	49.41461445
1.5	100	0.2	0.5	10.09285426	27.08922083	35.89018975	32.90270488
1.5	100	0.2	0.6	7.589826403	19.01493742	24.38433589	20.1453371
1.5	100	0.25	0.1	32.9430763	51.07157299	65.08001641	63.4462568
1.5	100	0.25	0.2	28.98667743	45.17561566	60.20449898	61.4968815
1.5	100	0.25	0.3	13.88776746	32.37787646	46.50787243	46.02272727
1.5	100	0.25	0.4	7.307226484	26.72587808	33.1853048	28.50222043
1.5	100	0.25	0.5	5.167541381	19.49939443	21.5583367	17.07710941
1.5	100	0.25	0.6	4.279370206	12.51513928	15.09890997	12.27291078
1.5	100	0.3	0.1	16.51190957	38.79693177	55.83468395	56.41960308
1.5	100	0.3	0.2	8.356883327	32.62010497	49.37323089	43.35494327
1.5	100	0.3	0.3	5.127169964	23.25393621	35.93056116	31.24747679
1.5	100	0.3	0.4	4.037141704	15.05853855	22.24465079	19.74162293
1.5	100	0.3	0.5	3.391199031	11.94993944	12.47476786	12.11142511
1.5	100	0.3	0.6	2.987484861	8.760597497	9.285425918	7.912797739
1.5	100	0.35	0.1	5.611626968	26.84699233	38.91804602	36.37464675
1.5	100	0.35	0.2	4.198627372	16.8348809	24.26322164	25.79733549
1.5	100	0.35	0.3	3.552684699	12.5555107	16.99636657	15.82559548
1.5	100	0.35	0.4	3.189341946	11.86919661	13.40331046	13.20145337
1.5	100	0.35	0.5	3.068227695	9.40654017	10.05248284	11.10213969
1.5	100	0.35	0.6	2.462656439	6.297941058	8.558740412	7.791683488

Figure A.6: Motion detection data continued.

Appendix B

Spatial Target Detection Data

N.B. Image restoration was not utilized in these experiments.

GSD	SNR	PTT WFE [waves]	Flimsy WFE [waves]	PSR Blue	PSR Green	PSR Red	PSR NIR
1	25	0.1	0.1	3.0997014	3.3994458	3.2218965	3.1712444
1	25	0.1	0.2	2.4880893	2.9313265	2.9886816	2.9365594
1	25	0.1	0.3	2.1977567	2.535204	2.6316324	2.6641919
1	25	0.1	0.4	1.9759067	2.3275752	2.3259527	2.4236992
1	25	0.15	0.1	2.3451181	2.786872	2.9733326	2.9507353
1	25	0.15	0.2	2.1438846	2.3264471	2.5838353	2.7152483
1	25	0.15	0.3	1.9848642	2.1213392	2.1253621	2.4208125
1	25	0.15	0.4	1.8218393	1.9794003	1.8679917	2.1575928
1	25	0.2	0.1	2.0680998	2.1372753	2.4242577	2.6474706
1	25	0.2	0.2	1.9555271	1.979927	1.9931744	2.3813695
1	25	0.2	0.3	1.8080855	1.8582525	1.6562444	2.0064425
1	25	0.2	0.4	1.8529335	1.799154	1.5678591	1.8647216
1	25	0.25	0.1	1.8785547	1.8236928	1.8962515	2.2562533
1	25	0.25	0.2	1.8330788	1.7022198	1.7481018	1.957065
1	25	0.25	0.3	1.8105225	1.6725573	1.5917701	1.7336818
1	25	0.25	0.4	1.8252352	1.6473054	1.5261913	1.6707827

Figure B.1: PSR data - SNR 25.

GSD	SNR	PTT WFE [waves]	Flimsy WFE [waves]	PSR Blue	PSR Green	PSR Red	PSR NIR
1	50	0.1	0.1	3.2030191	3.4302597	3.255917	3.3495121
1	50	0.1	0.2	2.5880085	2.9525151	3.0155856	3.1250058
1	50	0.1	0.3	2.3154385	2.550877	2.6757384	2.8559283
1	50	0.1	0.4	2.0172407	2.3489729	2.4017445	2.6218089
1	50	0.15	0.1	2.4590793	2.8011284	2.9924235	3.1409199
1	50	0.15	0.2	2.259724	2.3814382	2.6262553	2.9166162
1	50	0.15	0.3	2.1256159	2.1955849	2.226991	2.635054
1	50	0.15	0.4	1.8917905	2.0925239	2.0109521	2.3786068
1	50	0.2	0.1	2.1288906	2.1922049	2.4717653	2.8446162
1	50	0.2	0.2	2.0415007	2.0423306	2.0996442	2.6057391
1	50	0.2	0.3	1.9247556	1.9431285	1.782733	2.2478007
1	50	0.2	0.4	1.845666	1.9435507	1.733531	2.082506
1	50	0.25	0.1	1.922806	1.8933861	1.9764914	2.4664078
1	50	0.25	0.2	1.8995769	1.831228	1.8032321	2.1897614
1	50	0.25	0.3	1.8804044	1.8130617	1.6534002	1.9664757
1	50	0.25	0.4	1.8265882	1.7933914	1.6236405	1.8738556

Figure B.2: PSR data - SNR 50.

GSD	SNR	PTT WFE [waves]	Flimsy WFE [waves]	PSR Blue	PSR Green	PSR Red	PSR NIR
1	100	0.1	0.1	3.2334936	3.4281946	3.2509026	3.3955089
1	100	0.1	0.2	2.6371213	2.945153	3.0059992	3.1759394
1	100	0.1	0.3	2.3780509	2.5389191	2.6672805	2.9070847
1	100	0.1	0.4	2.1054565	2.33203	2.3965554	2.6716611
1	100	0.1	0.5	1.8503843	2.1479304	2.2450107	2.500311
1	100	0.1	0.6	1.7264061	2.0178931	2.1593373	2.3869365
1	100	0.15	0.1	2.5006723	2.7922674	2.9802068	3.1916937
1	100	0.15	0.2	2.3166777	2.3917971	2.6176642	2.9703805
1	100	0.15	0.3	2.2011683	2.2129662	2.2527714	2.6897247
1	100	0.15	0.4	1.9863409	2.1053002	2.0269724	2.4306721
1	100	0.15	0.5	1.7762608	1.9516015	1.9350611	2.2612925
1	100	0.15	0.6	1.6947182	1.8456564	1.9223488	2.1690977
1	100	0.2	0.1	2.1497511	2.1977965	2.4829121	2.8965108
1	100	0.2	0.2	2.0920929	2.0433253	2.1357033	2.6634225
1	100	0.2	0.3	1.9732056	1.9603059	1.8548343	2.3175984
1	100	0.2	0.4	1.8934321	1.9596337	1.8049588	2.1233308
1	100	0.2	0.5	1.7751629	1.8507684	1.7547598	2.001658
1	100	0.2	0.6	1.7795001	1.7450513	1.7735139	1.9382604
1	100	0.25	0.1	1.9363466	1.9026496	1.9983407	2.5198046
1	100	0.25	0.2	1.9058994	1.8543581	1.8309537	2.2522316
1	100	0.25	0.3	1.8851879	1.8408805	1.6975472	2.014383
1	100	0.25	0.4	1.8035788	1.8292463	1.6473007	1.8946391
1	100	0.25	0.5	1.8336605	1.7570565	1.6678542	1.8285387
1	100	0.25	0.6	1.8278338	1.6864554	1.7055095	1.7844209
1	100	0.3	0.1	1.8436534	1.7311284	1.7527709	2.0886669
1	100	0.3	0.2	1.8110324	1.6701592	1.6278668	1.8610022
1	100	0.3	0.3	1.8084619	1.6504759	1.5245132	1.751744
1	100	0.3	0.4	1.8473261	1.6473865	1.5370926	1.7041602
1	100	0.3	0.5	1.868747	1.6386901	1.5968393	1.6729483
1	100	0.3	0.6	1.8341396	1.6311158	1.6487321	1.6310176
1	100	0.35	0.1	1.8196285	1.6033389	1.636011	1.8139397
1	100	0.35	0.2	1.8612885	1.5738164	1.5254876	1.7053088
1	100	0.35	0.3	1.9265354	1.5635268	1.4340539	1.5671024
1	100	0.35	0.4	1.9328766	1.5896703	1.4604923	1.5226617
1	100	0.35	0.5	1.9148762	1.6173862	1.5285737	1.5082876
1	100	0.35	0.6	1.8544286	1.6343656	1.6338525	1.532436

Figure B.3: PSR data - SNR 100.

Appendix C

GIQE Data

N.B. In this effort noise was not an experimental variable for the GIQE. All experimental results reported in this document were carried out with a noise to signal power ratio of .3 (variable within Wiener-Helstrom Filter), PTT RMS WFE knowledge of .5 [waves], and flimsy RMS WFE knowledge of .5 [waves].

GSD [m]	PTT WFE [waves]	Flimsy WFE [waves]	GIQE Blue	GIQE Green	GIQE Red	GIQE NIR
1	0.1	0.1	2.8045055	2.7243301	2.662444	2.5564532
1	0.1	0.2	2.6288287	2.6643771	2.5876384	2.4638885
1	0.1	0.3	2.5783649	2.6060859	2.5694732	2.3988582
1	0.1	0.4	2.3983327	2.54938	2.5301008	2.3998514
1	0.1	0.5	2.5009236	2.6645157	2.6085966	2.4778722
1	0.1	0.6	2.2285183	2.4653119	2.5156106	2.3869322
1	0.15	0.1	2.114619	2.2970653	2.3949575	2.3446689
1	0.15	0.2	1.948022	2.2362106	2.3222392	2.3163617
1	0.15	0.3	1.866633	2.3808305	2.4746426	2.3942455
1	0.15	0.4	1.7279456	2.0163426	2.2838792	2.3175073
1	0.15	0.5	1.7080943	1.7708931	2.0387644	2.2284346
1	0.15	0.6	1.6354708	1.7177943	1.9895396	2.1291965
1	0.2	0.1	1.6259791	1.81165	2.1985397	2.3091991
1	0.2	0.2	1.6058025	1.5732775	1.8701125	2.1582566
1	0.2	0.3	1.599006	1.4745969	1.5985186	1.9794113
1	0.2	0.4	1.6181718	1.4768712	1.5445437	1.8442909
1	0.2	0.5	2.2310834	2.4251123	2.4821249	2.3976277
1	0.2	0.6	1.8062412	2.1151354	2.2690889	2.2822963
1	0.25	0.1	1.5881645	1.657545	1.9181073	2.0836024
1	0.25	0.2	1.5618694	1.5154099	1.5027702	1.78806
1	0.25	0.3	1.5755268	1.431478	1.6901463	2.0906604
1	0.25	0.4	1.5983917	1.4964034	1.4118768	1.8741892
1	0.25	0.5	1.5202598	1.4129592	1.3384898	1.6219551
1	0.25	0.6	1.3881005	1.4740292	1.3351066	1.4601014
1	0.3	0.1	1.3196172	1.4923791	1.3572376	1.3903181
1	0.3	0.2	1.599588	1.2713638	1.3211637	1.7595863
1	0.3	0.3	1.6417431	1.381568	1.3314144	1.4363401
1	0.3	0.4	1.6561559	1.2665587	1.2893223	1.2526525
1	0.3	0.5	1.4336138	1.3519041	1.3565298	1.2217365
1	0.3	0.6	1.2862537	1.375611	1.3939248	1.1850423
1	0.35	0.1	1.147587	1.300583	1.3929908	1.167836
1	0.35	0.2	2.1088214	2.2752602	2.3729653	2.3711335
1	0.35	0.3	1.7300751	1.9778156	2.1599092	2.2569183
1	0.35	0.4	1.4729906	1.624321	1.8188545	2.0488739
1	0.35	0.5	1.3822214	1.5021314	1.4915921	1.7447586
1	0.35	0.6	1.0964195	1.4422784	1.3646375	1.3410024

Figure C.1: GIQE data.

Bibliography

Kodak kaf-09000 image sensor, 2006. 4.4

Kodak kaf-10500 image sensor, July 2007a. 4.4

Kodak kaf-16803 image sensor, September 2007b. 4.4

Kodak kaf-39000 image sensor, March 2007c. 4.4

Kodak kaf-4320e performance specification, April 2005. 4.4

Kodak kaf-4320e device performance specification, April 2004. 4.4

A. Adams. *Multispectral Persistent Surveillance*. PhD thesis, Rochester Institute of Technology, 2008. (document), 2, 4.9.2, 4.9.2.1

M. F. Barnsley, R. L. Devaney, B. B. Mandelbrot, H.-O. Peitgen, D. Saupe, and R. F. Voss. *The Science of Fractal Images*. Springer-Verlag New York Inc., 1988. 3.9.3

N. Block. A sensitivity study of a polychromatic sparse-aperture system. Master's thesis, Rochester Institute of Technology, 2005. 3.11, 4

B. Daniel. *A System Study of Sparse Aperture Sensors in Remote Sensing Applications with Explicit Phase Retrieval*. PhD thesis, Rochester Institute of Technology, 2009. 3.7

R. Easton. *Linear Systems for Imaging Science*, volume 1. RIT, 2004. 3.1

R. Easton. *Linear Mathematics with Applications to Imaging*, volume 2. Rochester Institute of Technology, 2005. 3.2, 3.3, 3.7, 4.9.1, 4.9.1.1

J. Fienup. Phase retrival for undersampled broadband images. *Journal of the Optical Society of America*, 16(7):1831–1838, July 1999. 4.6.1

R. D. Fiete. Image quality and lambda fn/p for remote sensing. *Optical Engineering*, 38(7): 1229–1240, July 1999. 3.5

R. D. Fiete, T. A. Tantalo, J. R. Calus, and J. A. Mooney. Image quality of sparse-aperture designs for remote sensing. *Optical Engineering*, 41(8):1957–1969, August 2002. (document), 3.12.1, 3.12.2, 4.8.1, 4.9

J. P. Gardner and et. al. The james webb space telescope. *Space Science Reviews in Press*, May 2006. (document), 5.1

J. W. Goodman. *Introduction to Fourier Optics*. McGraw-Hill Companies, Inc., 3 edition, 1996. 3.9

R. E. Introne. *Enhanced Spectral Modeling of Sparse Aperture Imaging Systems*. PhD thesis, Rochester Institute of Technology, 2004. (document), 3.6.5, 3.6.6, 3.6.7, 3.3, 4

B. V. Kumar, A. Mahalanobis, and R. Juday. *Correlation Pattern Recognition*. Cambridge University Press, 1 edition, 2005. 4.9.1.1

J. C. Leachtenauer and R. G. Driggers. *Surveillance and Reconnaissance Imaging Systems*. Artech House, Inc., 2001. 4.8.2

J. C. Leachtenauer, W. Malila, J. Irvine, L. Colburn, and N. Salvaggio. General image quality equation: Giqe. *Applied Optics*, 36(32):8322–8328, November 1997. 3.6.7, 4.8.1, 4.8.1, 5.5

T. Lewis. Timothy lewis email. not published, September 2008. 3.9.2

J. C. Mather, editor. *Integrated modeling activities for the James Webb Space Telescope: optical jitter analysis*, volume 5487, Bellingham, WA, 2004. SPIE. 4.6.2

J. Schott. *Remote Sensing: The Image Chain Approach*. Oxford University Press, 2 edition, 2007. 3.2, 3.2, 4.2, 4.3, 4.8.1, 4.8.1

M. Strojnik and B. F. Anderson, editors. *Translation of spectral radiance levels, band choices, and signal-to-noise requirements of focal plane specifications and design constraints*, volume 4486, 2002. 3.6, 3.6.4, 3.6.5

J. C. Wyant and K. Creath. Basic wavefront aberration theory for optical metrology. *Applied Optics and Optical Engineering*, XI, 1992. 3.9.1

R. Zwiggelaar and C. R. Bull. On the use of local and scalable fourier transforms, fractal dimension information, and texture segmentation. In *Conference Publication No. 410*. Image Processing And Its Applications, 4-6 July 1995. 3.9.3